



DESIGN AND DEVELOPMENT OF A 3D-PRINTED VORTEX TUBE REACTOR
FOR INCREASING THE PRODUCTIVITY OF LIPID-BASED NANOPARTICLES
VIA FLOW CHEMISTRY

KITTIPAT SUWANPITAK

A THESIS SUBMITTED IN PARTIAL FULFILLMENT OF
THE REQUIREMENTS FOR MASTER DEGREE OF SCIENCE
IN PHARMACEUTICAL SCIENCES AND MANAGEMENT
FACULTY OF PHARMACEUTICAL SCIENCE
BURAPHA UNIVERSITY

2024

COPYRIGHT OF BURAPHA UNIVERSITY

การออกแบบและพัฒนาเครื่องปฏิริยาเคมีแบบท่อกระแสนที่เตรียมด้วยการพิมพ์สามมิติ เพื่อเพิ่ม
ผลิตภาพของอนุภาคไขมันนาโนด้วยเคมีกรไหล



วิทยานิพนธ์นี้เป็นส่วนหนึ่งของการศึกษาตามหลักสูตรวิทยาศาสตรมหาบัณฑิต
สาขาวิชาวิทยาการและการจัดการทางเภสัชศาสตร์
คณะเภสัชศาสตร์ มหาวิทยาลัยบูรพา
2567
ลิขสิทธิ์เป็นของมหาวิทยาลัยบูรพา

DESIGN AND DEVELOPMENT OF A 3D-PRINTED VORTEX TUBE REACTOR
FOR INCREASING THE PRODUCTIVITY OF LIPID-BASED NANOPARTICLES
VIA FLOW CHEMISTRY



KITTIPAT SUWANPITAK

A THESIS SUBMITTED IN PARTIAL FULFILLMENT OF
THE REQUIREMENTS FOR MASTER DEGREE OF SCIENCE
IN PHARMACEUTICAL SCIENCES AND MANAGEMENT
FACULTY OF PHARMACEUTICAL SCIENCE
BURAPHA UNIVERSITY

2024

COPYRIGHT OF BURAPHA UNIVERSITY

The Thesis of Kittipat Suwanpitak has been approved by the examining committee to be partial fulfillment of the requirements for the Master Degree of Science in Pharmaceutical Sciences and Management of Burapha University

Advisory Committee

Examining Committee

Principal advisor

.....

(Assistant Professor. Dr. Tanikan Sangnim)

..... Principal
examiner

(Professor Dr. Pornsak Sriamornsak)

Co-advisor

.....
(Associate Professor Dr. Kampanart
Huanbutta)

..... Member
(Assistant Professor Dr. Tanikan Sangnim)

..... Member
(Associate Professor Dr. Kampanart
Huanbutta)

.....
(Associate Professor Dr. Nopphon
Weeranoppanant)

..... Member
(Associate Professor Dr. Arpa
Petchsomrit)

..... Dean of the Faculty of Pharmaceutical
Science

(Dr. Nuttinee Teerakulkittipong)

This Thesis has been approved by Graduate School Burapha University to be partial fulfillment of the requirements for the Master Degree of Science in Pharmaceutical Sciences and Management of Burapha University

..... Dean of Graduate School
(Associate Professor Dr. Witawat Jangiam)

.....

64910154: MAJOR: PHARMACEUTICAL SCIENCES AND MANAGEMENT; M.Sc. (PHARMACEUTICAL SCIENCES AND MANAGEMENT)

KEYWORDS: Lipid-based nanoparticles, Computer-aided design, Computational fluid dynamics, Continuous flow chemistry, 3D-printing

KITTIPAT SUWANPITAK : DESIGN AND DEVELOPMENT OF A 3D-PRINTED VORTEX TUBE REACTOR FOR INCREASING THE PRODUCTIVITY OF LIPID-BASED NANOPARTICLES VIA FLOW CHEMISTRY. ADVISORY COMMITTEE: TANIKAN SANGNIM, Ph.D. KAMPANART HUANBUTTA, Ph.D. NOPPHON WEERANOPPANANT, Ph.D. 2024.

Lipid-based nanoparticles are versatile drug delivery systems, composed of lipids, phospholipids, cholesterol, and modified lipids. They efficiently encapsulate hydrophobic and hydrophilic drugs, enhance solubility and stability, and enable controlled drug release and targeted delivery while reducing toxicity due to their biocompatibility and low immunogenicity. However, conventional lipid-based nanoparticle preparation methods like batch synthesis has limitations in terms of nanoparticle properties, productivity, and scalability. To address these challenges, this study focuses on a new design vortex tube reactor fabricated by 3D printing techniques for continuous synthesis via flow chemistry. The optimized reactor, manufactured using polypropylene through fused deposition modeling, exhibits improved mixing and reduced variance compared to conventional approaches. Lipid-based nanoparticles produced in this 3D-printed vortex tube reactor were thoroughly characterized, demonstrating the feasibility of this innovative method. The experimental results showed a reduction in particle size from 192.67 ± 9.40 nm to 166.23 ± 0.98 nm, a decrease in PDI from 0.25 ± 0.01 to 0.17 ± 0.01 , an increase in percentage of entrapment efficiency from $49.09 \pm 0.65\%$ to $67.75 \pm 1.55\%$, an increase in percentage of loading capacity from $28.99 \pm 0.38\%$ to $36.39 \pm 0.83\%$, and a significant boost in productivity from 1.05 ± 0.13 mg/min to 313.4 ± 12.88 mg/min, compared to traditional batch techniques. These tangible improvements underscore the advantages of this novel approach. Paving the way, this study emphasizes the significance of reactor design and flow parameters in continuous flow chemistry for consistent, high-quality large-scale pharmaceutical manufacturing.



ACKNOWLEDGEMENTS

I would like to take this opportunity to express my deepest gratitude to the individuals and groups who have been instrumental in the completion of this thesis. First and foremost, I am immensely thankful to my thesis advisors: Asst. Prof. Dr. Tanikan Sangnim, Assoc. Prof. Dr. Kampanart Huanbutta, and Assoc. Prof. Dr. Nopphon Weeranoppanant. Their guidance, patience, and unwavering support have been pivotal throughout this research journey. Their invaluable insights and dedication to my academic growth have made this thesis possible. I would like to express my gratitude for their mentorship and collaboration, which enriched the scope and quality of this thesis. This research would not have been possible without the generous support of the Faculty of Pharmaceutical Sciences at Burapha University, which provided both laboratory equipment and financial support. These contributions have been indispensable in the successful execution of this project. I extend my heartfelt gratitude to Mr. Supree Vichyavichien and B and Brothers Co., Ltd. for their invaluable assistance with 3D printing work and material support. I am deeply appreciative of the opportunities and guidance they have provided throughout our collaboration, which has been pivotal to the project's success. I want to extend my appreciation to my friends and colleagues for their camaraderie, intellectual exchanges, and encouragement. Your companionship and the stimulating discussions we shared were a constant source of motivation. To my family, I owe a debt of gratitude that words cannot fully express. Their unwavering support, understanding, and sacrifices have sustained me throughout this academic journey. This thesis is as much their achievement as it is mine. Last but not least, I would like to extend my gratitude to all those whose names might not appear in this acknowledgment but have played a part, big or small, in my academic journey. Your support and encouragement have been a source of inspiration. This thesis is a testament to the collective effort and encouragement of this wonderful community. Thank you all for being a part of this journey.

Kittipat Suwanpitak

TABLE OF CONTENTS

	Page
ABSTRACT.....	D
ACKNOWLEDGEMENTS.....	F
TABLE OF CONTENTS.....	G
LIST OF TABLES.....	N
LIST OF FIGURES.....	P
CHAPTER 1.....	1
INTRODUCTION.....	1
Statements and significance of the problems.....	1
Research questions.....	3
Objectives.....	3
Research hypothesis.....	3
Conceptual framework.....	4
Significance of the research (Research advantages).....	5
Academic.....	5
Economic.....	5
Environmental.....	5
Social.....	5
Scope of study.....	5
CHAPER 2.....	7
RELATED LITERATURE.....	7
1. Formulating drugs into nanoparticles.....	7
1.1 Classification of nanoparticles in pharmaceutical.....	7
1.1.1 Polymeric nanoparticles.....	8
1.1.2 Inorganic nanoparticles.....	8
1.1.3 Lipid-based nanoparticles.....	8

1.2 Drug loading strategies.....	9
1.2.1 Post-loading.....	9
1.2.1.1 Porous materials.....	9
1.2.1.2 Non-porous materials.....	10
1.2.2 Co-loading.....	10
1.2.3 Pre-loading.....	10
2. Nanoparticle synthesis used in pharmaceutical application.....	11
2.1 Batch chemical synthesis.....	11
2.2 Flow chemistry.....	12
2.3 Comparison of a batch chemical synthesis vs. a flow chemistry.....	13
2.4 Advantages of flow chemistry.....	15
2.5 The components of flow chemistry.....	16
2.5.1 The pump.....	16
2.5.2 The mixer.....	20
2.5.3 The reactor.....	22
2.5.5 The back pressure regulator.....	27
2.5.6 The downstream unit.....	29
2.5.7 Additional components.....	29
2.5.7.1 Heat and Cooling Systems.....	29
2.5.7.2 Oscillators.....	29
2.5.7.3 Electrochemistry.....	30
2.5.7.5 Light Sources.....	30
2.5.7.6 Ultrasound Devices.....	30
2.6 Parameters of continuous flow chemistry.....	30
2.6.1 Stoichiometry.....	30
2.6.2 Residence time.....	31
2.6.3 Volume and space at steady state.....	33
2.6.4 Mixing.....	34
2.6.5 Mass transfer.....	36

2.6.6 Heat transfer	38
2.6.7 Pressure	40
2.7 Application of continuous flow chemistry in pharmaceutical formulation of nanoparticles.....	40
3. Computation fluid dynamic	43
3.1 Governing equation of fluid dynamic	44
Continuity Equation;	45
Momentum Equation;.....	45
3.2 Turbulence model	46
3.2.1 Turbulent kinetic energy (k)	47
3.2.2 Dissipation rate (ϵ)	49
3.3 Discretization method.....	52
3.2.1 Finite volume method.....	52
3.2.2 Finite element method	52
3.2.3 Finite difference method.....	53
3.4 Steps in flow simulation	53
3.4.1 Creating a 3D model.....	53
3.4.2 Mesh generation	53
3.4.3 Defining the fluid properties	54
3.4.4 Boundary conditions.....	54
3.4.4.1 Flow openings.....	55
3.4.4.2 Pressure openings	55
3.4.4.3 Wall characteristics	55
3.4.5 Defining the equations.....	55
3.4.5 Simulation run	55
4. 3D printing technology	55
4.1 VAT polymerization.....	56
4.1.1 Principle mechanism	56
4.1.2 Advantages	57

4.1.3 Limitations.....	57
4.2 Material extrusion.....	58
4.2.1 Principle mechanism	58
4.2.2 Advantages	59
4.2.3 Limitations.....	59
4.3 Material jetting	60
4.3.1 Principle mechanism	60
4.3.2 Advantages	61
4.3.3 Limitations.....	61
4.4 Binder jetting	62
4.4.1 Principle mechanism	62
4.4.2 Advantages	63
4.4.3 Limitations.....	63
4.5 Powder bed fusion	64
4.5.1 Principle mechanism	64
4.5.2 Advantages	65
4.5.3 Limitations.....	65
4.6 Direct energy deposition.....	66
4.6.1 Principle mechanism	66
4.6.2 Advantages	67
4.6.3 Limitations.....	67
4.7 Sheet lamination	68
4.7.1 Principle mechanism	69
4.7.2 Advantages	69
4.7.3 Limitations.....	70
CHAPTER 3	71
EXPERIMENTALS	71
1. Materials	71

2. The vortex tube reactor design and model development according to design of experiment	71
3. Numerical analysis.....	73
Continuity equation:	74
Momentum equation:	74
3.1 Mixing index evaluation.....	75
3.2 Reynolds number expression.....	76
4. Mesh independency test.....	77
5. Optimization of geometrical vortex tube reactor model design	79
6. Fabrication of 3D printed vortex tube reactor based FDM.....	79
7. Dispersion experiment	80
8. Synthesis and evaluation of PGA nanoparticles for investigation of flow chemistry parameters in a vortex tube reactor.....	82
9. Formulating lipid-based nanoparticles through a vortex tube reactor using the Block Behnken design	83
10. Lyophilization of lipid-based nanoparticles.....	84
11. The physical characteristics of lipid-based nanoparticles.....	84
12. Entrapment efficiency and loading capacity evaluation	85
13. Productivity evaluation	86
14. Morphology evaluation.....	86
15. Optimization condition for lipid-based nanoparticles formulation using a vortex tube reactor	87
16. Statistical analysis.....	88
CHAPTER 4	89
RESULTS.....	89
1. CFD mesh sensitivity.....	89
2. Experimental design of vortex tube reactor	90
2.1 Mixing performances of vortex tube reactor (Y_1).....	92
2.2 Flow structures of vortex tube reactor (Y_2).....	95
3. Optimized vortex tube reactor	97

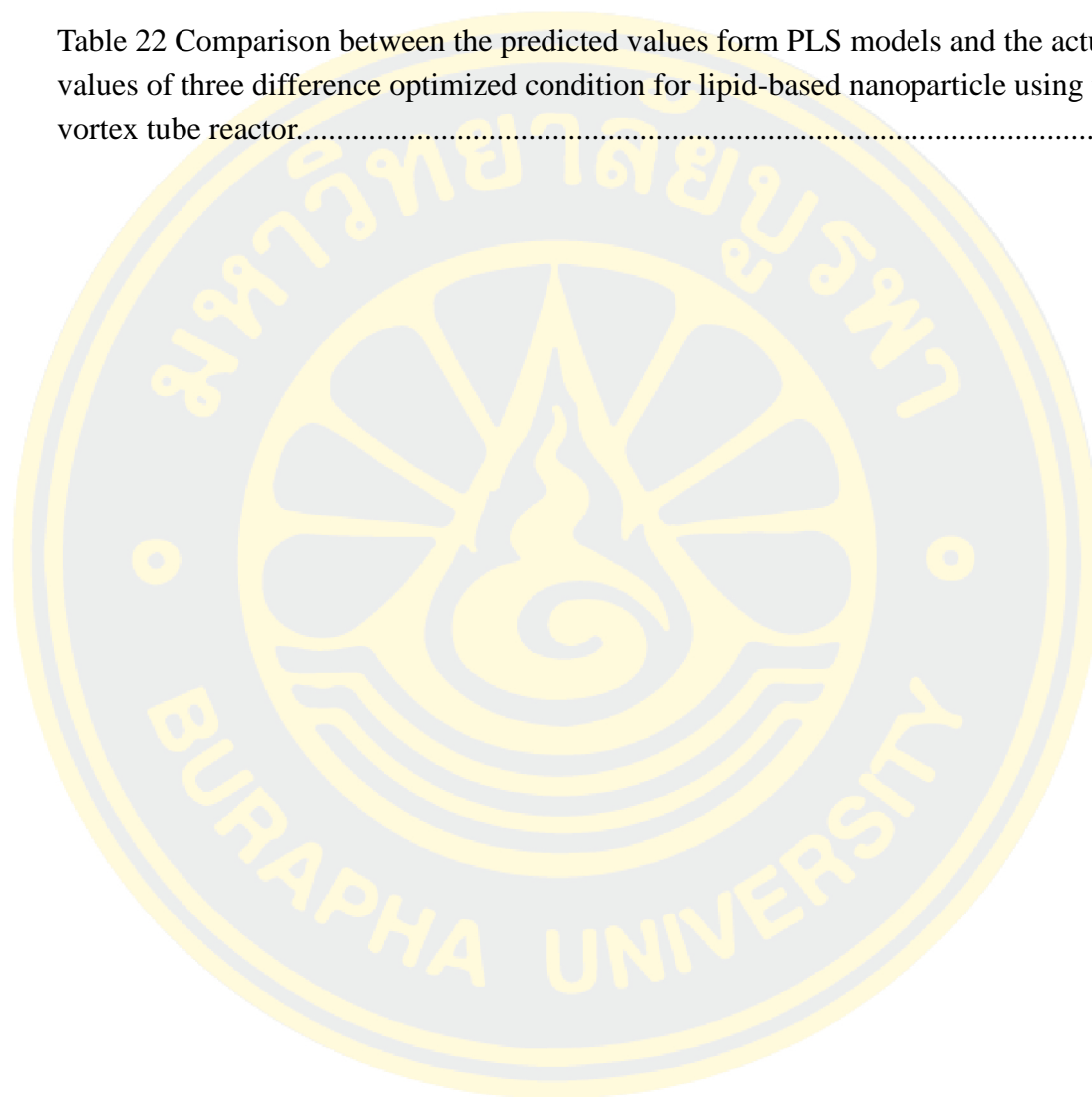
3.1	Mixing performance evaluation	98
3.2	Reynolds number evaluation	99
3.3	Relationship of mixing index in difference flow rate.....	100
4.	Fabrication of the vortex tube reactor based FDM.....	103
5.	Dispersion experiment	104
6.	Investigation of flow chemistry parameters in vortex tube reactor on formulated PGA nanoparticles	105
6.1	Effect of input flow rate on formulated PGA nanoparticles.....	106
6.2	Effect of aqueous-to-organic volumetric ratio on formulated PGA nanoparticles.....	108
6.3	Comparison of the formulated PGA nanoparticles using three different synthesis methods.....	109
7.	Experimental design of lipid-based nanoparticles formulation using a vortex tube reactor	111
7.1	Z-average (Y_1).....	114
7.2	Polydispersity index (Y_2)	117
7.3	Zeta-potential (Y_3).....	118
7.4	Entrapment efficiency percentage (Y_4)	120
7.5	Loading capacity percentage (Y_5)	121
7.6	Productivity (Y_6)	122
8.	Optimization condition for lipid-based nanoparticles formulation using a vortex tube reactor	123
9.	Prediction performance.....	127
10.	Formulation uniformity over formulated time.....	128
11.	Comparison of lipid-based nanoparticle formulation between vortex tube reactor and batch synthesis	130
CHAPTER 5	132
CONCLUSION	132
REFERENCES	135
APPENDIX	144
BIOGRAPHY	163



LIST OF TABLES

	Page
Table 1 Comparison of key parameters between batch chemical synthesis and flow chemistry.	14
Table 2 Types of pumps in flow chemistry.	17
Table 3 Types of mixers in flow chemistry.	20
Table 4 Types of reactors in flow chemistry.	23
Table 5 Back pressure regulator in flow chemistry.	28
Table 6 A comparison of surface area per reaction vessel volume. (Mallia, Carl J., and Ian R. Baxendale, Organic Process Research & Development, 2016, 20.2: 327-360.)	37
Table 7 The continuous flow chemistry setting-up in pharmaceutical formulation of nanoparticle.	41
Table 8 Summarized equation for CFD calculation.	51
Table 9 Factor levels based on central composite design.	73
Table 10 Properties of water and ethanol for CFD calculation from the engineering database (Solidworks).	75
Table 11 Constraint and criteria of the optimized vortex tube reactor model.	79
Table 12 The FDM 3D-printing condition.	80
Table 13 The interested factors on formulation of lipid-based nanoparticles using a vortex tube reactor.	84
Table 14 Constraint and criteria of the optimized condition of lipid-based nanoparticle synthesis.	87
Table 15 Relative error with the highest level automating generated grids (7 th level).	90
Table 16 Experimental runs and response results in the central-composite design.	91
Table 17 Partial Least Square Regression Model (PLS Model) in terms of coded factors of Y_1 and Y_2	92
Table 18 Comparison between the predicted values form PLS models and the actual values of optimized vortex tube reactor model.	97

Table 19 Mean residence times (t_m) and distribution variance (σ^2) of the 3D-printed optimized vortex tube reactor for the different flow rate.....	105
Table 20 Experimental runs and response results in the Block-Behnken design.	112
Table 21 Partial least square regression model in terms of coded factors.	113
Table 22 Comparison between the predicted values form PLS models and the actual values of three difference optimized condition for lipid-based nanoparticle using the vortex tube reactor.....	124



LIST OF FIGURES

	Page
Figure 1 Classification of nanoparticles in pharmaceutical. (Mitchell, Michael J., et al., 2021, p101-124).....	7
Figure 2 Principle of post-loading strategies. (Liu, Y., et al., 2022, p2143-2157).....	9
Figure 3 Principle of co-loading strategies. (Liu, Y., et al., 2022, p2143-2157).....	10
Figure 4 Principle of pre-loading strategies. (Liu, Y., et al., 2022, p2143-2157)	10
Figure 5 The installation of batch chemical synthesis. (The Essential Chemical Industry – online, 2013).....	12
Figure 6 The installation of continuous flow chemistry systems (a) T-shaped mixer, (b) Y-shaped mixer, (c) Quad-mixer, (d) syringe pump, (e) continuous-flow pump, (f) peristaltic pump, (g) tubular reaction vessel, (h) microfluidic chip, (i) column reaction vessel, and (j) back pressure regulator.	13
Figure 7 Mass transfer of internal phase and external phase in different the residence time. (Garcia-Ortega, Eduardo, et al., Chemical Engineering and Processing-Process Intensification, 2020, 153: 107921.).....	33
Figure 8 The flow characteristic of laminar flow(a) and turbulent flow(b) in tubular reactor. (Saliba, John, et al., Genes, 2018, 9.6: 285.).....	35
Figure 9 The position of the distance relative to the time of complete diffusion in the tubular reaction vessel.....	35
Figure 10 The temperature profile of (a) a batch synthesis and (b) a continuous flow chemistry. (Syrris-online, 2022)	38
Figure 11 Relation of a diameter of reaction vessel and heat diffusivity. (Noël T et.al., Organometallic Flow Chemistry, 2015, 1-41)	39
Figure 12 The fluctuation of the viscosity in turbulent flow. (Yucheng Liu et.al., 2011)	45
Figure 13 Type of CFD meshing of (a) tetrahedral grid and (b) hexahedral grid (Gullberg R. et.al., 2017)	54
Figure 14 VAT polymerization (Zhang J et al., Advanced Powder Technology, 2021, 32.9: 3324-3345.).....	56
Figure 15 Material extrusion (Zhang J et al., Advanced Powder Technology, 2021, 32.9: 3324-3345.).....	58

Figure 16 Material jetting (Zhang J et al., Advanced Powder Technology, 2021, 32.9: 3324-3345.).....	60
Figure 17 Binder jetting (Zhang J et al., Advanced Powder Technology, 2021, 32.9: 3324-3345.).....	62
Figure 18 Powder bed fusion (Zhang J et al., Advanced Powder Technology, 2021, 32.9: 3324-3345.).....	64
Figure 19 Direct energy deposition (Zhang J et al., Advanced Powder Technology, 2021, 32.9: 3324-3345.).....	66
Figure 20 Sheet lamination (Zhang J et al., Advanced Powder Technology, 2021, 32.9: 3324-3345.).....	68
Figure 21 The designed mixer model.	72
Figure 22 The designed vortex tube reactor model.....	72
Figure 23 Difference mesh refinement of the automating generated mesh in 7 levels.	78
Figure 24 Schematic representation of the experimental setting-up of the vortex tube reactor in synthesis of nanoparticles.	83
Figure 25 (a) Mesh independence test using the vortex tube reactor and (b) the automating generated mesh for all studied the vortex tube reactor model.	89
Figure 26 Response surface plot of the mixing index.....	94
Figure 27 Response surface plot of the Reynolds number.....	96
Figure 28 The mass fraction cut plot of (a) the vortex tube reactor and (b) the tubular reactor with a 4 mm diameter.....	98
Figure 29 Mass fraction evolutions along the midline at the exit of the optimized vortex tube reactor model and the tubular reactor with different flow rate.	99
Figure 30 The vorticity streamline cut plot of (a) the vortex tube reactor and (b) the tubular reactor with a 4 mm diameter.	100
Figure 31 The mixing index at different flow rates of the vortex tube reactor and the tubular reactor with 4 mm diameter.	101
Figure 32 Schematic representation of the 3D printed vortex tube reactor and assembly.....	103
Figure 33 Comparison of $E(\theta)$ curves in different flow rate of the printed vortex tube reactor.....	104

Figure 34 Z-average and PDI analysis of formulated PGA nanoparticles; (a) effect of input flow parameters, (b) effect of aqueous-to-organic volumetric ratio, and (c) comparison of formulated PGA nanoparticles using three different synthesis methods. Error bar represents 95% confidence interval. (n = 3, *p-value < 0.05, **p-value < 0.01, and ***p-value < 0.001 where a black star represents for significance of z-average and a red star represents for significance of PDI.)	107
Figure 35 SEM image of PGA nanoparticles prepared using (a) a 3D printed vortex tube reactor and (b) a tubular reactor.	111
Figure 36 Response surface plot for z-average: (a) X ₁ vs X ₂ , (b) X ₁ vs X ₃ , and (c) X ₂ vs X ₃	115
Figure 37 Response surface plot for PDI: (a) X ₁ vs X ₂ , (b) X ₁ vs X ₃ , and (c) X ₂ vs X ₃	117
Figure 38 Response surface plot for zeta-potential: (a) X ₁ vs X ₂ , (b) X ₁ vs X ₃ , and (c) X ₂ vs X ₃	119
Figure 39 Response surface plot for percentage entrapment efficiency: (a) X ₁ vs X ₂ , (b) X ₁ vs X ₃ , and (c) X ₂ vs X ₃	120
Figure 40 Response surface plot for productivity: (a) X ₁ vs X ₂ , (b) X ₁ vs X ₃ , and (c) X ₂ vs X ₃	122
Figure 41 TEM and SEM images of lipid-based nanoparticles using the vortex tube reactor: (a) TEM image at 44,000X, (b) TEM image at 89,000X, (c) SEM image at 15,000X, and (d) SEM image at 20,000X.	126
Figure 42 Comparison between the predicted values and the actual values of three difference optimized solutions for lipid-based nanoparticle using the vortex tube reactor based on (a) z-average, (b) PDI, (c) zeta-potential, (d) %EE, (e) %LC, and (f) productivity. Error bar represents 95% confidence interval.	128
Figure 43 X-chart and MR-chart of (a) z-average, (b) PDI, (c) zeta-potential, (d) %EE, (e) %LC, and (f) productivity across 6 lots of lipid-based nanoparticles formulation.	129
Figure 44 Comparison of lipid-based nanoparticle formulation: Vortex tube reactor vs. Batch synthesis; (a) z-average, (b) PDI, (c) zeta-potential, (d) %EE, (e) %LC, and (f) productivity. Error bar represents 95% confidence interval. (*p-value < 0.05, and **p-value < 0.01).	131

CHAPTER 1

INTRODUCTION

Statements and significance of the problems

Nanoparticles are currently under development as drug delivery systems for various drug substances and vaccines on the market, such as AmBisome, DepoCyt, Doxil, Inflexal, and Myocet (1). These nanoparticles are prepared using various materials designed for drug delivery purposes. For example, Pfizer-BioNTech and Moderna mRNA vaccines are formulated as lipid-based nanoparticles (2), while traditional formulations typically involve batch chemical synthesis. In this process, agitators are employed to mix reagents and facilitate chemical reactions within a mixing tank where the reaction time is determined by the mixing duration. However, this technique often encounters problems, such as a multi-modal distribution of nanoparticles, which can impact the quantity and efficacy of the drug substance. Additionally, the need to wait for synthesis completion before proceeding to the next step results in a non-continuous production process (3). To address this issue, production and synthesis techniques have been developed to enable continuous processes and ensure product consistency.

Flow chemistry represents a technique developed for the continuous synthesis of substances and the preparation of formulations, including polymeric nanoparticles, inorganic nanoparticles, and lipid-based nanoparticles. In this process, nanoparticles are continuously synthesized by regulating the flow of reactants into a coil or tube reactor for mixing and reaction, and subsequently directing them into a container. The flow chemistry reactor boasts a small diameter, enabling effective mixing and mass transfer with a high diffusion surface. Specific concentrations of reactants and products can be monitored at each region of the reactor, allowing for better control over reactions. The reaction time, or residence time, can be adjusted by regulating the flow rate and the volume of the reactor. Flow chemistry offers more stable heat transfer and pressure control compared to batch chemical synthesis, which relies on agitators to stir reagents in a tank, where the reaction depends on the reagents remaining in the tank or the exposure time of the reagents. In batch chemical

synthesis, heat transfer within the mixing tank is less stable due to limited heat transfer area. In certain reactions, inert gases are necessary to create pressure inside the mixing tank (4). In contrast, productivity with batch chemical synthesis is constrained by tank size and stirring time, whereas flow chemistry allows for continuous output through flow rate control. Nevertheless, the use of flow chemistry in industry remains limited due to the requirement for a significant amount of equipment to achieve sufficient productivity. Coil reactors or tube reactors used in flow chemistry are tubular in shape and possess a small diameter, resulting in flow characteristics that resemble laminar flow. The mixing mechanism is thus highly diffusion-based but low in convection. When the pipe diameter increases, the diffusion surface area decreases, and fluid velocity near the reactor wall is diminished due to friction, leading to a significant variation in fluid velocity around the reactor core or parabolic flows. This effect results in varying reaction times for each fluid stream at different radial distances from the axial center, potentially affecting product uniformity. Owing to the limitation of the chemical reactor's diameter, flow rate adjustment is restricted, culminating in inadequate productivity for industrial production (5).

To overcome these limitations in current reactor design and enhance productivity in flow chemistry systems, researchers have developed a new reactor design based on a larger volume and turbulent flow characteristics generated by vortex streamlines. This forward-thinking design is engineered to deliver a multifaceted enhancement in industrial processes. By integrating cutting-edge turbulence-inducing elements, it not only augments mass transfer but also revolutionizes mixing performance. The incorporation of these advanced elements optimizes the interaction and diffusion of substances, thereby accelerating chemical reactions and promoting uniform component distribution. As a result, the design facilitates not only faster adjustable flow rates but also a significant increase in overall productivity. This innovative configuration minimizes processing time, ensures consistent and high-quality outcomes, and has far-reaching implications in various sectors, spanning from pharmaceuticals to chemical processing and beyond (6-8).

Research questions

1 . Can the design of the vortex streamline flow direction inside the flow chemistry reactor increase mixing efficiency, and what are the associated flow characteristics?

2 . How do the manufacturing or design factors of reactor influence lipid-based nanoparticle product appearance, and how do they differ from conventional batch synthesis methods?

3 . Does the designed reactor demonstrate higher productivity of lipid-based nanoparticle formulation than the conventional batch synthesis method?

Objectives

1 . To examine the size and dimension parameters in each part of the reactor that influence flow and mixing characteristics for the optimized reactor design using computational fluid dynamics.

2 . To investigate the operation parameter relationship between optimized reactor model and lipid nanoparticle synthesis.

3 . Comparison between flow chemistry and batch synthesis for lipid-based nanoparticle fabrication.

Research hypothesis

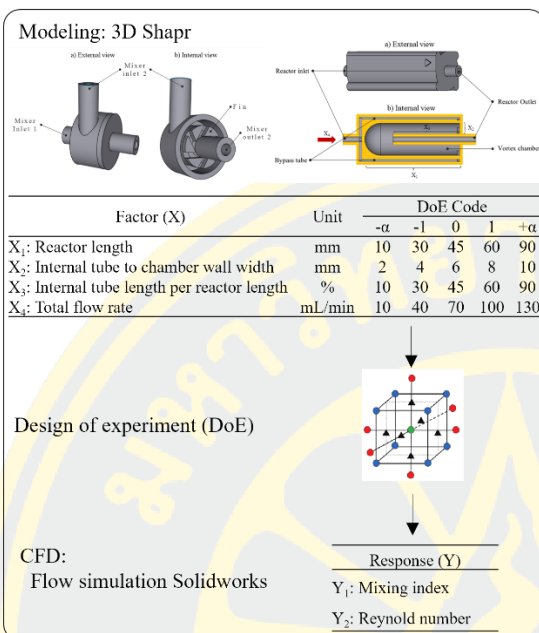
1 . Chaotic mixing in a vortex tube reactor enhances mixing efficiency and productivity.

2 . Increasing mixing efficiency accelerates mass transfer in reactions.

3 . The vortex tube reactor offers superior performance and enhances the properties of lipid-based nanoparticles compared to batch synthesis.

Conceptual framework

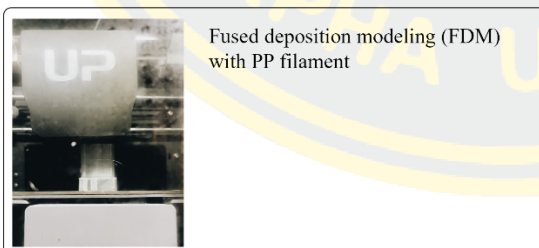
REACTOR DESIGN



OPTIMIZED VORTEX TUBE REACTOR MODEL

Factor (X) and Response (Y)	Criteria
X_1 Reactor length	in range
X_2 Internal tube to chamber wall width	in range
X_3 Percentage of Internal tube length/Reactor length	in range
X_4 Total flow rate	in range
Y_1 Mixing index	target = 1
Y_2 Reynolds number	maximize

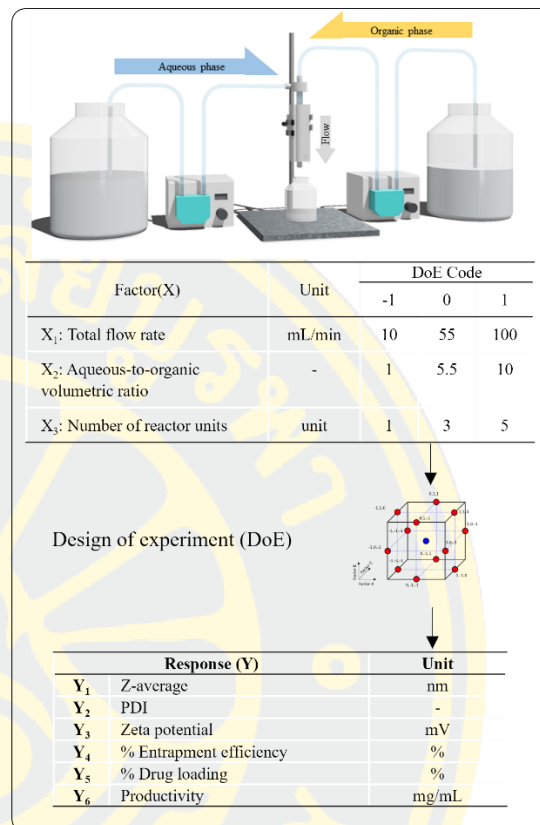
FABRICATION BASED FDM



DISPERSION EXPERIMENT

- Residence time distribution function (RTD)
- Mean residence times (t_m)
- Distribution variance (σ^2)

LIPID NANOPARTICLE SYNTHESIS



OPTIMIZED CONDITION FOR LNPs FORMULATION

Factor (X) and Response (Y)	Criteria
X_1 Total flow rate	in range
X_2 Aqueous-to-organic volumetric ratio	in range
X_3 Number of reactor units	in range
Y_1 Z-average	minimize
Y_2 PDI	minimize
Y_3 Zeta potential	minimize
Y_4 % Entrapment efficiency	maximize
Y_5 % Drug loading	maximize
Y_6 Productivity	maximize

- + TEM image
- + SEM image
- + Prediction performance
- + Formulation uniformity over batch
- + Comparison with batch synthesis

Significance of the research (Research advantages)

Academic

Understanding the design guidelines for flow chemistry reactors and the parameters influencing mixing efficiency is crucial for achieving high-quality synthesis at a larger scale. These guidelines can also be applied to other research studies, improving experimental results by increasing product yield, consistency, and stability through the advantages of flow chemistry. By following these guidelines, research sites can synthesize substances for their own use and reduce research costs.

Economic

Flow chemistry stands out as a valuable tool, allowing researchers to design reactors that enhance productivity and enable the domestic synthesis of substances or formulations, such as mRNA lipid nanoparticles. Notable examples of products benefiting from flow chemistry techniques include the Pfizer-BioNTech and Moderna vaccines. Producing these products domestically would reduce import costs and generate income within the country.

Environmental

Flow chemistry offers numerous environmental advantages compared to batch synthesis. In flow chemistry systems, the mixing process consumes less energy compared to mixing tanks with impellers. Additionally, flow chemistry enables faster heat transfer for temperature control, resulting in reduced energy usage. Furthermore, flow chemistry generates a larger product volume, reducing the need to remove unwanted substances and thereby minimizing environmental degradation.

Social

The use of a well-designed flow chemistry reactor can streamline domestic vaccine production, leading to faster and more efficient distribution. This increased accessibility to vaccines can significantly improve the overall quality of life for the population.

Scope of study

1. This research is computational fluid dynamic of a design of vortex tube reactor for flow chemistry instrument in a pilot scale production. The interest factors

in this study were include X_1 : reactor length (mm), X_2 : internal tube to chamber wall width (mm), X_3 : percentage of internal tube length per reactor length (%) and X_4 : total flow rate (ml/min) which is related to the response including Y_1 : mixing index and Y_2 : Reynolds number. The controllable factors were set by the boundary condition including temperature, pressure, type of liquid and non-slip velocity condition. The factors were varied by 4-factor, 5-level of Central Composite Design in Design expert11 software. The models from DoE were drawn with Shapr3D software. The fluid mechanism of the reactor models were studied by computation fluid dynamic (CFD) in flow simulation Solidworks2021 software. The optimized model was built by fused deposition modeling (FDM) 3D printing technique.

2 . The printed optimized reactor was tested in the mixing efficiency by residence time distribution (RTD) experiment to study the flow characteristics.

3 . The lipid-based nanoparticles synthesis was performed by 3-factor, 3-level Box-Behnken design in Design expert11 software. Bovine serum albumin (BSA) served as the biological model drug, while dipalmitoylphosphatidylcholine (DPPC) and cholesterol were employed as the lipid components. The interest factors in this study were include X_1 : total flow rate (mL/min), X_2 : aqueous-to-organic phase volumetric ratio and X_3 : number of reactor unit (unit) which is related to the response including Y_1 : Z-average (nm), Y_2 : polydispersity index (PDI), Y_3 : zeta-potential (mV), Y_4 : percentage entrapment efficiency (%), Y_5 : percentage of loading capacity (%), and Y_6 : productivity (mg/min). The optimized lipid-based nanoparticles synthesis condition was predicted and tested of synthesis uniformity then comparison of the performance with the batch synthesis.

CHAPTER 2

RELATED LITERATURE

1. Formulating drugs into nanoparticles

Nanoparticles are particles that range in size from 10 to 1000 nanometers. The development of nanoparticle delivery systems is an interdisciplinary science that has attracted the attention of researchers over the decade. With the aim of increasing the solubility of the active substance that is less soluble or less absorption, improved bioavailability, pharmacokinetics, able to control drug release at a specified rate and can be delivered to the target organ to reduce side effects and increase treatment efficacy of patients (9).

1.1 Classification of nanoparticles in pharmaceutical

This section explores the classification of nanoparticles in pharmaceuticals, including polymeric nanoparticles, inorganic nanoparticles, and lipid-based nanoparticles, each with distinct characteristics and applications, as illustrated in Figure 1.

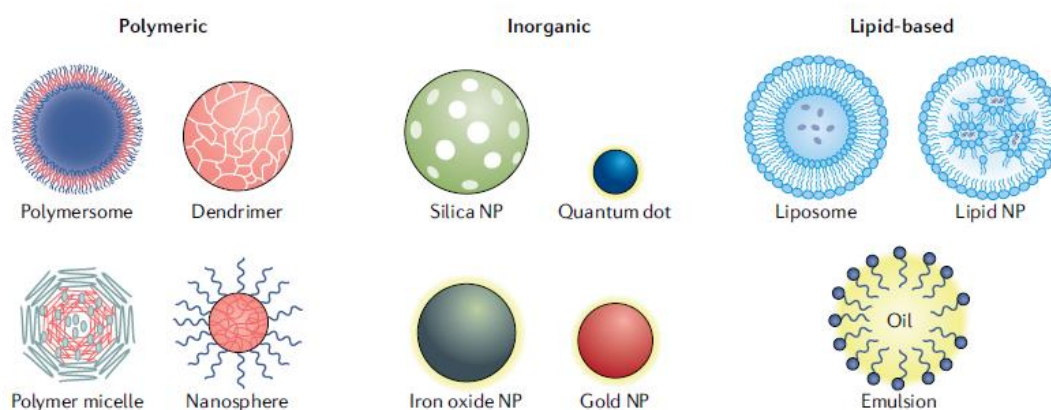


Figure 1 Classification of nanoparticles in pharmaceutical. (Mitchell, Michael J., et al., 2021, p101-124)

1.1.1 Polymeric nanoparticles are particles derived from natural or synthetic polymers, each possessing a variety of structures and properties. Types of polymeric nanoparticles include polymersomes, dendrimers, polymeric micelles, and nanospheres. Several techniques are employed for the synthesis of polymer nanoparticles, such as emulsification (solvent displacement or diffusion) (10), nanoprecipitation (11), ionic gelation (12), and microfluidics (13). The resulting product varies with each technique. Commonly used polymers include poly(lactide-co-glycolide) (PLGA) (14), poly(butyl cyanoacrylate) (15), polymethacrylate (16), chitosan (17), poly(ϵ -caprolactone) (PCL) (18), and poly(vinyl alcohol)-fatty acid copolymers (19). These polymers can undergo further synthesis to enhance the properties of the nanoparticles.

1.1.2 Inorganic nanoparticles are particles composed of inorganic materials, such as gold (20), iron (21), silica (22), and quantum dots (23), utilized for drug delivery and imaging applications. Inorganic nanoparticles exhibit specific physical, electromagnetic, and optical properties. The synthesis of nanoparticles from inorganic materials allows for control over size, structure, and shape, resulting in diverse properties of nanoparticles.

1.1.3 Lipid-based nanoparticles employ lipids as their primary components to create drug carriers with distinct advantages in drug delivery. Nanoparticles utilizing solid lipids as their primary component are referred to as Solid Lipid Nanoparticles (SLNs). In SLNs, drug substances are dispersed within reduced solid lipid particles in the nanoscale range, which reduces the risk of adverse reactions. They effectively encapsulate hydrophobic drugs, improving drug solubility and bioavailability. The nanoscale range of SLNs enhances drug penetration, and they remain stable at both room and body temperature, making them suitable for a wide range of drug delivery applications (24). On the other hand, Nanostructured Lipid Carriers (NLCs), represent another intriguing class of lipid-based nanoparticles. NLCs combine solid and liquid lipids, enhancing their drug loading capacity and structural stability, often prepared from phospholipids and cholesterol where the drug substance is entrapped in the carriers. This unique composition allows for controlled drug release, making them suitable for a variety of release mechanisms. NLCs can be functionalized for targeted drug delivery and are generally well-tolerated by the body,

with potential for reducing immunogenicity (25). Both SLNs and NLCs remain non-melting at room temperature or body temperature, giving them a flexible vesicular appearance. Examples include liposomes with lipid bilayers and nano-emulsions, which employ emulsifiers to encapsulate the drug in an organic phase that disperses in an aqueous phase.

1.2 Drug loading strategies

Drug loading within nanoparticles can be categorized in several ways, and in this context, the categorization is based on the sequence of adding drug substances (26).

1.2.1 *Post-loading* represents a technique involving the construction of nano-carriers before the introduction of drug substances into them, as illustrated in Figure 2. Characteristics of nano-carriers can be grouped into two material types which are porous materials and non-porous materials.



Figure 2 Principle of post-loading strategies. (Liu, Y., et al., 2022, p2143-2157)

1.2.1.1 Porous materials are designed to have a porous nanostructure. During the drug loading process, drug substances in solution are blended with the nano-carriers. Subsequently, the drug substances are retained within the porous nanostructures through various mechanisms such as adsorption, electrostatic interactions, entrapment, hydrophobic forces, and more. Porous materials encompass silica nanoparticles, carbon nanoparticles, metal-organic framework (MOF) nanoparticles (27), iron nanoparticles (21), hydrogel nanoparticles (28), calcium silicate hydrate nanoparticles (29), magnesium silicate nanoparticles (30), and hydroxyapatite nanoparticles (31).

1.2.1.2 Non-porous materials can function as nano-carriers for loading drug substances before the nano-carrier preparation, utilizing mechanisms like noncovalent hydrophobic interactions, electrostatic attraction, hydrogen bonding, and pi-pi stacking. Non-porous materials compass protein-based nanocarriers such as bovine serum albumin (BSA) nanoparticle (32).

1.2.2 *Co-loading* is a conjugation technique that involves drug-polymer conjugates (33), drug-macromolecule conjugates (34), or drug-drug conjugates (35), as illustrated in Figure 3. The compartment containing these conjugated molecules includes both hydrophilic and hydrophobic components, which can self-assemble when dispersed in the external phase.



Figure 3 Principle of co-loading strategies. (Liu, Y., et al., 2022, p2143-2157)

1.2.3 *Pre-loading* is a coating technique applied to a drug core, as illustrated in Figure 4. The drug core can be prepared through nanoprecipitation, followed by the deposition of the carrier to coat the nano-precipitated drug core. This process can be likened to the creation of a protective shell structure (36).

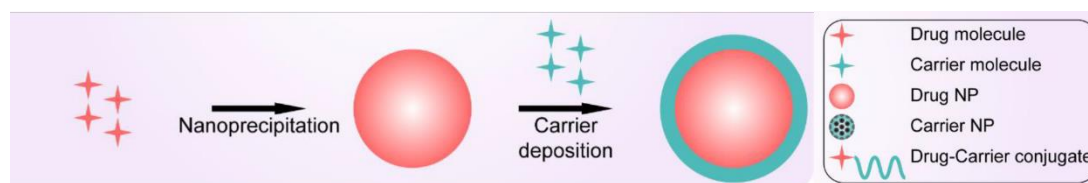


Figure 4 Principle of pre-loading strategies. (Liu, Y., et al., 2022, p2143-2157)

2. Nanoparticle synthesis used in pharmaceutical application

2.1 Batch chemical synthesis

Batch chemical synthesis is a widely used technique in the pharmaceutical, chemical, and materials industries for the production of a variety of chemicals and compounds, as shown in Figure 5. This method involves combining all the starting materials into the mixing tank in sequence, and then allowing the reaction to proceed under controlled conditions while the agitators rotate to mix the materials to facilitate chemical reactions until the desired product is obtained. The duration of the reaction depends on the mixing time. If the reaction occurs at high pressure, inert gases such as nitrogen may be added to the system to increase the pressure in the system. The temperature of the synthesis reaction in the mixing tank can be controlled by adding hot or cold water to the external shells of the tank. Once the starting materials have been added to the mixing tank, they cannot be removed or extracted until the reaction is complete. Therefore, batch chemical synthesis is not suitable for unsteady-state reactions or to produce intermediate substances, which can result in a lower yield of the desired product and make it difficult to correct errors in the synthesis process. Additionally, problems with the synthesis of nanoparticles often arise due to a wide range distribution and multi-modal distribution of nanoparticle synthesis, which can affect the quantity and efficiency of the particles. In addition, having to wait for the synthesis to be completed before using the product in the next process will result in a non-continuous production process that also a challenge in batch chemical synthesis (3). Due to this problem, a synthesis technique was developed to ensure that the synthesis process was continuous, and the product uniformity was discussed below.

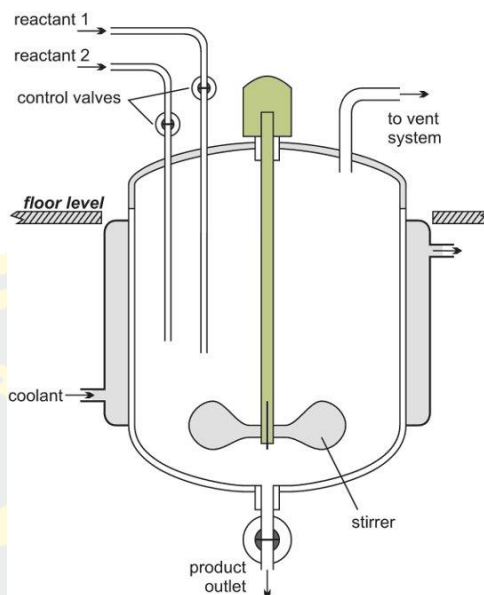


Figure 5 The installation of batch chemical synthesis. (The Essential Chemical Industry – online, 2013)

2.2 Flow chemistry

The technique of synthesizing using flow chemistry is a new method developed to address the limitations of traditional batch synthesis. This technique is also known as continuous flow chemistry, flow synthesis, or plug flow chemistry. It involves using pumps to introduce starting materials through small diameter tubes, typically 0.5-2 millimeters in diameter, which then mix at a connector. The mixture then flows into a coil reactor, column reactor, or microfluidic chip, where the reaction takes place until the product flows out of the system and is collected in a container, as shown in Figure 6. The reaction time depends on the volume of the tube or column and the total flow rate used in the system. If the reaction requires pressure, a back pressure regulator can be installed in the system without the need for gas. The temperature in the system can be controlled using a temperature control device, such as a water bath placed inside the reactor tube or column. In-line analysis can also be installed in the system to analyze the product continuously (37).

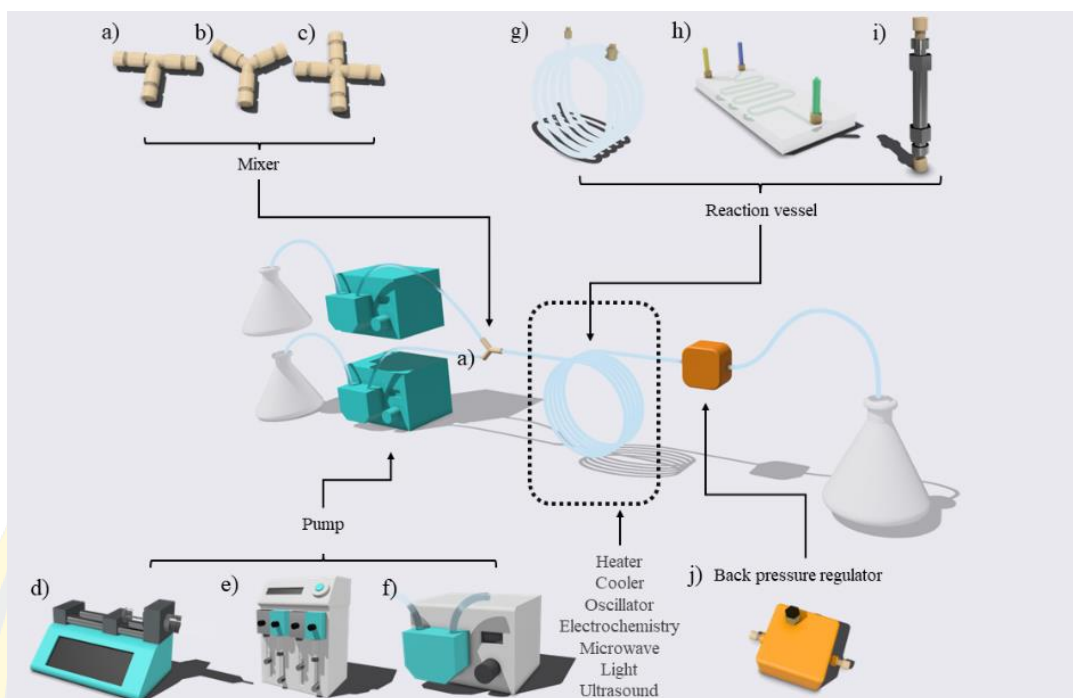


Figure 6 The installation of continuous flow chemistry systems (a) T-shaped mixer, (b) Y-shaped mixer, (c) Quad-mixer, (d) syringe pump, (e) continuous-flow pump, (f) peristaltic pump, (g) tubular reaction vessel, (h) microfluidic chip, (i) column reaction vessel, and (j) back pressure regulator.

2.3 Comparison of a batch chemical synthesis vs. a flow chemistry

Flow chemistry is a versatile and highly efficient approach to chemical synthesis that offers distinct advantages over traditional batch chemical synthesis methods. In this section, we present a comparative analysis of key parameters between batch chemical synthesis and flow chemistry, highlighting the superior control and efficiency that flow chemistry provides. Table 1 provides an overview of these parameters, illustrating how flow chemistry allows for precise control over various aspects of the synthesis process, resulting in improved productivity, product quality, and overall process optimization. By harnessing the advantages of flow chemistry, researchers and industries can achieve enhanced outcomes in the synthesis of important substances and high-value pharmaceutical products.

From Table 1, flow chemistry involves various parameters. These parameters can be precisely controlled and adjusted accordingly for each reaction. Furthermore, the progress of the reaction can be continuously monitored over time. In case of any errors during the synthesis process, the loss of product is much lower compared to synthesizing in a mixing tank. The remaining starting materials can still be used for other reactions since they are still stored in the container and have not undergone any reaction. Thus, flow chemistry provides significant benefits in pharmaceuticals, for synthesizing important substances, and producing high-value pharmaceutical products.

Table 1 Comparison of key parameters between batch chemical synthesis and flow chemistry.

Parameter	Batch chemical synthesis	Flow chemistry
Stoichiometry	The reactants are typically mixed together in a reactor vessel and left to react until completion. The stoichiometry of the reaction is determined by the initial amounts or molar ratio of reactants added to the vessel.	Flow chemistry allows for precise control over stoichiometry by introducing each reactant in a controlled manner and in precise ratios of flow rate and molarity.
Reaction time	Batch chemical synthesis usually involves longer reaction times, as the reactants are left to react until the reaction is complete by controlling stirring time.	Flow chemistry enables reactions to be completed more quickly, as the reactants are continuously fed into the reactor at a controlled rate that controlling the residence time, ensuring that the reaction progresses quickly and efficiently.

Reaction kinetics	The reaction kinetics in a batch synthesis is the reagent exposure time while often difficult to control, as the reaction may be subject to fluctuations in temperature, pressure, and other environmental factors.	Flow chemistry allows for precise control over reaction kinetics by the flow rate, as the reaction conditions can be carefully controlled and adjusted in real-time to optimize reaction conditions.
Productivity	The limitation on productivity in the batch synthesis is the size of the tank and waiting for the reaction to complete before the next step.	Flow chemistry often results in higher productivity compared to batch chemical synthesis, as the continuous nature of the process enables more efficient use of reactants and reduces the amount of time required for purification and separation.
Concentration profile	The concentration of reactants and products in the reactor vessel can vary over time, leading to fluctuations in reaction rate and yield.	Flow chemistry allows for precise control over the concentration profile of reactants and products, as the flow rate and reaction conditions can be carefully controlled and optimized to ensure maximum yield and purity.

2.4 Advantages of flow chemistry

Flow chemistry is a dynamic and efficient approach that provides meticulous control over synthesis parameters, ensuring the consistent production of chemical compounds with minimal variability. It sets itself apart by enabling the continuous synthesis of multi-step reactions, eliminating the need to wait for each individual reaction to finish before proceeding to the next step. This seamless progress not only saves valuable time but also enhances overall productivity (38, 39).

What makes flow chemistry particularly versatile is its adaptability; the devices employed in this method can be finely tuned and adjusted for each specific reaction, optimizing the reaction conditions and facilitating precise control over the chemical processes. Furthermore, safety is of paramount concern in the realm of flow chemistry in this aspect by reducing the risk of toxic exposure and safely managing potentially explosive reactions. This makes it a preferred choice for industries where safety is critical (40).

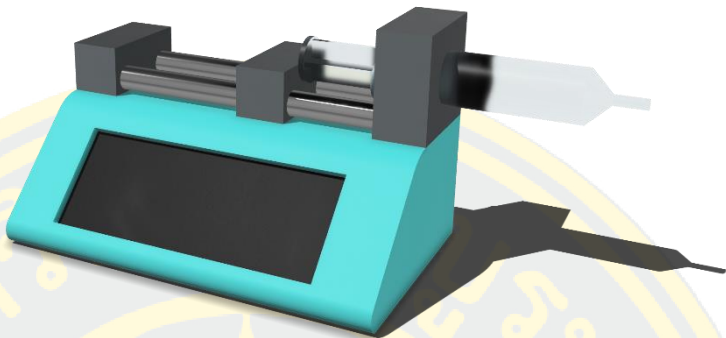
Incorporating in-line analysis further contributes to the appeal of flow chemistry. This feature allows real-time quality control, ensuring that the product's quality can be monitored and adjusted as needed throughout the synthesis process (41). Flow chemistry not only prioritizes safety and ensures product consistency, but it also boasts the potential for high production yields. The continuous nature of the process, combined with the controlled parameters and safety features, paves the way for efficient and prolific production of chemical compounds.

2.5 The components of flow chemistry

The flow chemistry components are essential for designing a process suitable for a particular reaction, as shown in Figure 6. The components of a flow chemistry system should be adjustable to meet the needs of the reaction. Therefore, the basic components of a flow chemistry system include a pump, mixer, reactor, column reactor, and back pressure regulator (39).

2.5.1 The pump is a crucial component used to draw reagent into the flow chemistry system and can be adjusted to match the required flow rate for the reaction. In context of continuous flow chemistry, different types of pumps are utilized, including syringe pumps, piston pumps, or peristaltic pumps. Each of these pumps has distinct advantages and is suitable for various applications, as shown in Table 2. The choice of pump in flow chemistry should be based on the specific requirements of the reaction, considering factors such as precision, reliability, flow rates, and the nature of the reagents being used. Each pump type has its advantages and limitations, and the selection should align with the needs of the application.

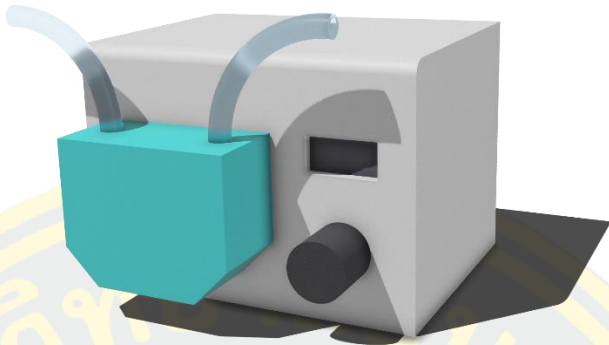
Table 2 Types of pumps in flow chemistry.

1. Syringe pump		
		
Mechanism	Advantages	Limitations
<p>Syringe pumps operate by using a motor to push a plunger within a syringe, thereby delivering a controlled and precise volume of reagent into the flow chemistry system. This mechanism allows for highly accurate flow rate control.</p>	<ul style="list-style-type: none"> • High Precision: Syringe pumps are renowned for their exceptional precision and accuracy in controlling flow rates. This makes them ideal for reactions where precise reagent delivery is critical. • Versatility: They can handle a wide range of flow rates and are well-suited for both small-scale and large-scale flow chemistry setups. • Low Dead Volume: Syringe pumps typically have minimal dead volume, ensuring that reagents are efficiently utilized and minimizing waste. 	<ul style="list-style-type: none"> • Limited Flow Rates: While versatile, syringe pumps may not be suitable for extremely high flow rates, as their design primarily targets precise control rather than rapid flow. • Complex Setup: Some syringe pump setups can be relatively complex, requiring careful calibration and maintenance. • Cost: High-precision syringe pumps can be costly, which may impact the overall cost of the flow chemistry system.

2. Piston pumps

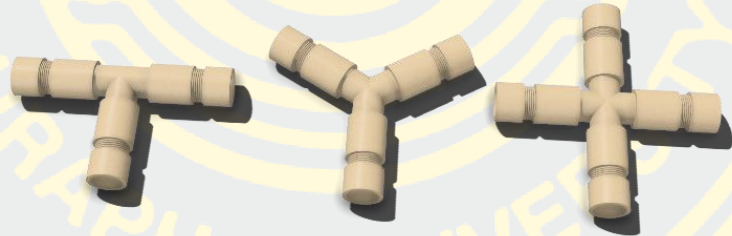


Mechanism	Advantages	Limitations
<p>Piston pumps use a reciprocating piston to generate fluid flow. They are known for their reliability and steady flow rates, which can be critical for certain reactions.</p>	<ul style="list-style-type: none"> • Reliability: Piston pumps are highly reliable and can operate continuously for extended periods. They are less prone to breakdowns and interruptions. • Variable Flow Rates: They offer a wide range of flow rates and are adaptable to various reaction requirements. • Resistance to Abrasive Reagents: Piston pumps can handle more viscous or abrasive reagents without significant wear and tear. 	<ul style="list-style-type: none"> • Complex Design: The internal design of piston pumps can be relatively complex, making them less straightforward to maintain and repair. • Higher Dead Volume: They may have a slightly higher dead volume compared to syringe pumps, potentially leading to some reagent waste. • Slower Response: Piston pumps may have slower response times compared to syringe pumps, which can affect certain reactions with rapid changes in flow rate.

3. Peristaltic Pumps		
		
Mechanism	Advantages	Limitations
<p>Peristaltic pumps use rollers to compress a flexible tube, propelling reagents through the system. The tube acts as a barrier between the pump and reagent, reducing contamination risk.</p>	<ul style="list-style-type: none"> • Contamination Control: The design minimizes contact between the reagent and the pump, making peristaltic pumps ideal for handling corrosive or sensitive materials. • Low Maintenance: They are generally low-maintenance devices, with easy tube replacement when needed. • Ease of Use: Peristaltic pumps are user-friendly and straightforward to set up. 	<ul style="list-style-type: none"> • Limited Precision: Peristaltic pumps may not provide the same level of precision and accuracy as syringe pumps, which can be a limitation in some applications. • Flow Rate Variability: They may have some variability in flow rates due to the tube compression mechanism, which can affect the consistency of reactions. • Lower Flow Rates: Peristaltic pumps may not be suitable for very high flow rates.

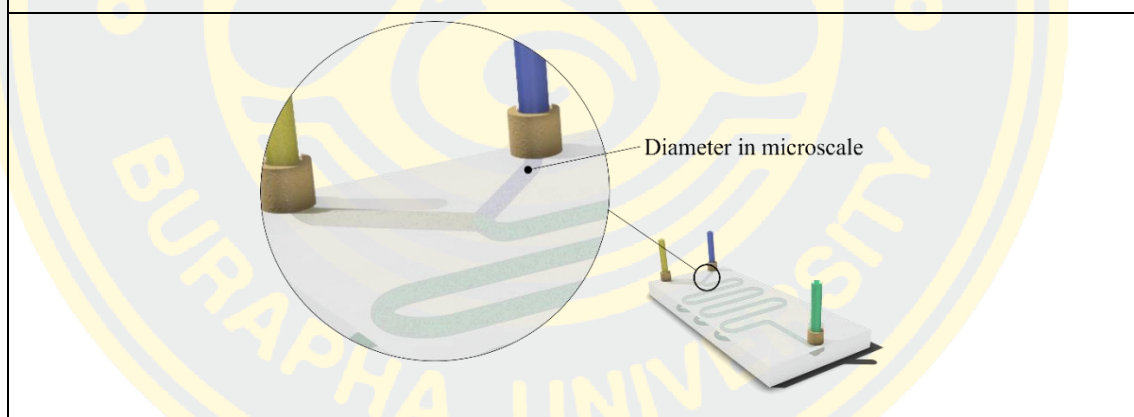
2.5.2 *The mixer* is an integral component of the flow chemistry system, responsible for facilitating the blending of reagents as they progress through the reaction pathway. The effectiveness of mixing plays a pivotal role in the success of the reaction, as it directly influences reaction kinetics and product yields. Mixers are designed in various configurations, shapes, and sizes, allowing them to be tailored to the specific requirements of different reactions. In flow chemistry, the choice of mixers depends on several factors, including the nature of the reaction, the reaction kinetics, and the physical properties of the reagents. Mixers can range from simple T-shaped mixer, Y-shaped mixers, and quad-shaped mixer for rapid blending to more complex designs like micromixers, helical mixers, or static mixers, as shown in Table 3, for precise control over residence time and mixing efficiency.

Table 3 Types of mixers in flow chemistry

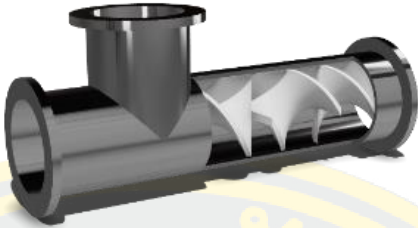
1. T-shaped mixer, Y-shaped mixer, and quad-mixer		
		
Mechanism	Advantages	Limitations
<p>The T-shaped mixer, Y-shaped mixer, and quad-mixer are fundamental components in flow chemistry used to facilitate the mixing of reagents. It operates based on the principle of confluence, where two or more reagent streams converge at a</p>	<ul style="list-style-type: none"> • Efficient mixing in rapidly blending reagents. The simple design of the junction encourages fast and thorough mixing, making it suitable for reactions where reagent homogeneity is crucial. • Low dead volume, which means minimal amounts of 	<ul style="list-style-type: none"> • May not be as effective in situations where precise control over mixing or longer residence times are required. • For some highly complex reactions, especially those with stringent mixing requirements, These mixers simplicity may not

<p>junction. This design promotes rapid and efficient mixing as the reagents collide and combine, leading to homogenization.</p>	<p>reagents are left behind in the mixer, reducing waste and ensuring that the majority of the reagents are utilized in the reaction.</p> <ul style="list-style-type: none"> • These mixers are relatively easy to integrate into flow chemistry systems. They are widely available and can be customized to suit different flow rates and reaction. 	<p>be sufficient. In such cases, more sophisticated mixer designs might be necessary.</p> <ul style="list-style-type: none"> • Depending on the flow rates and reagent properties, These mixers can sometimes lead to pressure drops in the system, which may need to be addressed in certain setups.
--	---	--

2. Micromixer



Mechanism	Advantages	Limitations
<p>Micromixers operate at a microscale, using various techniques such as chaotic advection and diffusion to achieve efficient mixing in confined spaces. They rely on intricate channel designs to promote rapid and thorough reagent blending.</p>	<ul style="list-style-type: none"> • High precision and control over mixing, especially in confined spaces. • Suitable for reactions with high reagent selectivity and fine-tuned residence time requirements. • Ideal for microreactors and lab-on-a-chip applications. 	<ul style="list-style-type: none"> • Complex design and fabrication, which may require specialized expertise. • Limited to applications where mixing at a microscale is necessary. • Potential for clogging in narrow channels, requiring vigilant maintenance.

3. Static mixer		
		
Mechanism	Advantages	Limitations
<p>Static mixers consist of stationary elements within the flow path, which induce mixing by disrupting the flow through their fixed geometry. They rely on the deformation and folding of reagent streams to achieve blending.</p>	<ul style="list-style-type: none"> • Low maintenance and reliability due to their lack of moving parts. • Suitable for continuous flow processes and can be customized for specific mixing requirements. • Ideal for applications involving viscous or shear-sensitive materials. 	<ul style="list-style-type: none"> • May be less efficient than more dynamic mixers for achieving thorough reagent homogeneity. • Limited precision in controlling mixing compared to micromixers. • Potential for increased pressure drop, particularly in configurations with numerous static mixings.

2.5.3 *The reactor*, which is connected to the mixer, typically operates by facilitating controlled reagent mixing within its channels, maintaining precise temperature control, and sometimes employing catalysts to enhance reactions. The continuous flow of reactants through the reactor enables efficient, scalable, and tightly regulated chemical processes, rendering flow chemistry an appealing choice across a broad spectrum of applications. Within the realm of chemical processes, various types of reaction vessels or reactors, as outlined in Table 4, assume a critical role, significantly shaping the efficiency and effectiveness of chemical reactions through their design and operational characteristics. In the end, the selection of the most suitable reactor depends on the specific demands of the reaction, including the desired reaction kinetics, reactant blending, and product purity.

Table 4 Types of reactors in flow chemistry

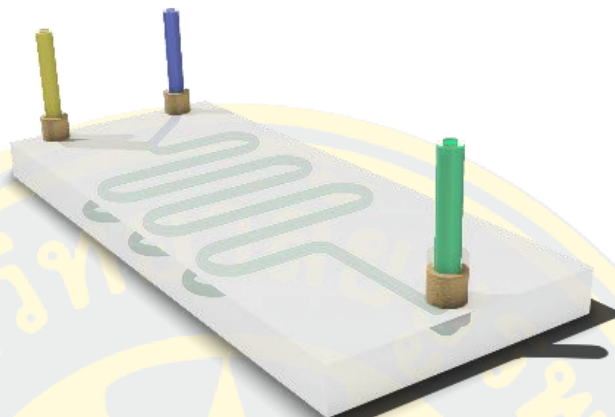
1. Plug Flow Reactors (PFRs)		
		
Mechanism	Advantages	Limitations
<p>Reactants flow through a long cylindrical vessel in a single direction, with no back mixing</p>	<ul style="list-style-type: none"> • Ideal for reactions with large temperature differences between reactants and products, as it minimizes heat transfer. • Provides a high degree of conversion of reactants to products. • Easy to model and optimize reaction kinetics. 	<ul style="list-style-type: none"> • May require larger reactor volumes compared to other reactor types for equivalent reaction conversion. • Difficult to control reaction conditions for highly exothermic reactions. • May require longer residence times to achieve complete reaction, increasing production costs.

2. Continuous Stirred Tank Reactors (CSTRs)



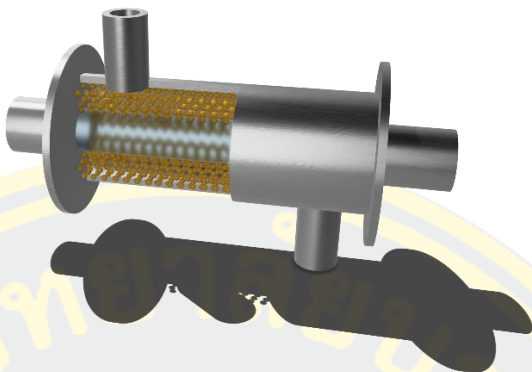
Mechanism	Advantages	Limitations
<p>Reactants are continuously mixed and reacted in a continuously stirred vessel.</p>	<ul style="list-style-type: none"> • Easy to control reaction conditions, including temperature and pressure. • Suitable for highly exothermic or endothermic reactions. • Can handle a wide range of reaction kinetics. 	<ul style="list-style-type: none"> • May have lower conversion rates compared to other reactor types, especially for fast reactions. • May require larger reactor volumes compared to other reactor types for equivalent reaction conversion. • May have higher production costs due to the requirement for continuous stirring.

3. Microfluidic Reactors



Mechanism	Advantages	Limitations
<p>Reactions occur in miniaturized channels or flow paths, with precise control over fluid flow and reaction conditions.</p>	<ul style="list-style-type: none"> • High surface area to volume ratio, leading to increased reaction efficiency and faster reaction kinetics. • Easy to control reaction conditions, including temperature, pressure, and reactant mixing. • Suitable for small-scale or high-throughput reaction processing. 	<ul style="list-style-type: none"> • Difficult to scale up to larger production volumes. • Limited by the size of the reaction channels and the volume of reactants that can be processed. • May require specialized equipment and fabrication processes for reactor design and construction.

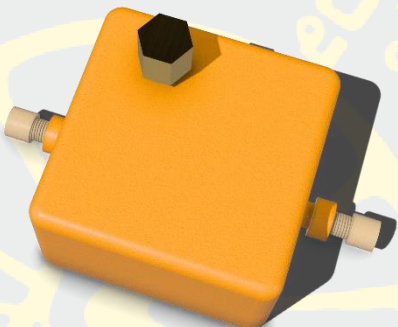
4. Specialized Reactors		
4.1 Catalytic Flow Reactor		
<p>Packed-bed reactor</p>  <p>Monolithic reactor</p>  <p>Inner-wall functionalized reactor</p> 		
Mechanism	Advantages	Limitations
<p>Reactants are continuously fed into the reactor and pass through the catalyst bed, where the reaction takes place.</p>	<ul style="list-style-type: none"> • Increased reaction efficiency due to the presence of a catalyst. • Suitable for reactions that require high temperatures and/or pressures. • Can handle a wide range of reaction kinetics. 	<ul style="list-style-type: none"> • May require specialized equipment and processes for reactor design and catalyst preparation. • The catalyst bed may need to be periodically replaced, increasing production costs. • May require careful monitoring and control of reaction conditions to prevent catalyst poisoning or deactivation.

4.2 Membrane Reactor		
		
Mechanism	Advantages	Limitations
<p>Reactants flow through the membrane and the reaction takes place on the membrane surface or within the membrane pores.</p>	<ul style="list-style-type: none"> • Increased reaction selectivity and product purity due to the separation of reactants and products by the membrane. • Easy to control reaction conditions, including temperature, pressure, and reactant mixing. • Suitable for reactions that generate harmful by-products or require highly controlled reaction conditions. 	<ul style="list-style-type: none"> • May require specialized equipment and fabrication processes for membrane design and preparation. • May be limited by the permeability of the membrane and the size of the reaction channels. • May require careful monitoring and control of reaction conditions to prevent membrane fouling or degradation.

2.5.5 The back pressure regulator is a vital element responsible for meticulously controlling pressure, ensuring the integrity and efficiency of chemical processes, as outlined in Table 5. It serves as a safeguard against runaway reactions resulting from pressure spikes, particularly in exothermic reactions. By diligently maintaining pressure at predetermined setpoints, the regulator prevents uncontrolled temperature increases and potentially catastrophic failures. Moreover, it is instrumental in maintaining product quality and consistency, a crucial factor in

industries where even minor pressure fluctuations can lead to variations in final product composition and properties, such as in the production of fine chemicals and pharmaceuticals.

Table 5 Back pressure regulator in flow chemistry

Black pressure regulator		
		
Mechanism	Advantages	Limitations
<p>A back pressure regulator is a device that controls the pressure at the outlet of a flow chemistry system. It operates by maintaining constant back pressure, which helps control the flow rate and improve the performance of the system. This is typically achieved by adjusting a spring-loaded piston or diaphragm to counteract the pressure in the system.</p>	<ul style="list-style-type: none"> • Precise Control: BPRs provide precise control over the pressure, ensuring stable and consistent flow rates in flow chemistry systems. • Prevention of Gas Bubbles: They prevent the formation of gas bubbles in the system, which can lead to irregular flow and unwanted reactions. • Improved Reaction Yield: Maintaining a constant pressure can enhance the reproducibility of chemical reactions and lead to higher yields. 	<ul style="list-style-type: none"> • Complexity: Some BPR systems can be complex to set up and maintain, requiring regular calibration and adjustment. • Cost: High-quality BPRs can be relatively expensive, which may be a significant cost factor in setting up a flow chemistry system. • Pressure Drop: BPRs can introduce a pressure drop in the system, which can impact the overall system efficiency and may require compensatory adjustments. • Compatibility: BPRs must be selected and installed

	<ul style="list-style-type: none"> • Safety: BPRs help in maintaining safe operating pressures, which is crucial for avoiding accidents and ensuring the integrity of the system. 	<p>carefully to ensure compatibility with the specific flow chemistry system and chemicals being used.</p>
--	--	--

2.5.6 *The downstream unit* of the flow chemistry holds a pivotal position, offering a range of flexible and strategic options for enhancing the overall efficiency and control of synthesis processes. One such option is the seamless connection to an in-line analytical tool, allowing for real-time monitoring and analysis of reaction parameters, product quality, and process kinetics. This real-time data acquisition enables operators to make on-the-fly adjustments and maintain precise control over the reaction, ensuring optimal yields and purity. Furthermore, the downstream unit can also be effectively integrated into the subsequent work-up operation, eliminating the need for intermediate transfer, and reducing the overall process footprint. This integration streamlines the workflow, saving time and resources, and can lead to more sustainable and cost-effective synthesis processes. The versatility in connecting the downstream unit to either in-line analytics or the next work-up operation underscores the adaptability and advantages of flow chemistry in modern chemical research and manufacturing.

2.5.7 *Additional components* are integral for precise control over synthesis conditions in various chemical processes. These components encompass a spectrum of technologies and techniques, including:

2.5.7.1 *Heat and Cooling Systems*: Temperature regulation is fundamental in chemical synthesis. Heat sources, such as heating mantles or ovens, and cooling systems like water baths or chillers, are employed to control and adjust reaction temperatures.

2.5.7.2 *Oscillators*: Oscillatory flow reactors are designed to introduce periodic variations in reaction conditions, promoting better mixing and enhancing selectivity in certain chemical reactions.

2.5.7.3 Electrochemistry: Electrochemical cells enable controlled redox reactions and are valuable in various applications, from organic synthesis to corrosion protection.

2.5.7.4 Microwave Irradiation: Microwave reactors provide rapid and uniform heating, accelerating reactions and reducing reaction times in many chemical processes.

2.5.7.5 Light Sources: Photoreactors utilize UV or visible light to initiate photochemical reactions, which can be highly selective and efficient.

2.5.7.6 Ultrasound Devices: Ultrasonication is employed to enhance mass transfer, increase reaction rates, and improve yields through cavitation-induced localized high temperatures and pressures.

Integrating these additional components into a flow chemistry setup offers operators a diverse toolbox for fine-tuning reaction conditions, optimizing reaction kinetics, and achieving desired product outcomes. These technologies contribute to the versatility and efficiency of flow chemistry, making it a powerful methodology for diverse chemical synthesis.

2.6 Parameters of continuous flow chemistry

In a continuous flow chemistry system, various parameters are controlled by the installed equipment to optimize the reaction. The important factors that need to be considered include stoichiometry, residence time, volume and space at steady state, mixing, mass transfer, temperature, and pressure. These parameters have a direct impact on the quantity and quality of the final product. It is important to adjust each parameter appropriately to achieve the desired outcome.

2.6.1 Stoichiometry

Stoichiometry is the relationship between the quantitative amounts of reactants and products in a chemical reaction. In continuous flow chemistry, the ratio of parameters such as reagent molarity and pump flow rate can be adjusted to set the specific stoichiometry for the reaction. Reaction kinetics are controlled by the reagent concentration and the flow rates of the reagent streams. The flow rates of the reagents

provide the residence time for the reaction, which can affect the outcome of the reaction. The flow rate (Q) is defined as the rate of volume change divided by time. Mathematically, it can be represented as:

$$Q = \frac{dV}{dt} \quad (1)$$

where; Q = Flow rate,
 dV = Volume of fluid,
 dt = Time.

By adjusting the flow rate, it is possible to control the residence time of the reaction and optimize the reaction conditions for the desired outcome.

The flow rate is related to the molarity of the reagent, which is defined as the molar flow rate. The molar flow rate can be calculated by multiplying the molarity of the reagent with the flow rate. Mathematically, it can be represented as:

$$n = cQ \quad (2)$$

where; n = Molar flow rate,
 c = Molarity,
 Q = Flow rate.

Molar flow rate is useful when it comes to determining the stoichiometry of the reaction and how much of each reactant is present in the reaction mixture. It allows the user to control the ratio of reactants to products, which is essential to the success of the reaction.

2.6.2 Residence time

The concept of reaction time in continuous flow chemistry refers to the amount of time that the reagents spend in the reaction vessel, also known as the

residence time. The residence time is determined by the ratio of the reaction vessel volume and the overall flow rate. It can be mathematically represented as:

$$\tau = \frac{V}{Q} \quad (3)$$

where; τ = Residence time,
 V = Volume of the system,
 Q = Flow rate of the system.

The residence time can be controlled by varying the volume of the reaction vessel or the flow rate of the reagents. For example, to achieve a longer residence time, it is possible to either pump more slowly or use a reaction vessel with a larger volume. It is important to control the duration of the reagents remaining in the reaction vessel, as it can affect the outcome of the reaction. A longer residence time can allow more time for the reactants to react, while a shorter residence time can lead to incomplete reactions. By controlling the residence time, it is possible to optimize the reaction conditions and achieve the desired outcome. In some reactions, where an intermediate is unstable, a continuous flow chemistry with a short residence time can be used. This can be beneficial for intermediate-sensitive reactions, as it allows for the immediate progression of the reaction to the next stage before the intermediate has a chance to degrade. This can result in a more productive synthesis than batch processing. In batch synthesis, the reactants are added and mixed sequentially in a reactor for a fixed time. This means that the reaction must wait for the mixing to complete before proceeding with the next reaction. And there is no addition or withdrawal of reactants until the end of the reaction, which can cause some of the intermediate to degrade while mixing. On the other hand, continuous flow chemistry allows for a constant flow of reactants through the reaction vessel, which eliminates the need to wait for mixing to complete before proceeding with the next reaction. This can result in a more efficient and productive synthesis, as well as reducing the risk of intermediate degradation (42).

2.6.3 Volume and space at steady state

Under flow conditions, each portion of the reaction vessel volume and space at steady state are defined by specific concentrations of the reactants and products. At a steady state, all the parameters are defined and remain constant at a particular point in time. As a result, the reaction profile within the reaction vessel can be defined in terms of space rather than reaction time. This is a key advantage of continuous flow chemistry as it allows for more precise and consistent control of the reaction conditions. By maintaining a steady state, it is possible to achieve a high degree of reproducibility and predictability in the reaction outcomes. Additionally, the ability to define the reaction profile in terms of space allows for more flexibility in the design of the reaction vessel and the manipulation of the reaction conditions.

Garciadiego-Ortega, Eduardo and colleagues have performed a computational fluid dynamics study of the heterogeneous phase extraction of uranium using continuous flow chemistry. Figure 7 shows that there is a mass transfer from the internal phase to the external phase when the position of the internal phase droplet is changed at each residence time. This phenomenon repeats as a pattern along the length of the reactor. As a result, the concentration at each point in the reaction vessel is approximately the same, which is a characteristic of specific concentrations in continuous flow chemistry when the flow system is in a steady state (43).

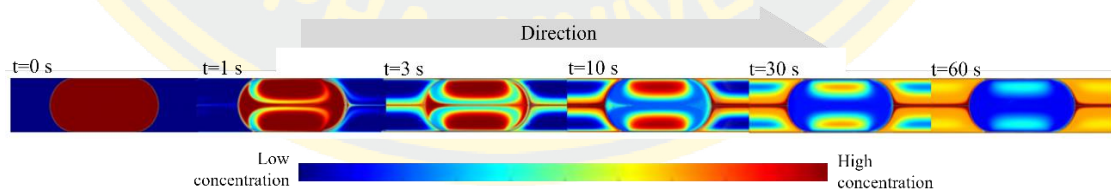


Figure 7 Mass transfer of internal phase and external phase in different the residence time. (Garciadiego-Ortega, Eduardo, et al., *Chemical Engineering and Processing-Process Intensification*, 2020, 153: 107921.)

2.6.4 Mixing

For efficient reactions, homogeneity mixing, and fast mass transfer are important. Mixing in continuous flow chemistry is highly advantageous compared to batch synthesis, as it leads to a better reaction profile due to high diffusion within small volumes of reagents in the reaction vessel. The flow characteristics of the system are one of the variables that indicate mixing and consist of two types: laminar flow and turbulent flow. Laminar flow occurs when the direction of fluid flow is parallel without layers disturbance, eddies or swirls of fluids. Therefore, diffusion term is the dominant in a mixing mechanism. On the other hand, turbulent flow is dominant of convection in a mixing mechanism by a chaotic property change that includes a rapid variation of pressure and flow velocity in space and time. The direction of fluid flow is no longer travels in layers and mixing across the reaction vessel. A dimensionless number that describes the flow characteristic can be calculated by the Reynolds number equation which is:

$$Re = \frac{\rho V D}{\mu} \quad (4)$$

where; Re = Reynolds number,
 ρ = Fluid density,
 V = Fluid velocity,
 D = Reactor diameter,
 μ = Fluid viscosity.

According to Figure 8, flows at Reynolds numbers larger than 4000 are typically turbulent, while those at low Reynolds numbers below 2300 usually remain laminar. Flows in the range of Reynolds numbers 2300 to 4000 are known as transition. It is important to select the appropriate flow characteristics to optimize the mixing and mass transfer in the continuous flow chemistry system (44, 45).

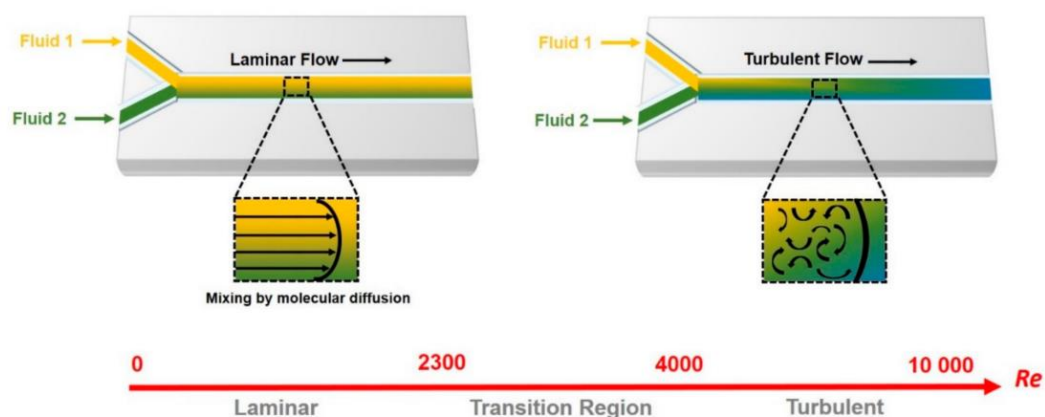


Figure 8 The flow characteristic of laminar flow(a) and turbulent flow(b) in tubular reactor. (Saliba, John, et al., Genes, 2018, 9.6: 285.)

In the context of tubular reactors with diameters ranging from 0.5 to 2 millimeters, the flow dynamics exhibit distinctive characteristics. Continuous flow chemistry in such systems is primarily characterized by laminar flow, a fascinating phenomenon where fluids move in parallel and smooth layers, as illustrated in Figure 9. This laminar flow behavior is especially noteworthy due to its role in shaping the reaction environment within the reactor.

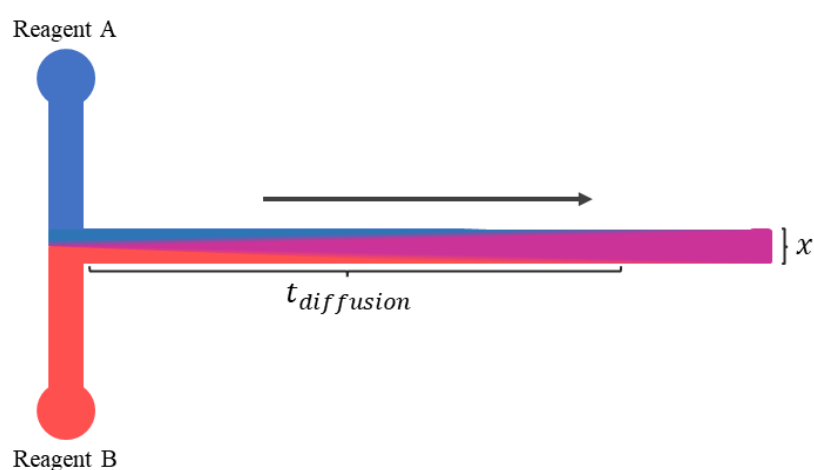


Figure 9 The position of the distance relative to the time of complete diffusion in the tubular reaction vessel.

According to the diffusion theory, the diffusion time is proportional to the square of the complete diffusion distance by diffusion coefficient. This can be represented by the equation:

$$t_{diffusion} = \frac{x^2}{D_{AB}} \quad (5)$$

where; $t_{diffusion}$ = Diffusion time,
 x = Complete diffusion distance,
 D_{AB} = Diffusion coefficient.

Therefore, shorter diffusion distances in a continuous flow chemistry will result in faster diffusion, which means faster mixing of the reagents. In order to ensure a uniform concentration across the reaction vessel, the time it takes for a molecule to flow from the entrance to the exit must be greater than the diffusion time (46).

2.6.5 Mass transfer

The high surface area per volume in a continuous flow chemistry is one of the key principles that lead to better mass transfer compared to batch synthesis (Table 6). A greater surface area per volume in continuous flow chemistry leads to more surface area contact between the reactants and results in a higher term of mass transfer coefficient. This is represented by the equation:

$$\text{Mass transfer coefficient} = k_L a \quad (6)$$

where; k_L = Mass transfer coefficient between the reactants,
 a = Surface area contact between the reactants.

Table 6 A comparison of surface area per reaction vessel volume. (Mallia, Carl J., and Ian R. Baxendale, *Organic Process Research & Development*, 2016, 20.2: 327-360.)

Reaction vessel type	Specific surface area per volume [m ² /m ³]
Microreactor ^[a]	104
Microreactor (gas-liquid) ^[b]	5,000
Tubular reactor	50-2,000
Packed column reactor	10-1,700
Static mixer	100-1,000
Stirred tank	100-2,000
5 mL-Round bottom flask	141
50 mL-Round bottom flask	66
250 mL-Round bottom flask	38

[a] For a volume of 140 μL of reaction vessel and 400x400 μm channel.

[b] Assume equivalent volume of gas and liquid with an average gas plug length of 2x the channel width.

Expanding the interfacial contact area to a considerable extent can create the opportunity for facilitating reactions that would typically be challenging to carry out within the confines of traditional batch synthesis procedures when transitioned to a continuous flow system (46, 47).

Microreactors typically have mass transfer coefficient values of 0.15-15 s⁻¹, while basic reactors used in laboratories, such as round bottom flasks, have mass transfer coefficient values of 0.001-0.02 s⁻¹. The equilibrium time of the reactants in the reaction is inversely proportional to the mass transfer coefficient, which can be represented by the equation:

$$t_{equilibrium} = \frac{1}{k_L a} \quad (7)$$

where; $t_{equilibrium}$ = Equilibrium time,

$k_L a$ = Mass transfer coefficient.

It was found that microreactors take less time to reach equilibrium of reactants, due to their greater mixing efficiency and high surface area to volume ratio.

This highlights the potential of microreactors in continuous flow chemistry to achieve faster and more efficient reactions (46).

2.6.6 Heat transfer

The large surface area-to-volume ratio of continuous flow chemistry allows for instantaneous and rapid heat transfer, which provides precise temperature control. This can lead to increased temperatures through the application of pressure, resulting in superheated reactions. For example, the normal boiling point of water is 100°C. In a continuous flow system, the temperature can be raised to 150°C at atmospheric pressure. Additionally, Figure 10 shows the temperature profiles of a batch synthesis and a continuous flow chemistry. Under flow conditions, the temperature can reach equilibrium quickly and remain constant over time. In contrast, batch synthesis typically has less thermal stability, with temperature gradually increasing until equilibrium is reached. This results in greater temperature variability and inconsistent temperature decreases.

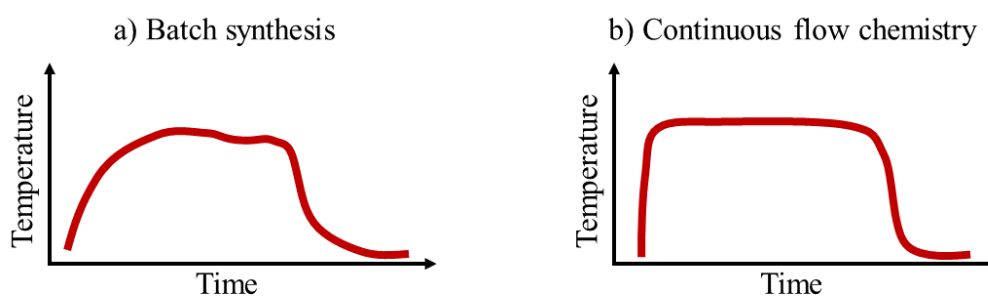


Figure 10 The temperature profile of (a) a batch synthesis and (b) a continuous flow chemistry. (Syrris-online, 2022)

Heat transfer efficiency in continuous flow chemistry plays a crucial role in determining the outcome of a reaction. One way to measure this efficiency is by using the ratio of heat exchange equation, which compares the heat generated during the reaction to the heat removed. The equation for this ratio is:

$$\beta = \frac{\text{Heat generation rate}}{\text{Heat remove rate}} = \frac{-r\Delta H_{rxn}d_F^2}{4\Delta T_{ad}\kappa} \quad (8)$$

where; β = Ratio of heat exchange,

r = Reaction rate,

ΔH_{rxn} = Reaction enthalpy,

d_F = Diameter of reaction vessel,

ΔT_{ad} = Adiabatic temperature,

κ = Heat diffusivity.

When the heat generation rate is equal to the heat removal rate, the β value is equal to 1, indicating a uniform heat exchange. However, if the heat generation rate is greater than the heat removal rate, the β value will be greater than 1, indicating poor heat exchange and a potential for temperature excursions.

The relationship between the diameter of a reaction vessel (d_F) and the heat transfer coefficient (κ) is illustrated in Figure 11. A microreactor with a smaller diameter (d_F) can enhance the heat transfer coefficient (κ) and result in a high rate of heat removal, resulting in a β value close to 1, indicating efficient heat exchange in continuous flow chemistry (42).

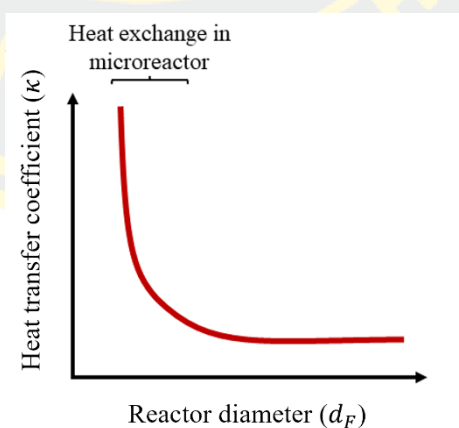


Figure 11 Relation of a diameter of reaction vessel and heat diffusivity. (Noël T et.al., Organometallic Flow Chemistry, 2015, 1-41)

2.6.7 Pressure

Controlling pressure in a continuous flow chemistry is a critical aspect of the process and is determined by two factors: back pressure due to flow, which increases with higher flow rates, narrow reaction vessels, or high viscosity liquids, and back pressure intentionally applied, typically through the use of a pressure regulator at the exit of the reaction vessel. The pressure inside the reaction vessel can be calculated using the Hagen-Poiseux equation:

$$\Delta P = \frac{8\mu LQ}{\pi R^4} \quad (9)$$

where; ΔP = Pressure,
 μ = Fluid viscosity,
 L = Length of the reaction vessel,
 Q = Flow rate,
 R = Radius of the reaction vessel.

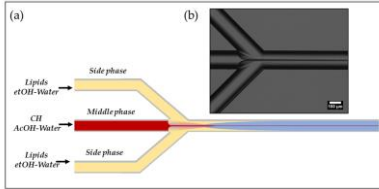
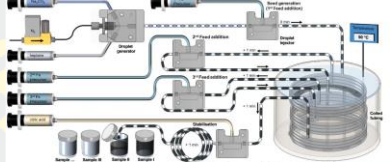
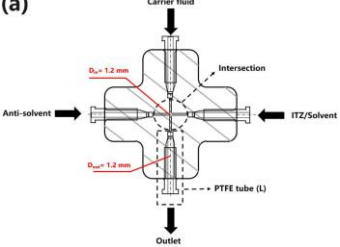
As per the Haagen-Poiseux equation, it is found that the pressure inside the reaction vessel increases with the higher viscosity of the fluid, longer length of the reaction vessel, higher flow rate and a smaller radius of the reaction vessel. When the reaction requires a higher pressure and the flow of the system does not produce enough pressure, a device called a pressure regulator can be used to increase the pressure in the system. There are various mechanisms for the pressure regulator, which can be checked in the manual (48).

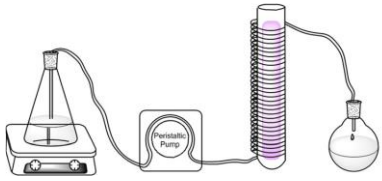
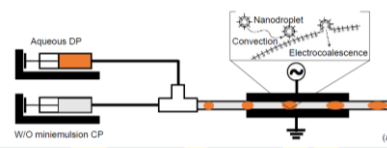
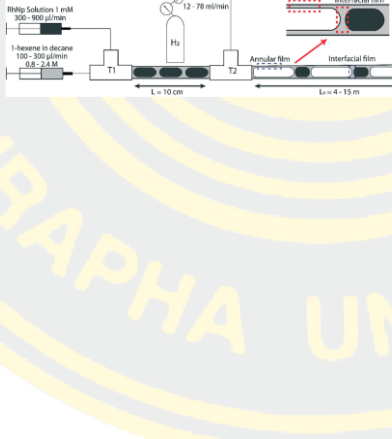
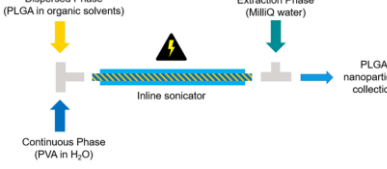
2.7 Application of continuous flow chemistry in pharmaceutical formulation of nanoparticles

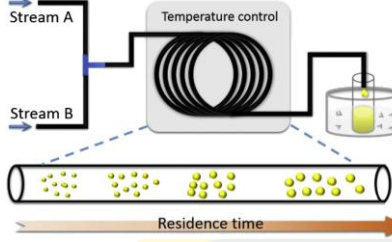
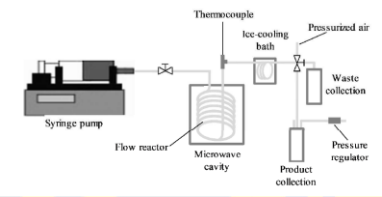
Different continuous flow chemistry setting-up in pharmaceutical formulation of nanoparticles, as outlined in Table 7, play a pivotal role in synthesis processes. Their design and operation can significantly influence the efficiency and effectiveness of nanoparticle synthesis. Continuous flow reactors have gained widespread usage in the pharmaceutical industry due to their capability to control reaction conditions and achieve high reaction efficiencies. Each reactor type possesses

a unique mechanism, along with its own set of advantages and disadvantages, which should be thoughtfully evaluated when choosing the most suitable reactor for a given process (49). Ultimately, the selection of the optimal reactor type will hinge on specific requirements such as desired reaction kinetics, reactant mixing, and product purity within the reaction.

Table 7 The continuous flow chemistry setting-up in pharmaceutical formulation of nanoparticle.

Type of reactor	Schematic	Working mechanism	Nanoparticle synthesis application	Advantages and limitations
Continuous Flow Microreactors		<p>Reactants are continuously fed into the reactor, and nanoparticles are continuously produced as they flow through the reactor.</p>	<p>Irinotecan-loaded Lipid-Polymer Nanoparticles (50)</p>	<p>This approach involves the use of microreactors, which are small devices that allow for precise control of reaction conditions.</p>
Segmented Flow Microreactors		<p>In segmented flow microreactors, the reactants are separated into discrete segments, which are then mixed together to initiate the reaction.</p>	<p>Iron oxide nanoparticles (51)</p>	<p>This approach can be useful for controlling the size and shape of nanoparticles, as well as for producing uniform batches of nanoparticles</p>
Droplet-based Microreactor		<p>This approach involves the use of droplets, which are small, discrete volumes of liquid that are suspended in an immiscible fluid.</p>	<p>Itraconazole nanoparticles (52)</p>	<p>By controlling the size and composition of these droplets, it is possible to control the size and composition of the resulting nanoparticles.</p>

Photochemical Flow Synthesis		In this approach, nanoparticles are synthesized using photochemistry, which involves the use of light to initiate the reaction.	Single chain polymer nanoparticles (53)	Controlling the intensity and wavelength of the light, it is possible to control the size and composition of the resulting nanoparticles.
Electrochemical Flow Synthesis		In this approach, nanoparticles are synthesized using electrochemistry, which involves the use of an electric current to initiate the reaction.	L-ascorbic acid loaded Gold (54)	By controlling the voltage and current, it is possible to control the size and composition of the resulting nanoparticles.
Gas-Liquid Segmented Flow		This approach involves using a gas to create discrete bubbles or droplets that contain the reactants. These bubbles or droplets are then mixed together to initiate the reaction.	Rhodium nanoparticle catalyst (55)	This technique can be useful for producing nanoparticles with a high degree of control over their size and composition.
Sonication-Assisted Flow Synthesis		In this approach, ultrasonic waves are used to initiate and drive the nanoparticle synthesis reaction.	Ritonavir and celecoxib loaded PLGA nanoparticle (56)	The sonication waves help to break down larger reactant molecules and promote the formation of nanoparticles.

<p>Continuous Flow Hydrothermal Synthesis</p>		<p>In this approach, reactants are continuously fed into a high-temperature, high-pressure reactor, where they undergo hydrothermal synthesis to form nanoparticles.</p>	<p>5-Fu loaded UiO-66 nanoparticle (57)</p>	<p>This technique is particularly useful for synthesizing nanoparticles with a high degree of crystallinity and purity.</p>
<p>Microwave-Assisted Flow Synthesis</p>		<p>This technique involves using microwave radiation to heat and initiate the reaction between the reactants.</p>	<p>Gold nanoparticle (58)</p>	<p>The use of microwaves can increase the reaction rate and produce nanoparticles with a narrower size distribution.</p>

3. Computation fluid dynamic

Computational Fluid Dynamics (CFD) is a numerical technique used to simulate fluid flow phenomena by utilizing numerical methods and computers to solve the Navier-Stokes equations, which are a set of partial differential equations consisting of the equations of mass conservation, momentum, and energy conservation. This technique allows for the prediction and study of fundamental phenomena by considering important variables, eliminating insignificant and can simulate complex flows such as turbulent and high-speed flows with high pressure.

The governing equations are written in the form of conservation equations, which is applicable to steady-state and incompressible fluid flows in two dimensions. The conservation equations consist of the continuity equation and the momentum equation, which includes the conservation of mass, momentum, and energy. The equations are solved using numerical techniques such as the finite difference method or the finite element method, which transform the partial differential equations into algebraic equations, making it easier to obtain results (59).

In this study, CFD proves invaluable in scrutinizing the mixing efficiency and flow characteristics within designed reactors. By allowing for the comprehensive visualization of intricate fluid dynamics, CFD affords researchers insights into streamline formation and behavior crucial for understanding mixing efficiency. One of its primary advantages lies in aiding the optimization of reactor design through virtual evaluations of different configurations, thereby streamlining the quest for improved mixing efficiency. Sensitivity analyses conducted through CFD enable researchers to identify and fine-tune the factors influencing mixing, contributing to the design's precision. The time and cost efficiency offered by CFD simulations prove particularly advantageous, allowing for the exploration of diverse operational conditions and design variations without the need for extensive physical experiments. Additionally, CFD offers a detailed understanding of fluid dynamics, aiding in the identification of mechanisms crucial for effective mixing. The flexibility of CFD allows for the variation of boundary conditions, simulating scenarios with altered inlet flow rate, or other fluid parameters to assess their impact on system performance. Moreover, the validation and verification of CFD simulations against experimental data enhance confidence in the accuracy and applicability of the obtained results, consolidating CFD's role as a powerful tool for comprehensively studying and improving designed reactor (60).

3.1 Governing equation of fluid dynamic

In turbulent flow, variables such as viscosity (μ), velocity (v), or pressure (p) have non-constant values and change over time (Figure 12), making the calculation of these variables complicated. Therefore, the Reynolds decomposition principle is used to assume various properties in the case of turbulent flow. It is divided into 2 parts: 1. The average value of the variable does not depend on time, such as u , v or p . 2. The part that represents the fluctuation of the variable, which is a time-dependent value, such as u' , v' or p' (61).

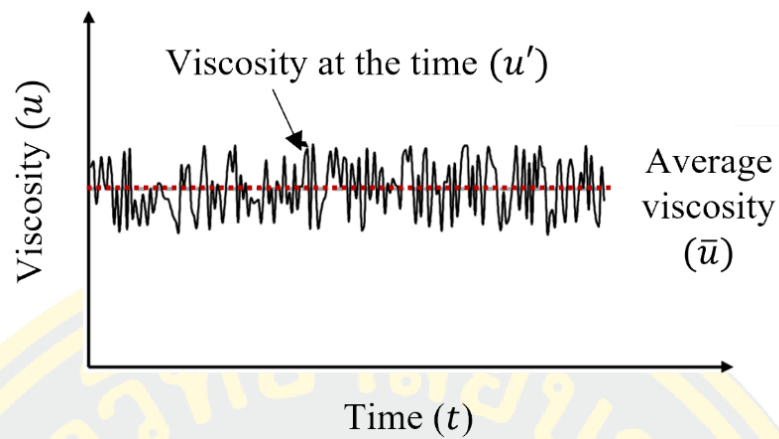


Figure 12 The fluctuation of the viscosity in turbulent flow. (Yucheng Liu et.al., 2011)

By expressing the basic equation of unsteady flow as a continuity equation and momentum equation in tensor form, we can write them as follows:

Continuity Equation;

$$\frac{\partial}{\partial x_i} (\rho u_i) = 0 \quad (10)$$

Momentum Equation;

$$\frac{\partial}{\partial x_j} (\rho u_i u_j) = -\frac{\partial p}{\partial x_i} + \frac{\partial}{\partial x_j} \left[\mu \left(\frac{\partial u_i}{\partial x_j} + \frac{\partial u_j}{\partial x_i} \right) \right] \quad (11)$$

where; ρ is the density of fluid,
 u is the fluid velocity,
 p is the pressure,
 μ is fluid viscosity.

From Reynolds decomposition, the function (f) of variables consisting of the mean value (\bar{f}) and the fluctuation component (f') can be calculated as follows:

$$f = \bar{f} + f' \quad (12)$$

The function of time-averaging can be written as follows.

$$\bar{f}(x) = \lim_{T \rightarrow \infty} \frac{1}{T} \int_t^{t+T} f(x, t) dt \quad (13)$$

After the time-averaging function is performed, the average value of the fluctuation component will be zero ($\overline{f'} = 0$) The average value of the product of two variables will be $\overline{fg} = \overline{f} \overline{g} + \overline{f'g'}$ if time-averaging is performed. This can be applied to the continuity equation and momentum equation.

$$\frac{\partial \bar{u}_i}{\partial x_i} = 0 \quad (14)$$

$$\rho \bar{u}_j \frac{\partial \bar{u}_i}{\partial x_i} = -\frac{\partial \bar{p}}{\partial x_i} + \frac{\partial}{\partial x_j} \left[\mu \left(\frac{\partial \bar{u}_i}{\partial x_j} + \frac{\partial \bar{u}_j}{\partial x_i} \right) \right] + \frac{\partial \tau_{ij}}{\partial x_j} \quad (15)$$

Equations 14 and 15 are called Reynolds-Averaged Navier-Stokes (RANS) equations. It can be observed that Equation 15 has the same form as Equation 11 except for the addition of the Reynolds stresses term ($\tau_{ij} = -\overline{\rho u'_i u'_j}$) arising from turbulent flow. This term τ_{ij} makes it impossible to solve both conservation equations together due to the large number of variables involved. Therefore, it is necessary to use a turbulence model to aid in the calculation (62).

3.2 Turbulence model

The Reynolds stress that cannot be calculated in the aforementioned equations using the continuity and Reynolds-averaged Navier-Stokes equation (RANS) will be computed using a turbulence model. The computation only considers the average flow. This study uses the Standard k- ϵ model, which is a model developed

by Launder and Spalding (1974) and employs the Boussinesq Approximation technique to find the Reynolds stress value (63), as shown in equations 16.

$$-\rho \overline{u'_i u'_j} = -\frac{2}{3} \rho k \delta_{ij} + \mu_t \left(\frac{\partial \bar{u}_i}{\partial x_j} + \frac{\partial \bar{u}_j}{\partial x_i} \right) \quad (16)$$

$$\mu_t = \rho C_\mu \frac{k^2}{\varepsilon} \quad (17)$$

The μ_t is the turbulent viscosity and can be calculated from equation 18 with the constant $C_\mu = 0.09$, where k is the turbulent kinetic energy ($k = \frac{1}{2} \overline{u'_i u'_i}$) and the term ε represents the rate of turbulent dissipation.

$$\rho \bar{u}_j \frac{\partial \bar{u}}{\partial x_i} = -\frac{\partial \bar{p}^*}{\partial x_i} + \frac{\partial}{\partial x_j} \left[\mu_{eff} \left(\frac{\partial \bar{u}_i}{\partial x_j} + \frac{\partial \bar{u}_j}{\partial x_i} \right) \right] \quad (18)$$

The terms Modified pressure (p^*) and Effective viscosity (μ_{eff}) can be defined by the equations 19.

$$p^* = p + \frac{2}{3} \rho k, \quad \mu_{eff} = \mu + \mu_t \quad (19)$$

3.2.1 Turbulent kinetic energy (k)

The equation for turbulent kinetic energy (k) is the energy per unit mass of turbulent fluctuation, which can be obtained from equation 20 as:

$$k = \frac{1}{2} \overline{u'_i u'_i} = \frac{1}{2} \left(\overline{u'^2} + \overline{v'^2} + \overline{w'^2} \right) \quad (20)$$

From the Reynolds-Averaged Navier-Stokes (RANS) equation (equation 16), when density (ρ) is divided on both sides of the equation and the equation is rearranged, the following is obtained:

$$\bar{u}_j \frac{\partial \bar{u}_i}{\partial x_i} = -\frac{1}{\rho} \frac{\partial \bar{p}}{\partial x_i} + \frac{\partial}{\partial x_j} \left[\nu \left(\frac{\partial \bar{u}_i}{\partial x_j} + \frac{\partial \bar{u}_j}{\partial x_i} \right) \right] + \frac{\partial \overline{u'_i u'_j}}{\partial x_j} \quad (21)$$

The different terms in the derivative equation of k can be used to create a complex and realistic model of turbulent kinetic energy (k) by specifying the Eddy viscosity (ν_t) as follows:

$$\nu_t \propto L \sqrt{k} \quad (22)$$

where; L is the length scale,

\sqrt{k} is the turbulent velocity fluctuation.

The equation for turbulent kinetic energy (k) can be obtained by multiplying u'_i throughout the Navier-Stokes equation and the RANS equation, and then subtracting the results of both equations and rearranging the terms as follows:

$$\underbrace{\bar{u}_j \frac{\partial k}{\partial x_j}}_{(1)} = - \underbrace{\frac{\partial}{\partial x_j} \left(\frac{1}{2} \overline{u'_j u'_i u'_i} \right)}_{(2)} - \underbrace{\nu \frac{\partial k}{\partial x_j}}_{(3)} + \underbrace{\frac{\overline{p' u'_j}}{\rho}}_{(4)} - \underbrace{\overline{u'_i u'_j} \frac{\partial \bar{u}}{\partial x_j}}_{(5)} - \underbrace{\nu \frac{\partial \bar{u}}{\partial x_j} \frac{\partial \bar{u}}{\partial x_j}}_{(6)} \quad (23)$$

where the meaning of each term is:

Term (1): Convection transport term of k ,

Term (2): Diffusion transport term of k ,

Term (3): Viscosity diffusion,

Term (4): Pressure-strain correlation,

Term (5): Production of k represented by the symbol P ,

Term (6): Dissipation of k represented by the variable ε .

Therefore, from the assumption of Gradient-Diffusion, we can simulate the turbulent diffusion and dissipation rate as follows:

$$-\frac{1}{2} \overline{u'_j u'_l u'_l} = \frac{v_i}{\sigma_k} \frac{\partial k}{\partial x_j} \quad (24)$$

where σ_k is the Prandtl-Schmidt number ≈ 1.0 , which normally assumes that the term for pressure diffusion $(-\frac{\overline{p'u'_j}}{\rho})$ is included in this term.

3.2.2 Dissipation rate (ε)

The equation for dissipation rate (ε) and the transport equation for ε can be found by defining the equation according to the Navier-Stokes equation. From this definition, it is found that the transport equation is very complex. However, it can be simplified. For two-equation models, there are other variables besides ε . These variables are categorized as follows:

$$\phi = k^m L^n \quad (25)$$

This variable can be used in the general equation as follows:

$$\bar{u}_j \frac{\partial \phi}{\partial x_i} = \frac{\partial}{\partial x_i} \left(\frac{v_t}{\sigma_\phi} \frac{\partial \phi}{\partial x_i} \right) + C_{\phi 1} \frac{\phi}{k} P - C_{\phi 2} \phi \frac{\sqrt{k}}{L} \quad (26)$$

For the k - ε model, ε can be defined by the equation:

$$\varepsilon = \frac{k^{\frac{3}{2}}}{L} \quad (27)$$

Substituting the variable Φ in the general equation 26 with ε , the equation for ε for high Reynold is obtained as follows:

$$\underbrace{\bar{u}_j \frac{\partial \varepsilon}{\partial x_i}}_{(1)} = \underbrace{\frac{\partial}{\partial x_i} \left(\frac{v_t}{\sigma_\varepsilon} \frac{\partial \varepsilon}{\partial x_i} \right)}_{(2)} + \underbrace{C_{\varepsilon 1} \frac{\varepsilon}{k} P}_{(3)} - \underbrace{C_{\varepsilon 2} \phi \frac{\varepsilon^2}{L}}_{(4)} \quad (28)$$

The various terms in equation (28) have the following physical meanings:

Term (1): Convection transport term of ε .

Term (2): Turbulent diffusion term.

Term (3): Production term of ε .

Term (4): Dissipation term of ε .

The production rate is related to turbulence energy, and the dissipation rate is given in a simple form as ε /turbulence time scale, where the time scale is a ratio of k / ε .

The constant value of the model from turbulence decay allows for a reduction of the equations k and ε to be as follows:

$$\bar{u} \frac{\partial k}{\partial x} = -\varepsilon \quad \text{and} \quad \bar{u} \frac{\partial \varepsilon}{\partial x} = -C_{s2} \frac{\varepsilon^2}{k} \quad (29)$$

The decrease of k is in the form of Power law ($k \propto x^{-n}$) where:

$$C_{s2} = \frac{n+1}{n} \quad (30)$$

Near the wall, the equation shown as:

$$P \approx \varepsilon, k \approx \frac{u_\tau^2}{\sqrt{C_u}}, \varepsilon = \frac{u_\tau^3}{\kappa y}, v_\tau = C_\mu \frac{k^2}{\varepsilon} \quad (31)$$

The equation for ε can be reduced as follows:

$$0 = \frac{\partial}{\partial x_i} \left(\frac{v_\tau}{\sigma_\varepsilon} \frac{\partial \varepsilon}{\partial x_j} \right) + C_{s2} \frac{\varepsilon}{k} P - C_{s2} \frac{\varepsilon^2}{k} \quad (32)$$

The relationship between $C_{\varepsilon 1}$ and $C_{\varepsilon 2}$ can be determined as follows:

$$C_{\varepsilon 1} = C_{\varepsilon 2} - \frac{\kappa^2}{\sigma_\varepsilon \sqrt{C_u}} \quad (33)$$

For the standard $k-\varepsilon$ model, calculations and experiments have been conducted to determine the standard constants used in the calculations as follows: $C_u=0.09$, $\sigma_k=1.0$, $\sigma_\varepsilon=1.3$, $C_{\varepsilon 1}=1.44$ and $C_{\varepsilon 2}=1.44$ (61). Therefore, the basic equation used to calculate general fluid flow in CFD programs can be summarized in Table 8.

Table 8 Summarized equation for CFD calculation.

Transport equation	Differential form
Continuity	$\frac{\partial}{\partial x_i} (\rho u_i) = 0$
Momentum	$\frac{\partial}{\partial x_j} (\rho u_i u_j) = -\frac{\partial p}{\partial x_i} + \frac{\partial}{\partial x_j} \left[\mu \left(\frac{\partial u_i}{\partial x_j} + \frac{\partial u_j}{\partial x_i} \right) \right]$

Turbulent kinetic energy	$\overline{\rho u_j \frac{\partial k}{\partial x_j}} = \frac{\partial}{\partial x_j} \left\{ \frac{\mu_t}{\sigma_k} \frac{\partial k}{\partial x_j} \right\} + P - \rho \varepsilon$
Dissipation rate	$\overline{\rho u_j \frac{\partial \varepsilon}{\partial x_j}} = \frac{\partial}{\partial x_j} \left\{ \frac{\mu_t}{\sigma_\varepsilon} \frac{\partial \varepsilon}{\partial x_j} \right\} + C_{\varepsilon 1} \frac{\varepsilon}{k} P - C_{\varepsilon 2} \rho \frac{\varepsilon^2}{k}$
Boussinesq approximation	$-\overline{\rho u_i u_j} = -\frac{2}{3} \rho k \delta_{ij} + \mu_t \left(\frac{\partial \overline{u_i}}{\partial x_j} + \frac{\partial \overline{u_j}}{\partial x_i} \right)$

3.3 Discretization method

The discretization method is used to solve linear equation systems by using numerical methods to obtain the solution. The discretization methods for solving computational fluid dynamics problems are as follows (59).

3.2.1 Finite volume method

The finite volume method is a standard method for developing software for solving fluid flow problems. The governing equations are solved by discretizing the control volume into discrete control volumes, and then integrating to obtain the conserved quantity as follows:

$$\frac{\partial}{\partial t} \iiint Q dV + \iint F dA = 0 \quad (34)$$

where; Q is the vector of conserved variables,

F is the vector of fluxes,

V is the volume of the cell,

A is the surface area of the cell.

3.2.2 Finite element method

The finite element method serves as a powerful numerical technique for conducting flow simulations. The process begins by establishing the governing equations, typically the Navier-Stokes equations, which describe the conservation of

mass, momentum, and thermal energy. To make these equations amenable to finite element method, they are transformed into their weak forms by integrating with weight functions. The computational domain is then discretized into smaller elements, connected at nodes, and assigned interpolation functions to approximate fluid behavior. Assembling these elements results in a global matrix equation, which is solved to obtain velocity and pressure fields. Post-processing techniques are applied to visualize flow patterns, calculate flow rates, and evaluate pressure distributions. finite element method can be extended to tackle complex scenarios such as multiphase flows, turbulence, and heat transfer. By providing a comprehensive and versatile approach to flow simulation, finite element method contributes significantly to the understanding and optimization of fluid dynamics in a wide range of engineering systems.

3.2.3 Finite difference method

The finite difference method uses a structured mesh and a coordinate transformation for complex shapes in the calculation as follows:

$$\frac{\partial Q}{\partial t} + \frac{\partial F}{\partial x} + \frac{\partial G}{\partial y} + \frac{\partial H}{\partial z} = 0 \quad (35)$$

where; Q is the vector of conserved variables.

F , G , and H are the fluxes in the x , y , and z directions, respectively.

3.4 Steps in flow simulation

3.4.1 Creating a 3D model involves defining the physical boundaries of the object, which can be done by various computer-aided design (CAD) programs. The model is then created by using a mathematical model to generate the parts. This generated part is called a model.

3.4.2 Mesh generation is the process of defining points to create a grid for analysis. The model is divided into small, contiguous volume elements. The grid has two types: tetrahedral (Figure 13a) is suitable for curved surfaces, and hexahedral

(Figure 13b) is suitable for flat surfaces. The grid's accuracy can affect the accuracy and precision of the results, but it may also require more time and a high memory computer. Conversely, a less accurate grid may require less processing time and a lower memory computer, but the result may not be as accurate. Therefore, selecting the appropriate grid accuracy is crucial because it considers both processing time and the accuracy of the results. The results must be as close to the actual answer as possible or within acceptable limits.

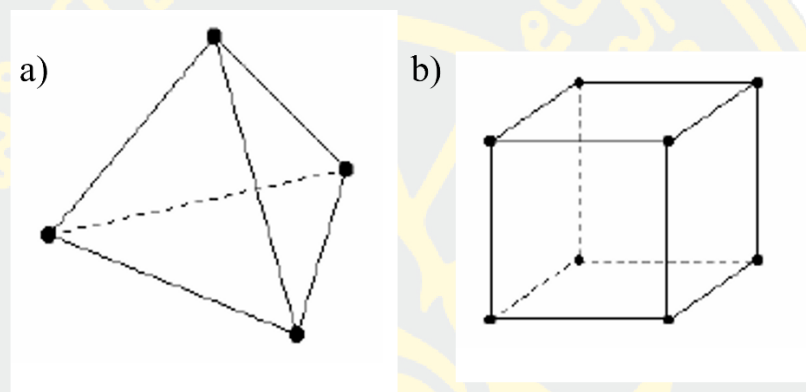


Figure 13 Type of CFD meshing of (a) tetrahedral grid and (b) hexahedral grid (Gullberg R. et.al., 2017)

Defining the characteristics of a mesh affects the accuracy and stability of the calculations, and the arrangement of the mesh depends on the flow pattern. For example, the inlet area should have a mesh that is consistent with the actual flow field to reduce errors in that region. Therefore, arranging a mesh that is regular and appropriate for the flow path is highly important (64).

3.4.3 Defining the fluid properties such as fluid types, density, viscosity, and thermal conductivity. These properties are crucial for accurate modeling.

3.4.4 Boundary conditions refer to setting conditions that determine the values of the variables and their sub-derivatives, which are derivatives in the direction of vectors. Boundary conditions are known values for CFD calculations (65) and can be defined as follows:

3.4.4.1 Flow openings, which define the vector quantity of the flow in the area with flow in and out. They can be defined in the form of mass flow, mass flux, volume flow, or velocity, as well as specifying the properties of the flow, thermodynamic parameters, and turbulence parameters.

3.4.4.2 Pressure openings, which determine the pressure characteristics in a known area. They can be defined as environmental pressure, static pressure, or total pressure, as well as specifying the thermodynamic parameters used in the calculation.

3.4.4.3 Wall characteristics are defined as the characteristics of the workpiece walls before the calculation, which can be defined in terms of thermal properties, thermal conductivity, and roughness. Additionally, the turbulence and heat transfer coefficients can be specified.

3.4.5 *Defining the equations* for physical modeling, the magnetohydrodynamics simulation is often related to the aforementioned control equations. Navier-Stokes equations for incompressible flow was selected and settled-up the appropriate governing equations to describe the fluid flow.

3.4.5 *Simulation run* allows the software to numerically solve the governing equations, which may involve steady-state or transient analysis, depending on the nature of the problem. The simulation concludes when convergence is achieved.

4. 3D printing technology

3D printing is a manufacturing process that creates three-dimensional objects from a digital file or CAD model by layering materials such as plastic, metal, or even food in a precise and controlled manner. The process involves slicing the digital file into thin layers and then using a 3D printer to build the object layer by layer (66). In this review, we will delve into the fundamental mechanism, explore the advantages, and discuss the limitations of several types of 3D printing technologies.

4.1 VAT polymerization

VAT polymerization, or VAT photopolymerization, is a widely used technique in additive manufacturing, commonly known as 3D printing. This method relies on the principle of selectively curing liquid resin layer by layer to create intricate three-dimensional objects, as illustrated in Figure 14.

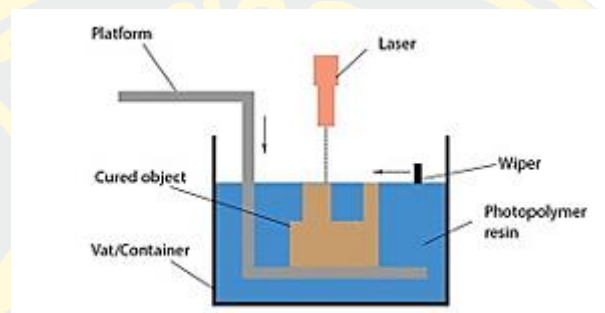


Figure 14 VAT polymerization (Zhang J et al., *Advanced Powder Technology*, 2021, 32.9: 3324-3345.)

4.1.1 Principle mechanism

VAT polymerization operates on the basis of photopolymerization, a process in which liquid resin is transformed into a solid state through the application of light. The typical setup involves a VAT containing liquid resin and a build platform. A light source, often an ultraviolet (UV) laser or projector, is used to selectively cure the resin layer by layer as follows:

- 1) Layer formation: The process begins with the creation of a thin layer of liquid resin on the build platform.
- 2) Selective curing: The UV light source is then precisely directed to specific areas, causing the resin to solidify. This selective curing is determined by a digital model, which guides the light source to cure the resin according to the desired object geometry.
- 3) Layer-by-layer building: The build platform is incrementally lowered, and the process is repeated, layer by layer, until the entire object is formed.
- 4) Finalization: After the completion of the printing process, excess resin is drained or removed, leaving behind the solidified 3D printed object.

4.1.2 Advantages

- 1) High resolution: VAT polymerization is known for its ability to produce high-resolution prints with fine details. The layer thickness can be minimized, resulting in smoother surfaces and intricate features.
- 2) Diverse materials: This technique is compatible with a variety of photopolymer resins, allowing for the production of objects with different mechanical properties, colors, and finishes.
- 3) Accuracy and precision: VAT polymerization offers precise control over the curing process, enabling the creation of complex structures and intricate designs with a high degree of accuracy.
- 4) Speed: Compared to some other 3D printing technologies, VAT polymerization can be relatively fast, especially for small to medium-sized objects.

4.1.3 Limitations

- 1) Material limitations: The range of available photopolymer resins may be limited compared to other 3D printing methods. This can constrain the mechanical properties and application versatility of the printed objects.
- 2) Post-processing requirements: Residual uncured resin may remain on the printed object, necessitating thorough post-processing steps, such as cleaning and curing, to achieve the desired final properties.
- 3) Build size constraints: The size of the 3D printed object is often restricted by the size of the vat and the build platform, limiting the scalability of VAT polymerization for larger objects.
- 4) Cost of equipment: High-quality VAT polymerization equipment, including UV light sources and precision components, can be expensive, making the initial investment a significant consideration for potential users.

VAT polymerization stands out as a powerful 3D printing technology with its ability to produce highly detailed and accurate objects. While it offers various advantages, such as high resolution and diverse material options, it is essential to be mindful of its limitations, including material constraints and post-processing requirements. As technology continues to evolve, addressing these limitations could further enhance the applicability of VAT polymerization in various industries (67).

4.2 Material extrusion

Material extrusion, also known as fused filament fabrication (FFF) or fused deposition modeling (FDM), is a popular 3D printing technology that utilizes the principle of layer-by-layer material deposition, as illustrated in Figure 15.

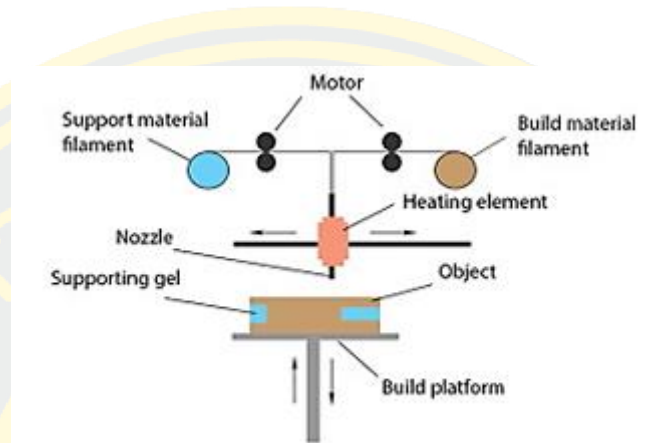


Figure 15 Material extrusion (Zhang J et al., *Advanced Powder Technology*, 2021, 32.9: 3324-3345.)

4.2.1 Principle mechanism

Material extrusion operates on a simple yet effective mechanism. The process begins with a thermoplastic filament, typically in spool form, which is fed into a heated nozzle. The filament is melted within the nozzle, and the liquefied material is extruded onto a build platform in a precise pattern determined by a digital model as follows:

- 1) Filament feed: The thermoplastic filament is fed into the heated nozzle.
- 2) Melting: The nozzle, heated to the melting temperature of the filament, melts the material, turning it into a viscous liquid.
- 3) Layer-by-layer deposition: The liquefied material is extruded through a nozzle orifice onto the build platform, creating a single layer of the object being printed.
- 4) Build platform movement: The build platform is lowered, and the process is repeated, layer by layer, until the entire object is formed.

5) Cooling and solidification: As each layer is deposited, it quickly cools and solidifies, bonding with the previous layers.

4.2.2 Advantages

1) Wide material compatibility: Material extrusion supports a variety of thermoplastic materials, offering users flexibility in choosing materials with different mechanical properties, colors, and purposes.

2) Affordability and accessibility: FDM printers are often more affordable and accessible for personal and professional use, making them a popular choice for hobbyists and small businesses.

3) Ease of use: The technology is relatively simple to understand and operate, making it suitable for users of various skill levels.

4) Large build volume: FDM printers are available in a range of sizes, allowing for the fabrication of objects with significant dimensions.

4.2.3 Limitations

1) Layer resolution: The layer-by-layer deposition can result in visible layer lines on the final print, potentially affecting the surface finish and detail level, especially when compared to technologies with finer resolutions.

2) Overhangs and supports: Printing overhangs or intricate structures may require additional support structures, which must be manually removed after printing.

3) Mechanical anisotropy: The mechanical properties of printed objects can vary depending on the orientation of the printed layers, leading to anisotropic behavior.

4) Post-processing considerations: Depending on the material used, post-processing steps such as sanding or smoothing may be necessary to achieve the desired surface finish.

Material extrusion, with its straightforward mechanism and versatility in material selection, has established itself as a prominent 3D printing technology. While it may have some limitations, such as layer resolution and mechanical anisotropy, the advantages of affordability, accessibility, and ease of use make material extrusion an excellent choice for a wide range of applications, from rapid prototyping to functional part production. As technology continues to advance, addressing these limitations may

further enhance the capabilities of Material Extrusion in the 3D printing landscape (68).

4.3 Material jetting

Material jetting is a sophisticated 3D printing technology that enables the creation of highly detailed and multi-material objects, as illustrated in Figure 16.

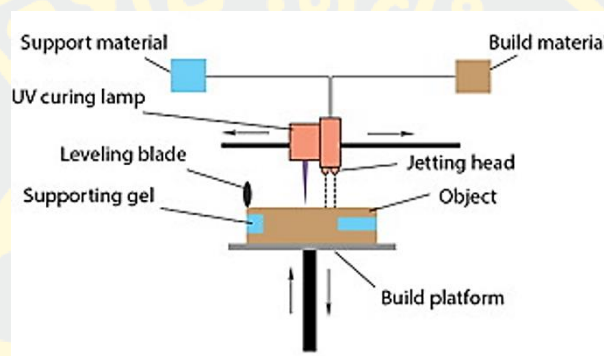


Figure 16 Material jetting (Zhang J et al., *Advanced Powder Technology*, 2021, 32.9: 3324-3345.)

4.3.1 Principle mechanism

Material jetting operates on the principle of jetting or spraying tiny droplets of photopolymer materials onto a build platform. The process involves the use of multiple printheads, each containing a different material or a combination of materials. These droplets are rapidly cured, typically using UV light, creating solid layers that build up the 3D object as follows:

- 1) Material reservoirs: Material jetting systems have multiple reservoirs containing different photopolymer materials.
- 2) Printhead jetting: The printheads precisely jet tiny droplets of liquid material onto the building platform according to the digital model.
- 3) Curing: The deposited material is rapidly cured using UV light, solidifying the layer.

4) Layer-by-layer building: The process is repeated layer by layer, with the ability to switch between materials during printing, allowing for the creation of multi-material and multi-color objects.

5) Support material jetting: Material jetting systems can also use a separate support material that is later removed, enabling the creation of complex geometries and overhangs.

4.3.2 Advantages

1) High resolution: Material jetting can achieve extremely high levels of detail, producing smooth surfaces and intricate features.

2) Multi-material printing: The ability to jet multiple materials during a single print allows for the creation of objects with varying mechanical properties, colors, and translucencies in a single build.

3) Color printing: Some material jetting systems can produce full-color prints, allowing for the creation of visually appealing prototypes and models.

4) Accuracy and precision: Material jetting provides excellent accuracy, making it suitable for applications where precision is crucial, such as dental and medical models.

4.3.3 Limitations

1) Material cost: The materials used in material jetting can be expensive, potentially limiting its cost-effectiveness for certain applications.

2) Build speed: Material jetting may have longer print times compared to other technologies, especially when intricate details and multiple materials are involved.

3) Post-processing requirements: Depending on the system, post-processing steps like support removal and curing may be required, adding to the overall production time.

4) Equipment cost: Material jetting printers can be relatively expensive, making them more suitable for professional and industrial applications.

Material Jetting stands out as a cutting-edge 3D printing technology, offering unparalleled precision and the ability to create complex, multi-material objects with high detail. While it may have limitations in terms of cost and build speed, the advantages, particularly in accuracy and multi-material capabilities, make Material

Jetting a valuable choice for applications that demand exceptional quality and customization. As technology continues to evolve, addressing these limitations could further expand the range of applications for Material Jetting in various industries (69).

4.4 Binder jetting

Binder jetting is a versatile 3D printing technology that utilizes a powder-based approach for creating objects layer by layer, as illustrated in Figure 17.

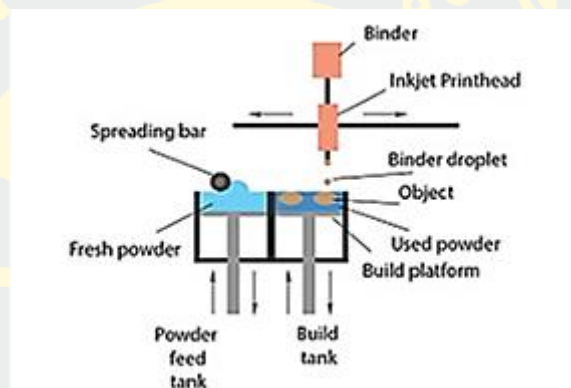


Figure 17 Binder jetting (Zhang J et al., *Advanced Powder Technology*, 2021, 32.9: 3324-3345.)

4.4.1 Principle mechanism

Binder jetting operates by selectively depositing a liquid binding agent onto a powder bed. The binding agent causes the powder particles to adhere and solidify, forming the desired layer of the 3D object. The process is repeated, layer by layer, until the entire object is created as follows:

- 1) Powder bed: A layer of fine powder (such as metal, polymer, or ceramic) is spread evenly on the build platform.
- 2) Binder application: The printer selectively jets a liquid binding agent onto the powder bed, binding the particles together to form the current layer of the object.

3) Layer compaction: After the binder is applied, a roller or another mechanism may be used to compact the powder layer, enhancing its structural integrity.

4) Repeating process: Steps 1-3 are repeated for each layer until the entire 3D object is formed within the powder bed.

5) Post-processing: After printing is complete, the object is typically removed from the loose powder, and any excess powder is brushed or blown off. Additional post-processing steps, such as sintering or infiltrating, may be required to achieve the desired material properties.

4.4.2 Advantages

1) Material versatility: Binder jetting supports a wide range of materials, including metals, ceramics, and polymers, providing versatility for various applications.

2) Speed: Binder jetting can be relatively fast, especially for large and geometrically simple objects, as multiple layers can be printed simultaneously.

3) Economical use of materials: The powder-based approach allows for efficient use of material, reducing waste compared to other technologies.

4) Complex geometries: Binder jetting is capable of producing intricate and complex geometries that may be challenging for other manufacturing methods.

4.4.3 Limitations

1) Resolution: While binder jetting is capable of producing high-quality parts, it may have limitations in terms of resolution compared to some other 3D printing technologies.

2) Surface finish: The surface finish of binder jetting parts may not be as smooth as parts produced using other methods, requiring additional post-processing for certain applications.

3) Mechanical properties: The final mechanical properties of binder jetting parts may be influenced by the post-processing steps and the material used.

4) Size constraints: The build size of binder jetting printers may be limited, particularly for certain materials and applications.

Binder jetting stands out as a versatile 3D printing technology suitable for a range of materials and applications. Its ability to produce complex geometries,

combined with its relative speed and economical use of materials, makes it a compelling choice for various industries. While it may have some limitations in terms of resolution and surface finish, the advantages offered by binder jetting position it as a valuable tool in the landscape of additive manufacturing. As technology continues to advance, addressing these limitations could further expand the scope of applications for binder jetting (70).

4.5 Powder bed fusion

Powder bed fusion (PBF) encompasses a range of additive manufacturing technologies that employ a powder bed to selectively fuse materials layer by layer, forming three-dimensional objects, as illustrated in Figure 18.

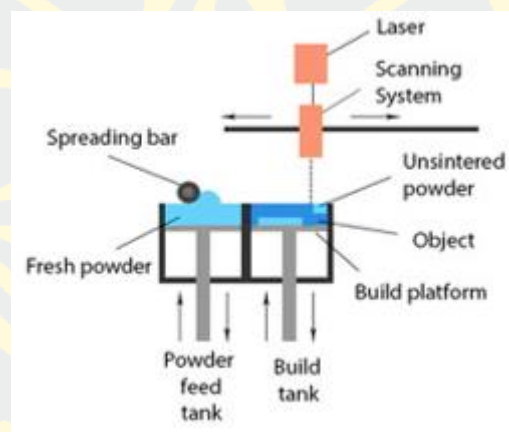


Figure 18 Powder bed fusion (Zhang J et al., *Advanced Powder Technology*, 2021, 32.9: 3324-3345.)

4.5.1 Principle mechanism

The fundamental principle of powder bed fusion involves selectively melting or sintering layers of powder material to build up a 3D object. There are various techniques within the powder bed fusion category, including selective laser sintering (SLS) and electron beam melting (EBM), each with its own specific process as follows:

- 1) Powder dispersion: A thin layer of powdered material (typically polymer, metal, or ceramic) is evenly spread across the build platform.

2) Melting: A high-powered laser in SLS or an electron beam in EBM selectively melt or sinter the powder according to the digital model, fusing the particles together to form the current layer.

3) Platform lowering: After each layer is completed, the build platform is lowered, and a new layer of powder is spread, repeating the process until the entire object is formed.

4.5.2 Advantages

1) Material versatility: PBF supports a wide range of materials, including metals, polymers, and ceramics, allowing for diverse applications in various industries.

2) Complex geometries: PBF can produce highly complex and intricate geometries with internal features that would be challenging or impossible with traditional manufacturing methods.

3) High strength and density: The fusion process in PBF results in parts with high strength and density, making them suitable for functional prototypes and end-use applications.

4) No need for support structures: Unlike some other 3D printing technologies, PBF does not require support structures for overhangs, as the unsintered powder acts as natural support.

4.5.3 Limitations

1) Equipment cost: PBF machines, especially those capable of processing metal powders, can be expensive, limiting accessibility for smaller businesses or individuals.

2) Post-processing requirements: Parts produced with PBF often require post-processing steps such as heat treatment or surface finishing to achieve the desired mechanical properties and aesthetics.

3) Powder handling: Working with fine powders can pose challenges in terms of handling, safety, and powder recovery for reuse.

4) Build size constraints: The build size of PBF machines may be limited, affecting the size of the objects that can be produced in a single print.

Powder bed fusion has emerged as a versatile and powerful 3D printing technology, offering high-quality and functional parts across a range of materials. Its

ability to produce complex geometries and parts with excellent mechanical properties positions it as a valuable tool for industries ranging from aerospace to healthcare. While there are considerations such as equipment cost and post-processing requirements, the advantages of material versatility and part strength make powder bed fusion a compelling choice for applications that demand precision and reliability. As technology continues to advance, addressing these limitations could further broaden the applicability of powder bed fusion in the evolving landscape of additive manufacturing (71).

4.6 Direct energy deposition

Direct energy deposition (DED) is an additive manufacturing technique that involves the direct deposition of material, usually in the form of powder or wire, onto a substrate using a focused energy source, as illustrated in Figure 19.

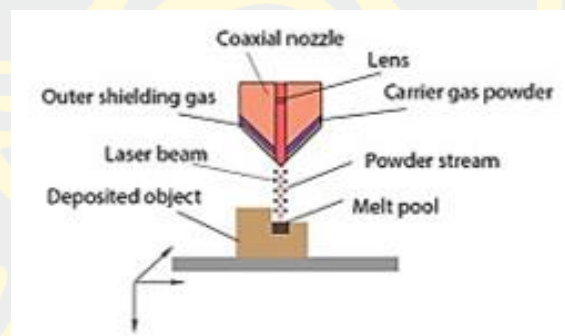


Figure 19 Direct energy deposition (Zhang J et al., *Advanced Powder Technology*, 2021, 32.9: 3324-3345.)

4.6.1 Principle mechanism

Direct energy deposition is a cutting-edge additive manufacturing technique that utilizes focused energy sources, such as lasers or electron beams, to melt and deposit material onto a substrate. The process involves feeding a continuous wire or powder feedstock into the melt pool, where it fuses with the substrate or previously deposited layers. This layer-by-layer approach allows for the creation of intricate and customized geometries with a high degree of precision as follow:

1) Material feed: Metal powder or wire is fed into the deposition nozzle.

2) Energy source activation: A focused energy source, such as a laser or electron beam, is used to melt or fuse the material as it is deposited onto the substrate.

3) Layer-by-layer building: The deposition head is controlled by a robotic arm or other automated system, allowing for precise control over the material deposition. The process is repeated layer by layer, building up the 3D object.

4) In situ processing: Some DED systems also allow for in situ processing, where additional features like machining or finishing are performed during the deposition process.

4.6.2 Advantages

1) Material versatility: DED supports a wide range of materials, including metals, polymers, and ceramics, making it versatile for various industrial applications.

2) Rapid prototyping and repair: DED is well-suited for rapid prototyping and repair applications, allowing for the quick addition of material to existing components or the creation of near-net-shape parts.

3) Large-scale printing: DED is capable of printing large-scale objects due to its inherent ability to deposit material rapidly.

4) In situ processing: The capability for in situ processing, such as machining or surface finishing during the deposition process, enhances the efficiency of DED for certain applications.

4.6.3 Limitations

1) Surface finish: The surface finish of parts produced using DED may not be as smooth as those produced using other 3D printing technologies, often requiring post-processing steps for improved aesthetics.

2) Resolution: DED may have limitations in terms of resolution compared to certain other 3D printing methods, affecting the level of detail that can be achieved.

3) Equipment size and cost: DED systems, especially those designed for large-scale applications, can be sizable and expensive, limiting accessibility for smaller businesses or individuals.

4) Material efficiency: Depending on the application, DED may have challenges with material efficiency, as excess material may need to be machined away in certain cases.

Direct energy deposition stands out as a robust and versatile 3D printing technology, well-suited for applications requiring rapid material deposition and in situ processing. While there are considerations such as surface finish and equipment cost, the advantages of material versatility, large-scale printing, and rapid prototyping make DED a valuable tool for industries ranging from aerospace to manufacturing. As technology continues to advance, addressing these limitations could further enhance the capabilities and broaden the applications of direct energy deposition in the field of additive manufacturing (72).

4.7 Sheet lamination

Sheet lamination is an innovative 3D printing technology that deviates from traditional layer-by-layer approaches, as illustrated in Figure 20.

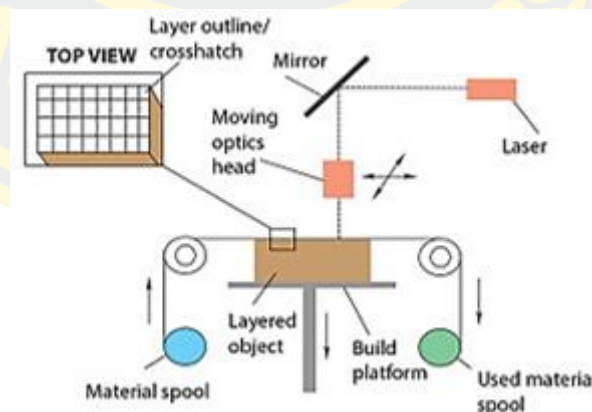


Figure 20 Sheet lamination (Zhang J et al., *Advanced Powder Technology*, 2021, 32.9: 3324-3345.)

4.7.1 Principle mechanism

At its core, sheet lamination involves the bonding of thin layers of material to create a final 3D object. Unlike some other additive manufacturing techniques, sheet lamination does not rely on melting or sintering powdered material. Instead, it utilizes sheets of material, often paper or metal, which are bonded together through various methods. One common technique is adhesive bonding, where layers are glued together to form the desired shape. Another method involves the use of heat or pressure to laminate the sheets, creating a solid structure as follows:

- 1) Layered sheet stacking: The process begins with a stack of thin sheets, typically paper or metal, representing the cross-sections of the 3D object.
- 2) Adhesive application: Adhesive is selectively applied to the sheets according to the digital model, determining where layers will adhere and where voids will exist.
- 3) Pressing and bonding: The stack of sheets is pressed together, bonding the adhesive-coated layers. This process is often performed iteratively for each layer until the complete object is formed.
- 4) Precision cutting: After bonding, excess material is precisely cut away, revealing the desired shape of the 3D object.

4.7.2 Advantages

- 1) Material variety: Sheet lamination is versatile in terms of materials, accommodating various types of sheets including paper, metal, and composites, offering flexibility for different applications.
- 2) Color and texture options: The use of colored or textured sheets allows for the creation of visually appealing and detailed objects without the need for additional post-processing.
- 3) Cost-effectiveness: Sheet lamination can be a cost-effective option, especially for certain applications and materials, as the raw materials are often readily available and less expensive.
- 4) Environmentally friendly: Depending on the materials used, sheet lamination can be environmentally friendly, particularly when utilizing recyclable or biodegradable sheet materials.

4.7.3 Limitations

1) Resolution and layer thickness: Achieving fine resolutions may be challenging in sheet lamination, as the thickness of each layer is constrained by the thickness of the sheet material.

2) Limited material strength: The strength of objects produced through Sheet Lamination can be influenced by the properties of the sheet material, potentially limiting its suitability for certain high-stress applications.

3) Post-processing complexity: While the process itself is relatively simple, post-processing steps, such as precise cutting and removal of excess material, can be intricate and time-consuming.

4) Build size constraints: The build size of objects is somewhat limited by the dimensions of the available sheet material, affecting the scalability of sheet lamination for larger projects.

Sheet lamination stands as a unique and resourceful member of the 3D printing family, offering distinct advantages in material variety, color options, and cost-effectiveness. While limitations such as resolution and material strength exist, the environmentally friendly nature and simplicity of the process make sheet lamination a compelling choice for specific applications, particularly those where intricate details and vibrant aesthetics are paramount. As technology evolves, addressing these limitations may further enhance the appeal and broaden the applications of sheet lamination in the diverse landscape of additive manufacturing (73).

CHAPTER 3

EXPERIMENTALS

1. Materials

Polyglycolic acid (PGA), lot 202201042, cosmetic grade, was purchased from Chemipan Corporation Co., Ltd. (Bangkok, Thailand). Polyvinyl alcohol (PVA), lot 12123PD, laboratory grade, was purchased from Sigma Aldrich, Inc. (St. Louis, MO, USA). Bovine serum albumin (BSA), lot SLCF8575, laboratory grade, was purchased from Sigma Aldrich, Inc. (St. Louis, MO, USA). Dipalmitoylphosphatidylcholine (DPPC), lot 580355P-1G-D-326, laboratory grade, was purchased from Avanti polar lipids (Birmingham, AL, USA). Cholesterol, lot SLCP9543, laboratory grade, was purchased from Sigma Aldrich, Inc. (St. Louis, MO, USA). Erythrosine, lot CM020031703, food grade, was purchased from Adinop Co., Ltd. (Bangkok, Thailand). Dichloromethane, lot 21-08-0094, laboratory grade, was purchased from RCI Labscan Ltd. (Bangkok, Thailand). Acetone, lot A1084-4-4001, laboratory grade, was purchased from QRëC. (Chonburi, Thailand). Ethanol, lot L1215483-220, laboratory grade, was purchased from Sigma Aldrich, Inc. (St. Louis, MO, USA). Bradford reagent, SLCP9543, laboratory grade, was purchased from Sigma Aldrich, Inc. (St. Louis, MO, USA). Polypropylene (PP) filament was obtained from B and Brothers Co., Ltd. (Samut Sakhon, Thailand).

2. The vortex tube reactor design and model development according to design of experiment

The design of a vortex tube reactor was carried out using Shapr3D software. The reactor designed for flow chemistry is composed of two main components, which are a mixer and a vortex tube reactor. The mixer part design of the reactor is shown in Figure 21. The model is composed of two inlets (4 mm in diameter), and the flow streamlines at mixer inlet 1 and inlet 2 are interconnected through a fin for mixing. The fluid flow is moved tangentially within the mixer part, and the whirling fluid flow is then forced by the fin to change direction and form a vortex streamline before

exiting the mixer through the outlet. This vortex streamline then passes through the reactor.

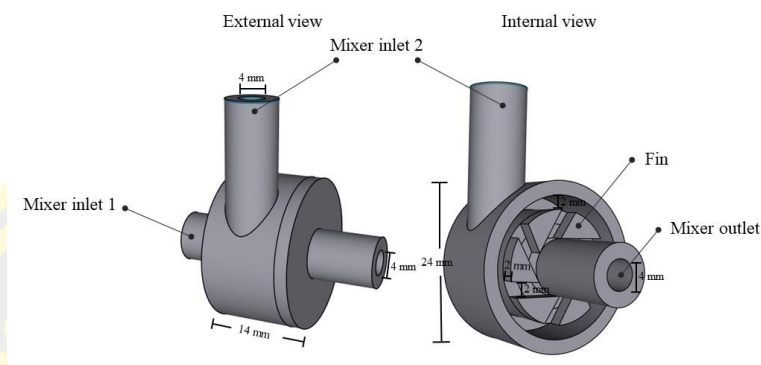


Figure 21 The designed mixer model.

The vortex tube reactor in this flow chemistry system is shown in Figure 22. The model was designed with a focus on mixing performance and flow characteristics. The reactor was designed to create a vortex streamline that enhances mixing and mass transfer, resulting in greater productivity according to the streamlines are separated to 4 ways of the by-pass tube while intended to increase fluid velocity, which creates a suitable environment for vortex mixing of the reagents inside the chamber.

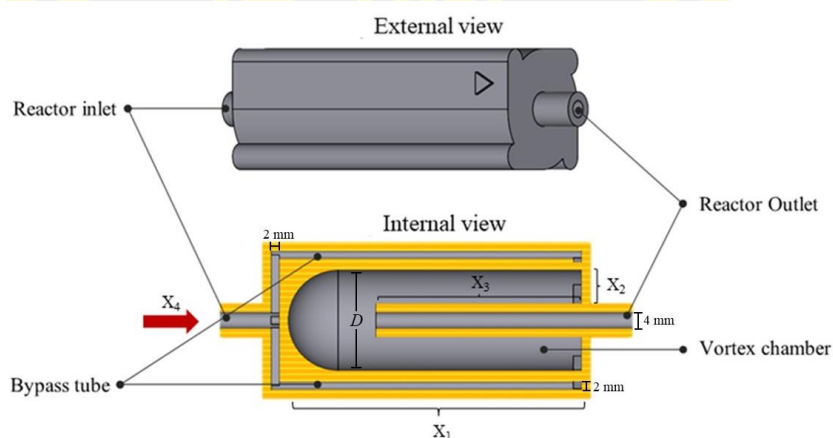


Figure 22 The designed vortex tube reactor model.

The design of the reactor and the operating parameters were studied and optimized using the experimental design (DoE), Central Composite Design. As presented in Table 9, the interest factors in this study were reactor length (X_1), internal tube to chamber wall width (X_2), percentage of internal tube length per reactor length (X_3), and total flow rate (X_4). The variable factors were determined by the maximum printed dimensions of a 3D-printer (UP Mini 2, Beijing Tiertime Technology Co., Ltd., China), and the maximum flow rate of a peristaltic pump (Sp-minipump, Shenzhen Precision Pump Co., Ltd., China). After that the experimental runs were generated and tested by CFD (flow simulation, Solidworks2021) and the following responses, including mixing index (Y_1) and Reynolds number (Y_2) were monitored and recorded.

Table 9 Factor levels based on central composite design.

Factor (X)	Unit	DoE Code				
		$-\alpha$	-1	0	1	$+\alpha$
X ₁ : Reactor length	mm	10	30	45	60	90
X ₂ : Internal tube to chamber wall width	mm	2	4	6	8	10
X ₃ : Internal tube length per reactor length	%	10	30	45	60	90
X ₄ : Total flow rate	mL/min	10	40	70	100	130

3. Numerical analysis

The mathematical models and equations were used to conduct the computational fluid dynamics (CFD) simulations. The simulations were run using the flow simulation software (Solidworks2021). These equations take into account the effects of viscosity, pressure, and density to predict the flow behavior in a particular system. The governing equations of the three-dimensional, steady, and incompressible flows are the Navier-Stokes equations which can be solved using the finite element method (FEM) or finite volume method (FVM). The Navier-Stokes equations are given by:

$$\text{Continuity equation:} \quad \nabla \cdot V = 0 \quad (36)$$

$$\text{Momentum equation:} \quad \rho \left(\frac{\partial V}{\partial t} + (V \cdot \nabla)V \right) = -\nabla P + \mu \nabla^2 V \quad (37)$$

where, V is the velocity vector,

ρ is the fluid density,

P is the pressure,

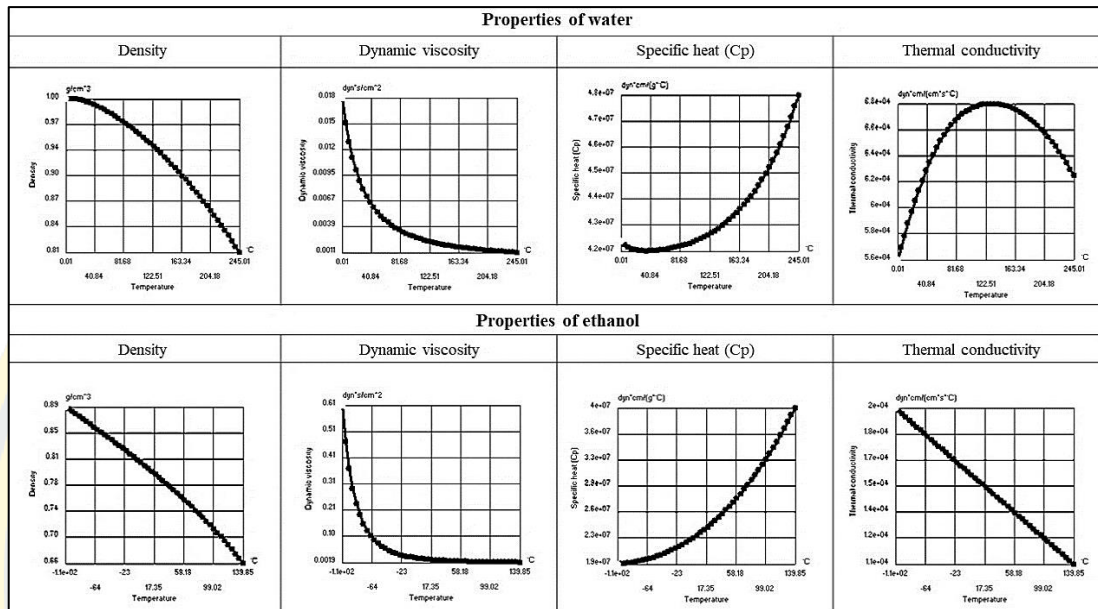
μ is the viscosity,

t is time.

The species transport model was employed as it is the most commonly used method to model the mixing of miscible fluids, taking into account the mass diffusion coefficient. The code solved the conservation equations that described the sources of convection and diffusion for each species. The local mass fraction of each species was predicted by solving the convection-diffusion equation, with the sum of the mass fractions of all species being equal to one.

The CFD code was used to solve the governing equations of three-dimensional, steady, and incompressible flows (continuity and momentum). The species transport model, which takes into account the mass diffusion coefficient, was also used. The conservation equations for each species were solved by considering convection and diffusion mechanisms. The liquid properties from the engineering database (Solidworks) in Table 10 was used for CFD calculation, and the mixing was governed mainly by chaotic advection. The boundary conditions were rigid and non-movable walls, a non-slip velocity condition, and constant uniform velocity at the inlets. The mass fraction ratio of the water to ethanol was equal to 1:0 at inlet 1 and 0:1 at inlet 2, while at the outlet, environment pressure and temperature at 25 °C were assumed.

Table 10 Properties of water and ethanol for CFD calculation from the engineering database (Solidworks).



3.1 Mixing index evaluation

Evaluation of Mixing index (MI) is established based on the deviation of the mass fraction in a cross-section. This method involves dividing the cross-section into several cells, which in this case are the grid elements. The mass fraction is then calculated for each cell. Ideal mixing is characterized by a uniform distribution of particles from the two branches throughout the cross-section, resulting in equal proportions of particles with indices 0 and 1. Optimal mixing should therefore result in an even partition of particles with indices 0 and 1. The calculation of the MI in each cross-section of the micromixer is done as follows:

$$MI = 1 - \frac{\sigma}{\sigma_0} \quad (38)$$

where σ is the standard deviation of the mass fraction in a cross-section, which is determined using the integrated function of the CFD code:

$$\sigma^2 = \frac{1}{N} \sum_{i=1}^N (C_i - \bar{C})^2 \quad (39)$$

The standard deviation is at its maximum for unmixed fluids and at its minimum for perfectly mixed fluids. N represents the total number of cells in a cross-section, C_i is the mass fraction and \bar{C} is the average mass fraction. Mixing is considered to have occurred when the mass fractions of the two fluids are equal, meaning they both reach the value of 0.5. The maximum standard deviation σ_0 over the data range is calculated as:

$$\sigma_0^2 = \bar{C}(1 - \bar{C}) \quad (40)$$

A mixing index (MI) of 1 indicates perfect mixing ($\sigma = 0$), and MI of 0 indicates an unmixed state ($\sigma = \sigma_0$). A higher value of MI indicates a more homogeneous concentration and better mixing performance (74).

3.2 Reynolds number expression

The generalized Reynolds number expression for the vortex tube reactor was calculated using computational fluid dynamics (CFD) simulations, as follows:

$$Re = \frac{\rho v D}{\mu} \quad (41)$$

The following parameters were used in the calculation of the Reynolds number expression: Fluid density (ρ) and dynamic viscosity (μ) were taken as an input based on the fluid used in the vortex tube reactor, which was obtained from the engineering database (Solidworks2021) in Table 11 which provides the values for the fluid as a function of temperature. The velocity is characterized by the average fluid inlet velocity (v), which is calculated using the integrated function of the CFD code. The velocity was determined by measuring the fluid flow rate and dividing it by the cross-sectional area of the reactor, and the entire fluid flow was assumed to exit

through the fluid outlet of the vortex tube reactor. Diameter (D) of the reactor was taken as an input based on the overall body of the vortex tube reactor (75-77).

4. Mesh independency test

This sub-section presents a detailed methodology for the mesh sensitivity analysis conducted in the vortex tube reactor study. To evaluate the sensitivity of the simulation results, a comprehensive mesh sensitivity analysis was conducted for each mesh resolution. The analysis involved systematically varying seven levels of automated meshing while keeping other simulation parameters constant. There are two types of mesh. The tetrahedral shape is suitable for curved surfaces, and the hexahedral shape is appropriate for flat surfaces. The difference in mesh refinement is shown in Figure 23. By comparing the simulation results obtained from different mesh resolutions, the convergence and stability of the results were assessed. The analysis aimed to determine the optimal mesh size and resolution that would ensure accurate and reliable results in the numerical simulations.

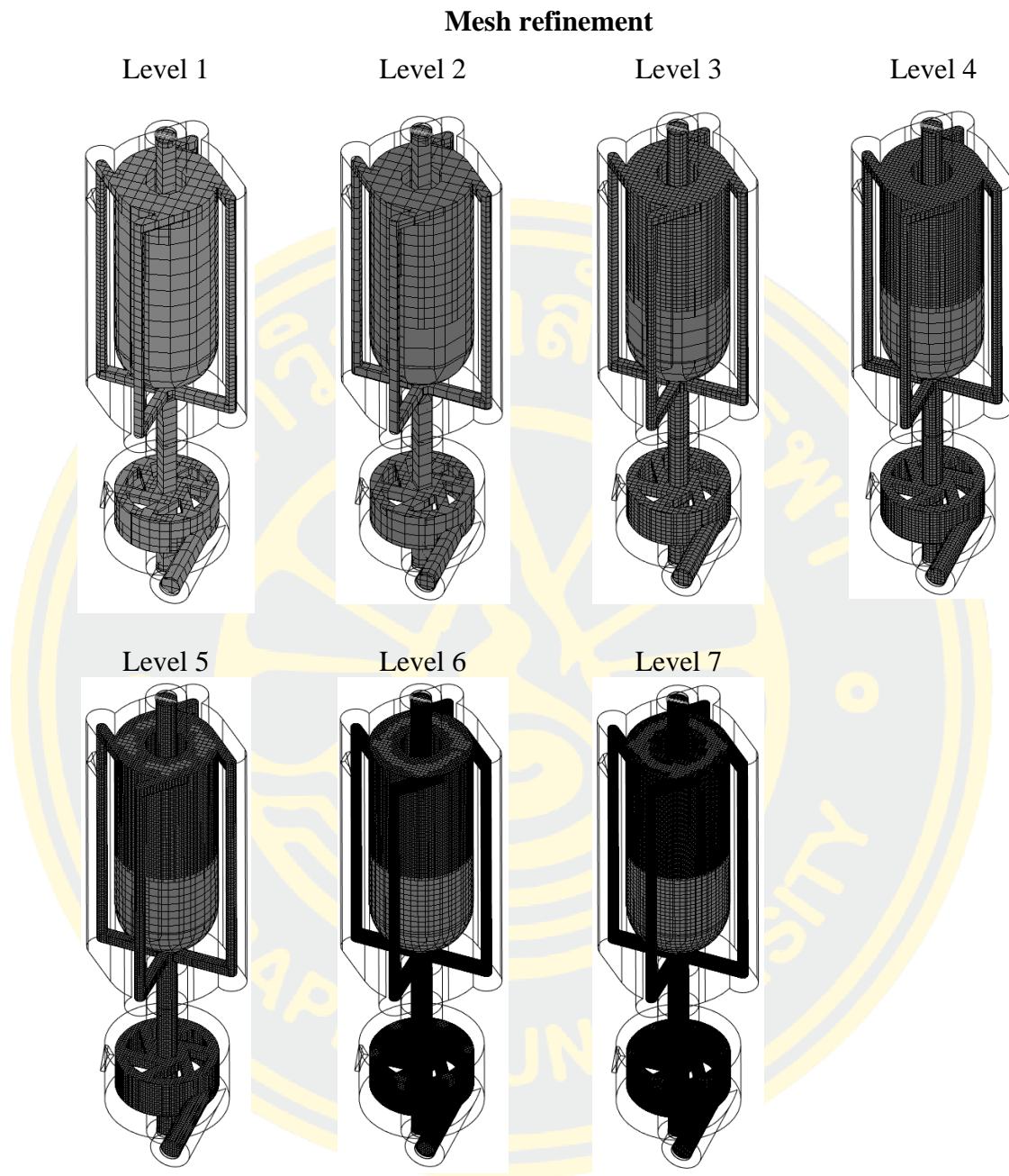


Figure 23 Difference mesh refinement of the automating generated mesh in 7 levels.

5. Optimization of geometrical vortex tube reactor model design

Once the simulation of each sample is completed, the Design-Expert 11 software was used to calculate the relationship patterns using partial least square models and 3D surface plots. Then, the optimized vortex tube reactor was calculated by setting the criteria shown in Table 11. Y_1 : the mixing index must be close to 1 (target to 1), which indicates complete mixing, and Y_2 : the Reynolds number must be maximized, which indicates that the flow characteristic is closely turbulent. The prediction of the optimized vortex tube reactor design parameters was optimized for optimal mixing efficiency.

Table 11 Constraint and criteria of the optimized vortex tube reactor model.

Factor (X) and Response (Y)		Constraint	Criteria
X_1	Reactor length	$10 < X_1 < 90$	In range
X_2	Internal tube to chamber wall width	$2 < X_2 < 10$	In range
X_3	Percentage of Internal tube length/Reactor length	$10 < X_3 < 90$	In range
X_4	Total flow rate	$10 < X_4 < 130$	In range
Y_1	Mixing index	$0.9474 < Y_1 < 1$	Target = 1
Y_2	Reynolds number	$239.45 < Y_2 < 3,132.25$	Maximize

6. Fabrication of 3D printed vortex tube reactor based FDM

The fabrication process of the 3D printed vortex tube reactor was carried out using fused deposition modeling (FDM) technology (UP Mini 2, Beijing Tiertime Technology Co., Ltd., China) with polypropylene (PP) filament. The design of the vortex tube reactor was created using computer-aided design (CAD) software. The STL file was then converted and sliced into G-code using the slicing software of UPstudio (Beijing Tiertime Technology Co., Ltd., China), and then loaded into the FDM printer by the printing conditions shown in Table 12.

Table 12 The FDM 3D-printing condition.

Printing condition	Parameter setting
Polymer	PP Filament
Nozzle Diameter	0.4 mm
Layer Height	0.2 mm
Print Speed	50 mm/s
Infill	20%
Print Temperature	210°C
Bed Temperature	50°C

After completing the printing process, the 3D printed vortex tube reactor was removed from the build platform and cleaned to remove any excess material. In the post-processing stage, dichloromethane flowed through the reactor for 5 minutes at a flow rate of 10 mL/min to dissolve any remaining filament and seal any potential leaks. This was followed by a 15-minute flow of ethanol at a flow rate of 10 mL/min, which was used to flush out the dichloromethane and ensured that the reactor was free of any remaining residue. The 3D printed vortex tube reactor was then assembled and tested to ensure its functionality.

7. Dispersion experiment

A dispersion experiment was conducted in the optimized reactor to observe the effect of fluid dynamics on the dispersion behavior of the tracer within the reactor. 0.5 mL of 1% (w/v) erythrosine solution, as a tracer, was injected into the reactor with a flow rate of 10–120 mL/min of DI water. Samples were collected at regular time intervals, and the absorbance was measured using a UV-VIS spectrophotometer (2J1-0004, Hitachi, Japan) at a wavelength of 530 nm. The absorbance measurements of tracer concentration ($C(t)$) at the time (t) were used to evaluate the residence time distribution function $E(t)$, the mean residence time (t_m), and the distribution variance (σ^2).

The residence time distribution function (RTD) or $E(t)$ function can be calculated from the sample data collected at various time intervals. The RTD is the fraction of total fluid in the reactor that is leaving at a specific time.

$$E(t) = \frac{C(t)}{\int_0^{\infty} C(t)dt} \quad (42)$$

The mean residence time (t_m) can then be calculated from the RTD by finding the first moment of the RTD:

$$t_m = \frac{\int_0^{\infty} t \cdot C(t)dt}{\int_0^{\infty} C(t)dt} \quad (43)$$

The distribution variance can also be calculated from the RTD as the second moment of the RTD:

$$\sigma^2 = \frac{\int_0^{\infty} (t - t_m)^2 \cdot C(t)dt}{\int_0^{\infty} C(t)dt} = \int_0^{\infty} t^2 E(t)dt - t_m^2 \quad (44)$$

To facilitate the comparison of results obtained from different flow rates of the vortex tube reactor configurations, it is necessary to use dimensionless units. The dimensionless concentration (C_{θ}) can be calculated by dividing the tracer concentration at time ($C(t)$) by the initial tracer concentration (C_0):

$$C_{\theta} = \frac{C(t)}{C_0} \quad (45)$$

Similarly, the dimensionless time (θ) can be calculated by dividing time (t) by the mean residence time (t_m):

$$\theta = \frac{t}{t_m} \quad (46)$$

Finally, the dimensionless $E(\theta)$ can be obtained by using C_θ and θ :

$$E(\theta) = \frac{C(\theta)}{\int_0^\infty C(\theta)d\theta} \quad (47)$$

8. Synthesis and evaluation of PGA nanoparticles for investigation of flow chemistry parameters in a vortex tube reactor

The investigation of flow chemistry parameters was conducted by PGA nanoparticles synthesis with a vortex tube reactor. Choosing PGA aimed to validate the experimental process, ensuring the vortex tube reactor's effective synthesis of nanoparticles. This approach allowed for an initial confirmation of the reactor's capability, with flexibility for adjustments to enhance nanoparticle properties. In this study, the flow system was operated by combining an aqueous solution of 0.5% w/v of PVA in DI water with an organic phase, which contained 0.5% w/v PGA in acetone. The impact of different system parameters on the size and PDI of the final formulation was studied by adjusting the total flow rate and aqueous-to-organic volumetric ratio of the incoming streams from 68.92 to 140 mL/min and from a ratio of 3:1 to 9:1 (aqueous-to-organic volumetric ratio), respectively. Total flow rate represents the combined flow rate of the organic and aqueous phases that are pumped through the two inlets, while aqueous-to-organic volumetric ratio refers to the volume ratio of the aqueous and organic phases, which the experimental setting-up shows in Figure 24.

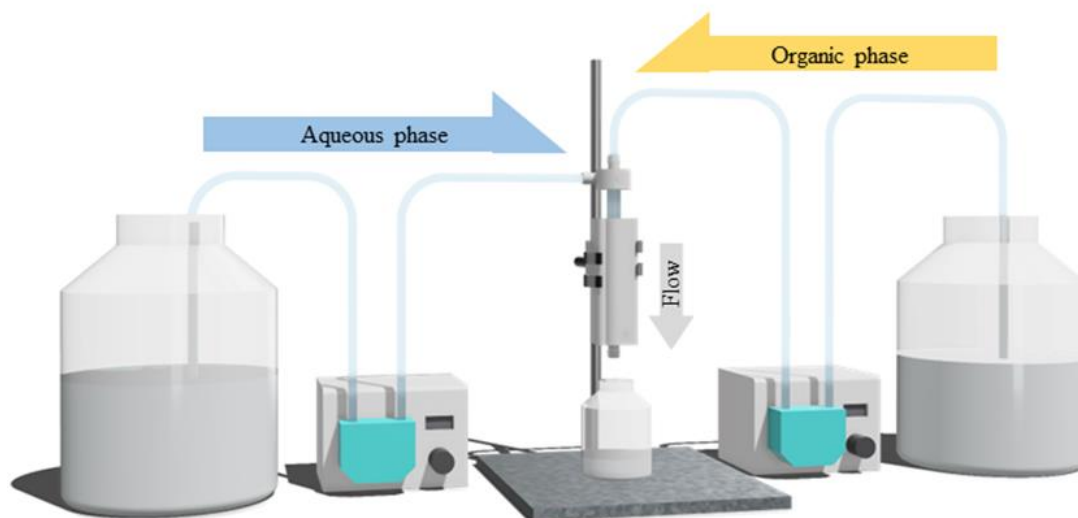


Figure 24 Schematic representation of the experimental setting-up of the vortex tube reactor in synthesis of nanoparticles.

9. Formulating lipid-based nanoparticles through a vortex tube reactor using the Block Behnken design

The lipid-based nanoparticles were produced using a vortex tube reactor by combining an aqueous solution of 2 mg/mL of BSA, as the biological model drug, in DI water and an organic phase of ethanol containing DPPC and cholesterol lipids in a weight ratio of 70:30, at a total concentration of 10 mg/mL, which the experimental setting-up shows in Figure 24. The primary objective was to enhance the efficiency of lipid-based nanoparticles, transforming them into effective carriers for delivering bioproducts. This aimed to investigate potential applications in targeted drug delivery and other biomedical fields, along with assessing the performance of a vortex tube reactor in the synthesis of lipid-based nanoparticles.

The influence of various system parameters on the final formulation was investigated by an experimental design called Block Behnken Design, as shown in Table 13. The factors of interest in this study were X_1 : total flow rate of the incoming streams from 68.92 to 140 mL/min, X_2 : aqueous-to-organic volumetric ratio of the incoming streams from a ratio of 3:1 to 9:1 (aqueous-to-organic volumetric ratio), and X_3 : the number of reactor units ranging from 1-5 units. Total flow rate represents the combined flow rate of the organic and aqueous phases that are pumped through the

two inlets, while aqueous-to-organic volumetric ratio refers to the volume ratio of the aqueous and organic phases. These factors were related to the responses of the study, which included Y_1 : z-average, Y_2 : polydispersity index, Y_3 : zeta-potential, Y_4 : %entrapment efficiency, Y_5 : %drug loading capacity, and Y_6 : productivity. The collected samples were transferred to centrifugal ultrafiltration with MWCO of 30 kDa (Amicon Ultra-15 filter, Merck, Germany) and centrifuged at 8,000 rpm and 4°C for 30 minutes. The retentate containing loaded BSA was redispersed to 1.5 mL with DI water and kept at 2°C - 8°C in refrigerator.

Table 13 The interested factors on formulation of lipid-based nanoparticles using a vortex tube reactor.

Factor(X)	Unit	DoE Code		
		-1	0	1
X_1 : Total flow rate	mL/min	10	55	100
X_2 : Aqueous-to-organic volumetric ratio	-	1	5.5	10
X_3 : Number of reactor units	unit	1	3	5

10. Lyophilization of lipid-based nanoparticles

To obtain powdered particles from BSA-loaded LNPs, the BSA-loaded LNPs were first prepared, and then the samples were filled into cryovials, each containing up to 1 mL of the sample. Subsequently, these cryovials were subjected to an initial deep-freezing step at -80°C for a duration of 2-3 hours. After this initial freezing step, the cryovials were transferred to the vacuum chamber of a lyophilizer (Christ Gamma 2-16 LSCplus, Martin Christ, Germany.) Within this vacuum chamber, the samples underwent the lyophilization process, during which all the water within the samples completely sublimated.

11. The physical characteristics of lipid-based nanoparticles

The particle size, polydispersity index and zeta-potential were evaluated using a Zetasizer (MAL1070387, Malvern, UK). To perform the measurements, the

lipid-based nanoparticles were diluted to a concentration of 10% v/v using deionized water and agitated for 3 minutes before analysis. The average values and standard error were calculated based on measurements from three batches of samples.

12. Entrapment efficiency and loading capacity evaluation

To measure the BSA loading in LNPs, this method was modified from Roshan Goswami et.al., 2021 (78), and integrated it with Bradford assay (79). Specifically, 100 μL of the retentate containing loaded BSA was taken in the centrifugal ultrafiltration. This initial sample was diluted by adding 100 μL of 0.1% Triton X-100 in DI water. Triton X-100 disrupts the integrity of the lipid nanoparticles (LNPs), leading to the release of the BSA encapsulated within the LNPs. Subsequently, this diluted sample was further diluted by 60 times the original volume of DI water. Following by Bradford Assay to quantify the BSA content, 200 μL of Bradford reagent was added to 200 μL of the diluted sample. The mixture was then incubated for 10 minutes at room temperature. The Bradford assay is based on the formation of a, with absorbance measured at 595 nm. The concentration of BSA in the LNPs was determined by comparing the absorbance values to a standard curve constructed using known BSA concentrations. The encapsulation efficiency (EE%) was calculated as the percentage of BSA incorporated compared to the initial BSA concentration available using the following equation:

$$EE\% = \frac{\text{Mass of loaded BSA}}{\text{Total BSA used}} \times 100\% \quad (48)$$

Loading capacity (LC%) was calculated as the percentage of the mass of BSA-loaded divided by the total mass of the particle component (lyophilized LNPs) using the following equation:

$$LC\% = \frac{\text{Mass of loaded BSA}}{\text{Total mass of the particle components}} \times 100\% \quad (49)$$

13. Productivity evaluation

To calculate the productivity after lyophilization of LNPs synthesis, the weight of the final lyophilized product obtained after the process. The productivity can be calculated using the following equation:

$$\text{Productivity} = \frac{\text{Total mass of lyophilized product}}{\text{Total time for the synthesis}} \quad (50)$$

14. Morphology evaluation

The surface morphology of the lipid-based nanoparticles was meticulously examined through a comprehensive imaging approach involving Transmission Electron Microscopy (TEM) (TECNAI 20, Philips, Amsterdam, Netherlands) and Scanning Electron Microscopy (SEM) (LEO 1450 VP, Carl Zeiss, Germany).

For sample preparation in TEM imaging, a small aliquot of the nanoparticle suspension was meticulously fixed onto a formvar-coated copper grid. Following this, the samples underwent a thorough drying process to ensure optimal imaging conditions. TEM imaging was performed at an accelerating voltage of 100 kV, and micrographs were captured under various magnifications to obtain detailed insights into the nanoparticle structure.

Additionally, SEM imaging was conducted. The SEM analysis provided complementary insights into the three-dimensional surface structure of the nanoparticles. To prepare samples for SEM, a small quantity of the nanoparticle suspension was affixed to an SEM stub using double-sided adhesive tape. A gold coating was then applied using a sputter coater under vacuum conditions to enhance conductivity and facilitate improved imaging quality. SEM imaging was performed at an accelerating voltage of 15 kV, and the samples were observed under various working distances to capture a range of magnifications.

15. Optimization condition for lipid-based nanoparticles formulation using a vortex tube reactor

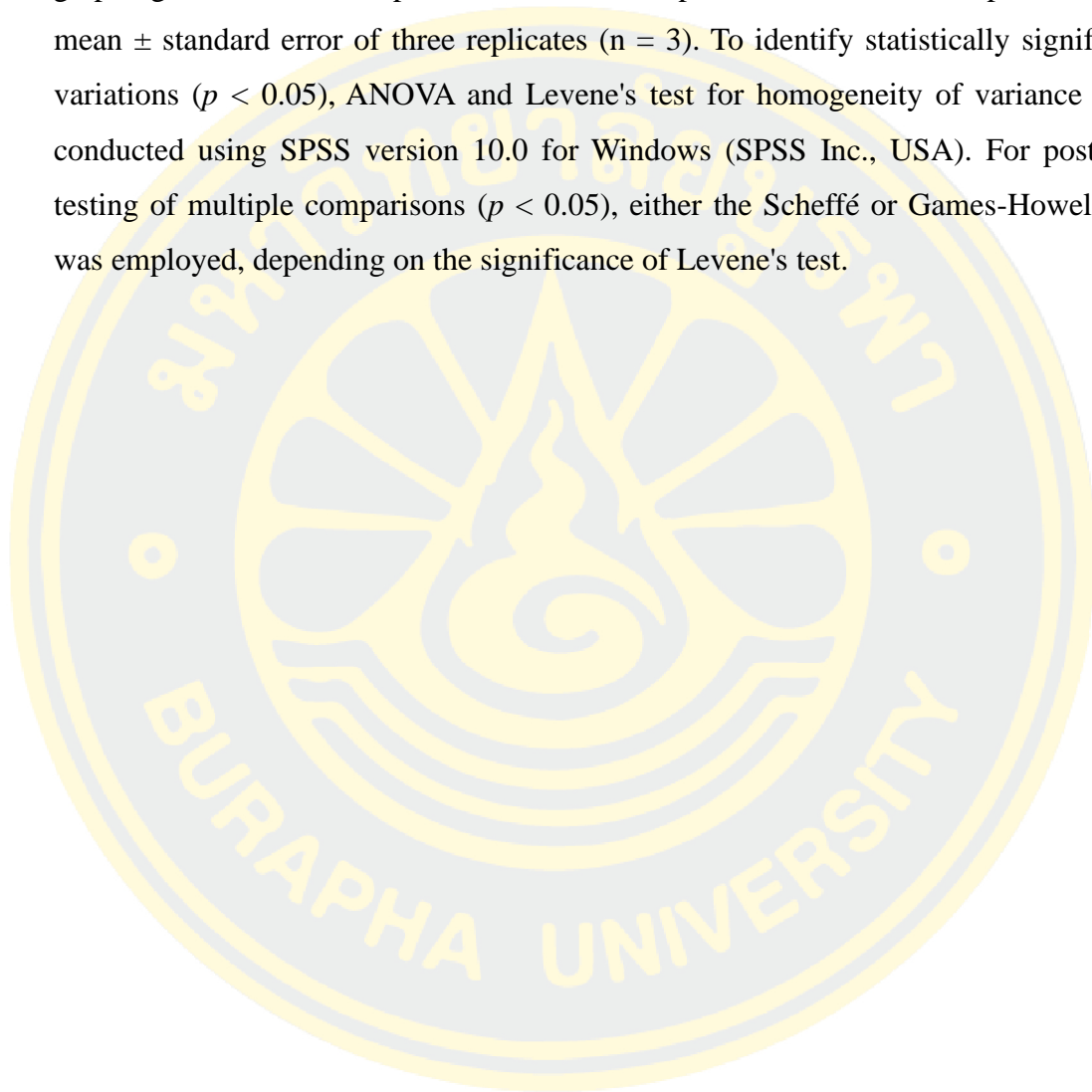
In order to optimize the formulation condition of lipid-based nanoparticle using the vortex tube reactor, Design Expert 11 software is employed. This software utilizes partial least square models and 3D surface plots to identify relationship patterns based on simulation results for each sample. Table 14 outlines the optimization criteria, encompassing in ranges of X_1 : total flow rate ratio, X_2 : aqueous-to-organic volumetric ratio, and X_3 : the number of reactor units. The objective is to minimize Y_1 (z-average), Y_2 (PDI), and Y_3 (zeta potential). Additionally, the goal is to maximize Y_4 (% entrapment efficiency), Y_5 (% loading capacity), and Y_6 (productivity) in order to predict the optimal conditions that will yield both high productivity and desirable physical properties for the lipid-based nanoparticles.

Table 14 Constraint and criteria of the optimized condition of lipid-based nanoparticle synthesis.

Factor (X) and Response (Y)		Constraint	Criteria
X_1	Total flow rate	$10 < X_1 < 100$	In range
X_2	Aqueous-to-organic volumetric ratio	$1 < X_2 < 10$	In range
X_3	Number of reactor units	$1 < X_3 < 5$	In range
Y_1	Z-average	$153.10 < Y_1 < 323.10$	Minimize
Y_2	PDI	$0.125 < Y_2 < 0.515$	Minimize
Y_3	Zeta potential	$-16.70 < Y_3 < -8.25$	Minimize
Y_4	% Entrapment efficiency	$31.11 < Y_4 < 118.66$	Maximize
Y_5	% Drug loading	$20.48 < Y_5 < 50.69$	Maximize
Y_6	Productivity	$21.27 < Y_6 < 391.50$	Maximize

16. Statistical analysis

The correlations of CFD parameters and experimental parameter were determined using Design Expert 11 (Stat-Ease, Inc., USA) for statistical analysis and graphing of the model response surface. The experimental data were reported as the mean \pm standard error of three replicates ($n = 3$). To identify statistically significant variations ($p < 0.05$), ANOVA and Levene's test for homogeneity of variance were conducted using SPSS version 10.0 for Windows (SPSS Inc., USA). For post hoc testing of multiple comparisons ($p < 0.05$), either the Scheffé or Games-Howell test was employed, depending on the significance of Levene's test.



CHAPTER 4

RESULTS

1. CFD mesh sensitivity

An unstructured and uniform mesh with tetrahedral cells was employed to assess the sensitivity of the outcomes to mesh refinement and to determine the optimal cell size in the vortex tube reactor while ensuring accuracy and reliable results in the numerical simulations. The mesh convergence was evaluated by testing seven levels of automated meshing, as shown in Figure 25a, and the normalized value determined the proportion of each level value divided by the 7th level value. The results show that the meshing of six-levels, as illustrated by the center point models shown in Figure 25b, is initially convergence indicated adequate for obtaining precise outcomes, with a relative error with seven-level less than 0.2689% for the mass fraction of water and 1.4667% for the Reynolds number, as shown in Table 15. Other models were initially convergent at the same six-level as described in Appendix. Therefore, this meshing was chosen as the optimal grid for the study. Based on the findings, the 6th level meshing offers a balance between accuracy and computational efficiency.

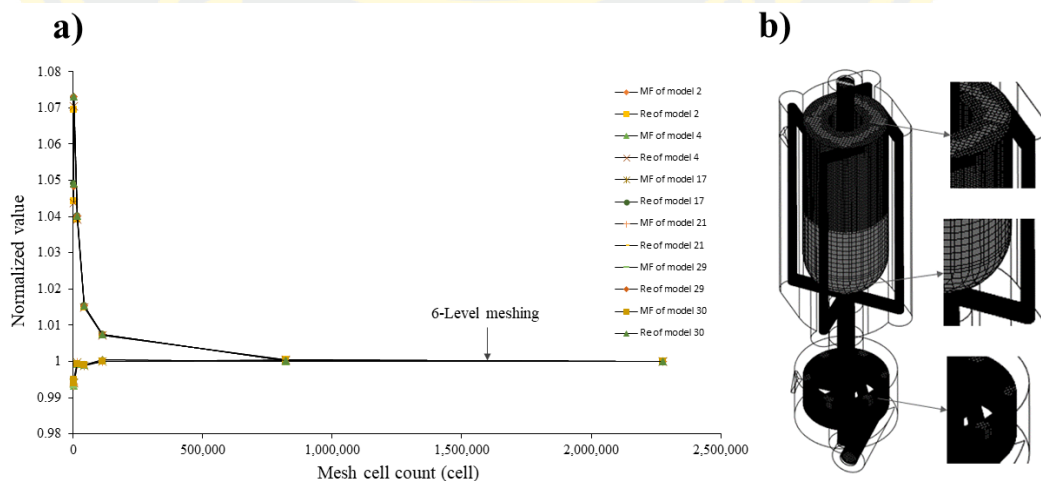


Figure 25 (a) Mesh independence test using the vortex tube reactor and (b) the automating generated mesh for all studied the vortex tube reactor model.

Table 15 Relative error with the highest level automating generated grids (7th level).

Run	Mech no. of 6 th level meshing (cells)	Iteration	%Relative error with 7 th level	
			Mass fraction of water	Reynolds number
1	817,569	521	0.0537	0.0785
2	821,352	508	0.0000	0.0417
3	658,343	447	0.0179	0.0749
4	821,325	508	0.0000	0.0417
5	133,316	437	0.0538	0.0732
6	849,119	383	0.1439	0.0677
7	1,031,558	488	0.1436	0.0333
8	1,428,243	526	0.0717	0.0680
9	1,010,688	419	0.1799	0.0942
10	821,352	534	0.0896	0.2214
11	639,576	461	0.2689	0.4146
12	658,350	531	0.0358	0.0438
13	849,077	434	0.0716	0.5331
14	1,032,001	459	0.1076	0.0679
15	821,352	401	0.0000	0.0627
16	1,010,660	449	0.0539	0.3500
17	821,352	506	0.0179	0.0298
18	195,603	275	0.1073	1.4667
19	941,032	584	0.0000	0.0627
20	673,532	437	0.0179	0.0356
21	821,366	506	0.0179	0.0268
22	817,667	636	0.0000	0.0584
23	733,085	518	0.0358	0.3908
24	276,519	307	0.0896	0.1132
25	639,597	381	0.0179	0.0313
26	1,427,656	580	0.0538	0.0313
27	1,013,285	557	0.0179	0.0657
28	630,716	624	0.0179	0.0358
29	821,352	506	0.0358	0.0298
30	821,086	506	0.0179	0.0268

2. Experimental design of vortex tube reactor

The results of central-composite design experiments involving four factors in Table 16 were assessed, and the correlations between independent and dependent variables were analyzed using partial least square regression. The relationship findings between the independent factors (X) and the responses (Y) are presented in Table 17. The PLS model based on the coded factors of MI and Reynold number was found to be highly significant with a p-value of 0.0003 and less than 0.0001, respectively. This indicates that the model can effectively explain the relationship between the independent variables and the dependent variable. Nevertheless, a noteworthy observation emerged when examining center points with minimal

variation in mixing index and Reynold number within CFD results. Their proximity was so pronounced that overlap occurred. Despite the proficient fit of the predicted CCD model to the designated points, indicating a substantial model fit, a disparity surfaced. The discrepancies between the actual data points far surpassed those between the center points, leading to a notable lack of fit statistic. Intriguingly, the center points demonstrated a superior fit compared to the model points, revealing a nuanced aspect of the analysis of CFD results.

Table 16 Experimental runs and response results in the central-composite design.

Model	X ₁ : Reactor length (mm)	X ₂ : Internal tube to chamber wall width (mm)	X ₃ : Percentage of Internal tube length/Reactor length (%)	X ₄ : Total flow rate (mL/min)	Y ₁ : Mixing index	Y ₂ : Reynolds number
1	70	8	70	40	0.9956	1,070.28
2	50	6	50	70	0.9978	1,677.65
3	70	8	30	40	0.9958	1,148.58
4	50	6	50	70	0.9979	1,677.65
5	30	8	70	40	0.9928	1,148.88
6	30	4	30	40	0.9886	767.20
7	70	4	30	100	0.9989	1,924.36
8	70	4	70	40	0.9863	765.72
9	30	4	70	40	0.9899	765.36
10	50	6	50	130	0.9997	3,132.25
11	30	8	30	100	0.9995	2,911.32
12	70	8	30	100	0.9997	2,879.04
13	30	4	30	100	0.9998	1,940.40
14	70	4	30	40	0.9943	766.20
15	50	6	50	10	0.9474	239.45
16	30	4	70	100	0.9973	1,936.08
17	50	6	50	70	0.9988	1,679.05
18	10	6	50	70	0.9974	1,753.35
19	90	6	50	70	0.9963	1,676.70
20	50	6	10	70	0.9989	1,685.70
21	50	6	50	70	0.9983	1,679.00
22	70	8	70	100	0.9997	2,876.46
23	30	8	70	100	0.9998	2,905.50
24	50	2	50	70	0.9668	1,007.88

Model	X ₁ : Reactor length (mm)	X ₂ : Internal tube to chamber wall width (mm)	X ₃ : Percentage of Internal tube length/Reactor length (%)	X ₄ : Total flow rate (mL/min)	Y ₁ : Mixing index	Y ₂ : Reynolds number
25	30	8	30	40	0.9952	1,150.86
26	70	4	70	100	0.9982	1,916.36
27	50	6	90	70	0.9957	1,676.45
28	50	10	50	70	0.9981	2,349.69
29	50	6	50	70	0.9983	1,679.05
30	50	6	50	70	0.9983	1,679.00

Table 17 Partial Least Square Regression Model (PLS Model) in terms of coded factors of Y₁ and Y₂.

PLS models	p-value	F-value	R ²	Adjusted R ²
$Y_1 = 0.0082X_1^2X_2^2 - 0.0008X_1X_2X_3X_4 - 0.0063X_1^2X_2 - 0.0097X_1^2X_4 + 0.0006X_1X_2^2 + 0.0006X_1X_2X_3 - 0.0001X_1X_2X_4 + 0.0005X_1X_3X_4 - 0.0003X_1^2 - 0.004X_2^2 - 0.0002X_3^2 - 0.0062X_4^2 + 0.0001X_1X_2 - 0.0003X_1X_3 - 0.0003X_1X_4 + 0.0005X_2X_3 - 0.001X_2X_4 + 0.0004X_3X_4 - 0.0003X_1 + 0.0078X_2 - 0.0008X_3 + 0.0131X_4 + 0.9983$	0.0003*	1,186.23	0.9998	0.9990
Lack of fit	0.0489*	5.86		
$Y_2 = 150.063X_2X_4 - 13.8292X_1 + 333.036X_2 + 728.835X_4 + 1682.18$	<0.0001*	13,561.78	0.9995	0.9995
Lack of fit	<0.0001*	720.05		

* indicating statistical significance (p-value < 0.05)

2.1 Mixing performances of vortex tube reactor (Y₁)

The mixing index refers to a quantitative measure of how well their substances are mixed homogeneously. It is often used to evaluate the efficiency of mixing performance in the vortex tube reactor model. The results of the PLS model for predicting the mixing index in this system provide valuable insights into the

relative importance of the different factors that affect mixing, while the RS plot is shown in Figure 26. The coefficients of the PLS equation reveal the relative importance of each variable in predicting the mixing index. The highest positive coefficients were found for $X_1^2 X_2^2$ ($p < 0.0001$), X_2 ($p < 0.0001$), and X_4 ($p < 0.0001$), indicating that these variables have the greatest positive influence on the mixing index. Conversely, the highest negative coefficients were found for $X_1^2 X_2$ ($p < 0.0001$), $X_1^2 X_4$ ($p < 0.0001$), X_2^2 ($p < 0.0001$) and X_4^2 ($p < 0.0001$), indicating that these variables have a negative impact on the mixing index. Other coefficients were found to have smaller effects on the mixing index. These factors may be less critical for predicting mixing performance, and their influence may be overshadowed by the larger effects of other factors. In the PLS model for Y_1 , the factors of X_1 , X_2 and X_4 have positive and negative coefficients in the difference term, which suggests that increasing these factors can lead to better mixing performance, but extreme values of these factors can reduce the mixing index. This finding is supported by previous studies on the design of the passive mixer with threaded inserts for enhancing mixing performance via flow chemistry. The results showed that the design of the flow direction by threaded insert for vortex streamlines and increasing Reynolds number via increasing flow rate had the greatest impact on mixing performance (80).

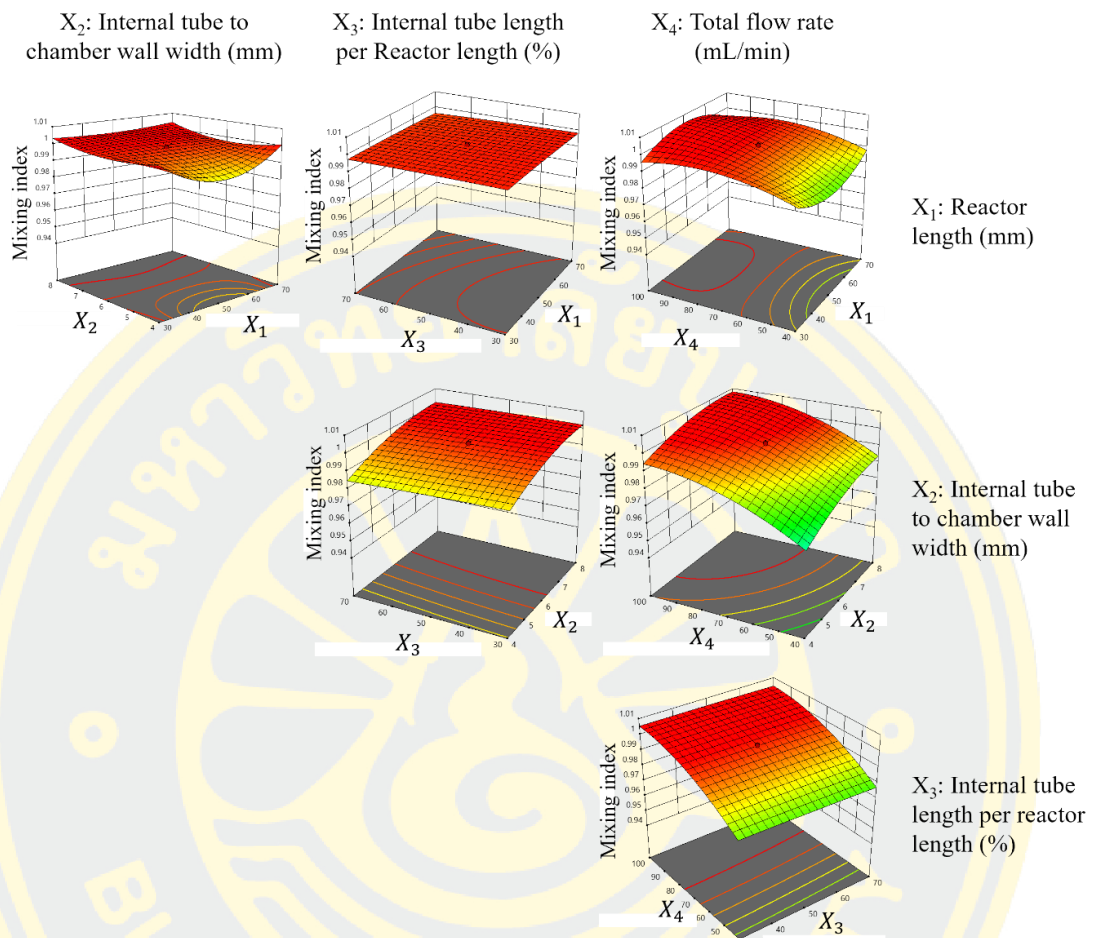


Figure 26 Response surface plot of the mixing index.

The findings of this study are consistent with Reynolds' transport theorem, which suggests that increasing the diameter of the reactor results in a more turbulent flow of the fluid (7, 8). This increased turbulence can lead to better mixing efficiency as the fluid experiences greater mixing and agitation. The study also found that increasing the flow rate resulted in the formation of vortex streamlines in the reactor, which further enhanced the mixing efficiency. Overall, these findings can be useful for the design and optimization of similar systems, as they provide insights into the factors that can have the greatest impact on mixing performance. The high significance and accuracy of the PLS model also suggest that it can be a valuable tool for predicting mixing performance in this system.

2.2 Flow structures of vortex tube reactor (Y₂)

Reynolds number analysis is used to determine the flow regime of a fluid and predict the flow behavior within the vortex tube reactor model based on its velocity, density, viscosity, and characteristic length. The Reynolds number (Re) is a dimensionless quantity that helps classify the type of flow, whether it is laminar, transition, or turbulent. In this study, the coefficients of the PLS equation reveal the relative importance of each variable in predicting the Reynolds number, while the RS plot of major factors is shown in Figure 27. The highest positive coefficient was found for X_2X_4 ($p < 0.0001$), X_2 ($p < 0.0001$), and X_4 ($p < 0.0001$) indicating the greatest positive influence on the Reynolds number. On the other hand, the coefficient for X_1 ($p = 0.0005^*$) was found to have a negative impact on the Reynolds number. This may suggest that increasing reactor diameter, increasing flow rate, and decreasing reactor length could result in higher Reynolds numbers while relating to the Reynolds transport theorem.

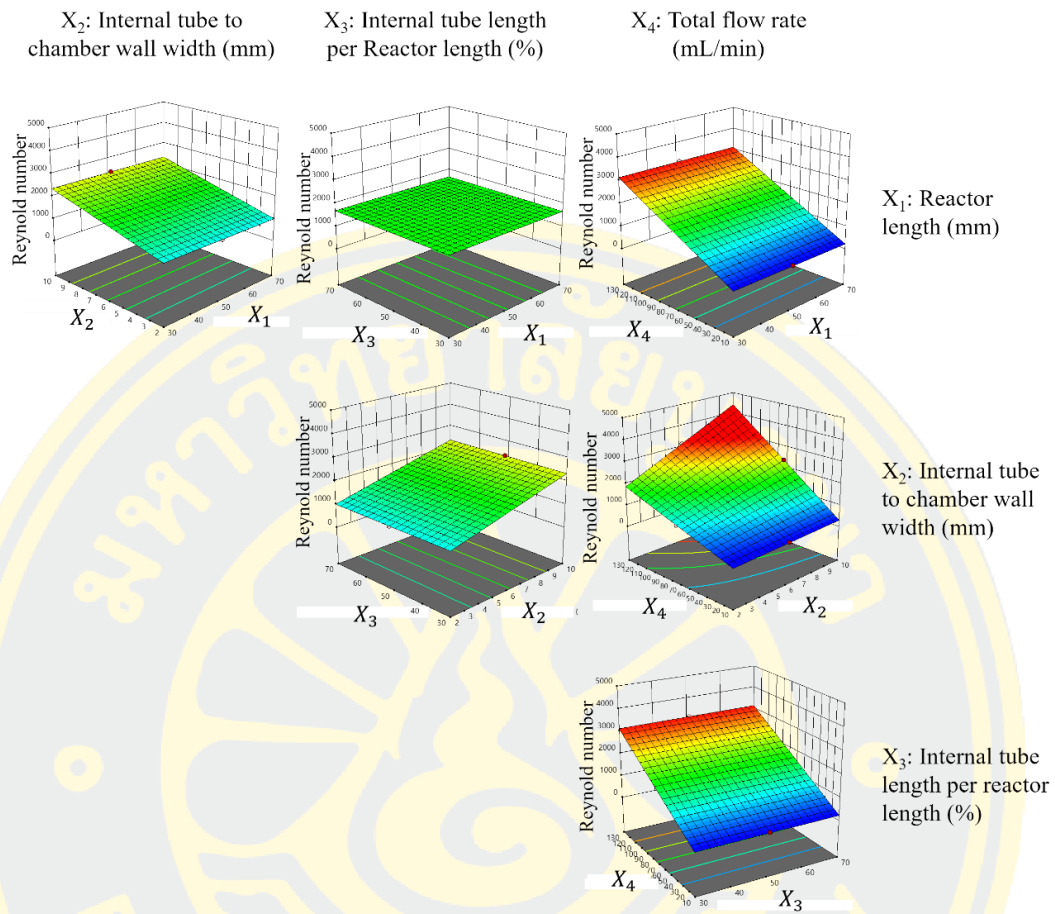


Figure 27 Response surface plot of the Reynolds number.

This study found a positive correlation between the increase in Reynolds number and improved mixing performance in the vortex tube reactor. However, increasing the reactor length can reduce the Reynolds number. This is because a longer reactor allows for more time for the fluid to develop a more steady and consistent flow, which can reduce turbulence and fluctuations in the fluid flow (81, 82).

Overall, these findings can be useful for the design and optimization of similar systems, as they provide insights into the factors that can have the greatest impact on the Reynolds number. The high significance and accuracy of the PLS model also suggest that it can be a valuable tool for predicting Reynolds numbers in this system.

3. Optimized vortex tube reactor

Once the experimental design was completed, partial least squares regression models and response surfaces were generated, and the constraints for all factors determined the desirability of all responses, as presented in Table 11. The optimization of the vortex tube reactor was performed, and the prediction values of the factors X_1 , X_2 , X_3 , and X_4 were obtained as 79.81 mm, 8.95 mm, 86.74 mm, and 104.46 mL/min, respectively. The vortex tube reactor was prepared and CFD analyzed according to the optimized conditions. Table 18 shows the prediction ability percentages obtained by comparing the predicted responses from the partial least squares regression models with the actual test values. The actual values were very close to the predicted values. For the response variables, the prediction ability of Y_1 and Y_2 were found to be 99.95% and 100.15%, respectively, which provided a desirability value of 1. The high percentage of prediction ability for both the factors and the response variables suggests that the optimization process was successful in predicting the optimal values for the factors and achieving the desired responses. These results indicate that the optimized conditions of the vortex tube reactor can lead to improved mixing performance and Reynolds number.

Table 18 Comparison between the predicted values form PLS models and the actual values of optimized vortex tube reactor model.

Mech no. (cells)	Iteration	Factor (X) and response (Y)	Unit	Calculated independent factor (X) and prediction values (Y)	Actual values	Percentage of prediction ability (%)	
880082	743	X_1 : Reactor length	mm	79.81	-	-	
		X_2 : Internal tube to chamber wall width	mm	8.95	-	-	
		X_3 : Internal tube length per reactor length	%	86.74	-	-	
		X_4 : Total flow rate	mL/min	104.46	-	-	
			Y_1 : Mixing index	-	1.0000	0.9995	99.95
			Y_2 : Reynold number	-	3244.46	3240.55	99.88

3.1 Mixing performance evaluation

The analysis of the mixing performance of the optimized vortex tube reactor was performed by CFD. The result showed that the mixing index was at 0.99948, indicating a homogeneous concentration and great mixing performance (MI approaches 1 and σ approaches 0 indicate perfect mixing) (74). The mass fraction cut plot of the vortex tube reactor (Figure 28a) shows that the fins at the mixer helped to accelerate the mixing process, and when the fluid flowed into the by-pass channels, mixing occurred almost completely before returning to the vortex chamber and exiting through the outlet, which shows the color change of the mass fraction of water in the optimized vortex tube reactor from red (high mass fraction of water) and blue (low mass fraction of water) to green (steady of mass fraction of water) in Figure 28a.

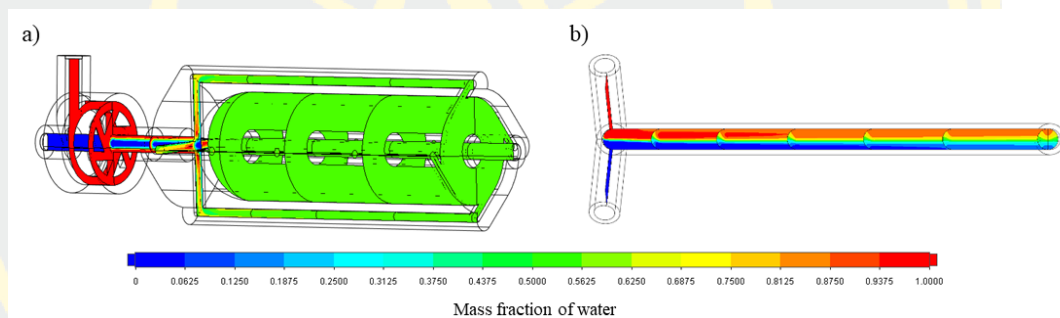


Figure 28 The mass fraction cut plot of (a) the vortex tube reactor and (b) the tubular reactor with a 4 mm diameter.

The measurement of mass fraction evolutions along the midline at the exit of the vortex tube reactor (Figure 29) revealed that these profiles were almost similar along the Y-direction of the graph, with a standard deviation value of only 0.00026, confirming the homogeneity of the mixing.

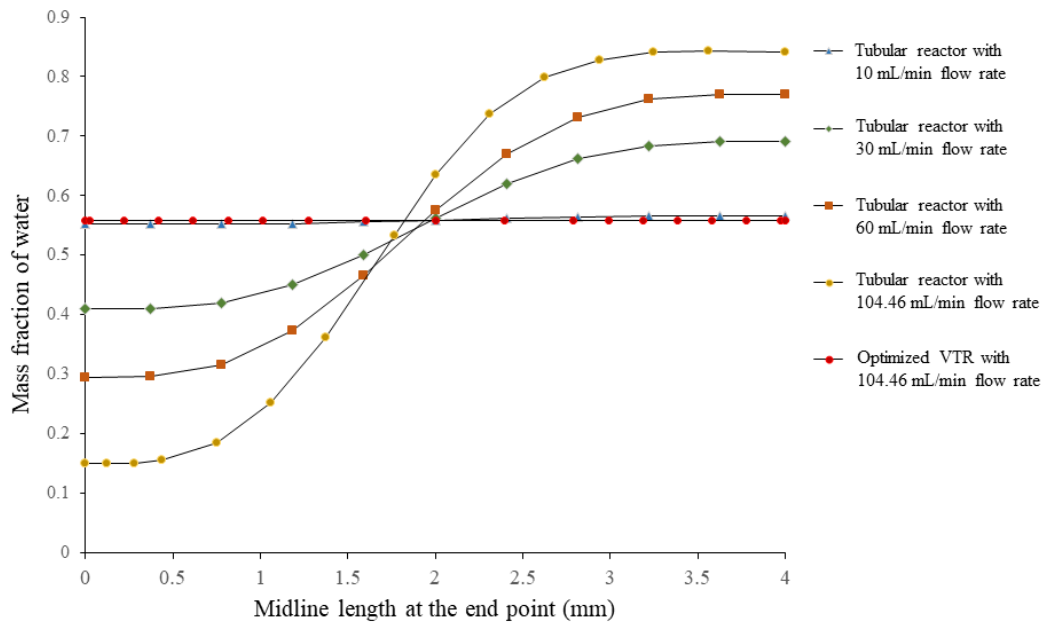


Figure 29 Mass fraction evolutions along the midline at the exit of the optimized vortex tube reactor model and the tubular reactor with different flow rate.

3.2 Reynolds number evaluation

The purpose of conducting a Reynolds number analysis is to identify the flow regime of a fluid and make predictions about the flow behavior within the optimized vortex tube reactor. The analysis of the Reynolds number revealed that the value was 3,240.55, indicating that the flow characteristics of the optimized vortex tube reactor were in a transitional state ($2,300 < Re < 4,000$) (83). This result is consistent with the vorticity streamlines cut plot shown in Figure 30a, where the streamlines inside the vortex tube reactor have a swirling and eddying pattern as well as some laminar pattern. This observation further confirms the transitional flow regime, which is characterized by the coexistence of both laminar and turbulent flow patterns. This finding is supported by previous studies on the transitional flow regime in various types of reactors. The transitional flow regime is known to be associated with enhanced mixing and improved mass transfer due to the coexistence of both laminar and turbulent flow patterns. Therefore, the transitional flow regime in the

optimized vortex tube reactor is expected to contribute to the improved mixing performance observed in this study (75).

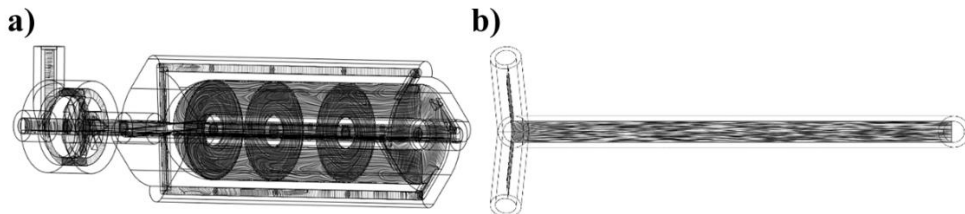


Figure 30 The vorticity streamline cut plot of (a) the vortex tube reactor and (b) the tubular reactor with a 4 mm diameter.

3.3 Relationship of mixing index in difference flow rate

The mixing index (MI) at different flow rates is presented in Figure 31, offering a glimpse into the intricate fluid dynamics within the vortex tube reactor. The increase in flow rate leads to an increase in Reynolds number, indicating a transition from laminar to turbulent flow. However, the mixing index initially remains high, indicating good mixing at low flow rates dominated by the diffusion term. In addition, the observation that the mixing index initially remains high at low flow rates is consistent with the theoretical expectation that diffusion dominates at low Reynolds numbers. In the context, the Navier-Stokes equation (equation 37) can be attributed to the balance between inertial forces and viscous forces. The dominance of the diffusion term at low Reynolds numbers aligns with the notion that viscous forces play a more pronounced role in the fluid motion, facilitating efficient mixing through molecular diffusion (84).

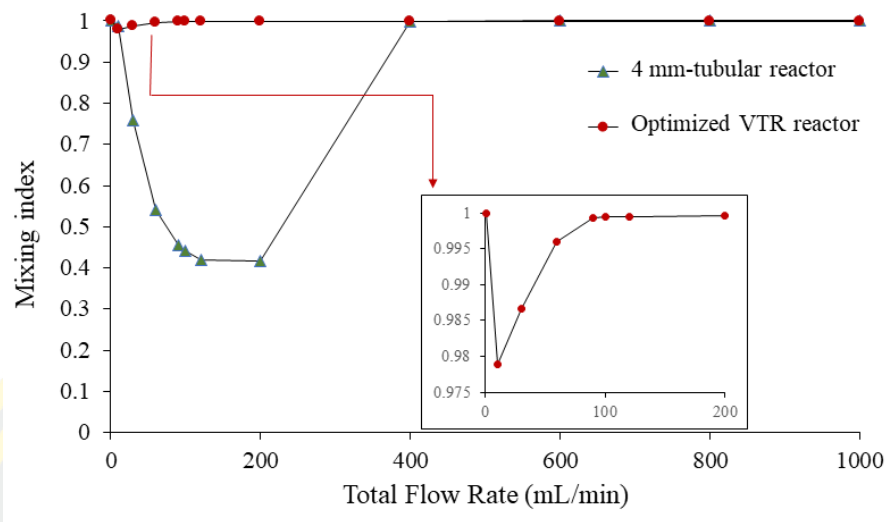


Figure 31 The mixing index at different flow rates of the vortex tube reactor and the tubular reactor with 4 mm diameter.

At a flow rate of 10 mL/min, corresponding to a Reynolds number of 310.21, the mixing index started to slightly decrease. This observation suggests that the onset of turbulence occurs and the increase in the convection term is not strong enough to fully homogenize the fluid. According to the Navier-Stokes equation (equation 37), the convection term, representing the transport of momentum by the bulk motion of the fluid, becomes more influential. The onset of turbulence at this point suggests that inertial forces are gaining prominence, but the increase in the convection term might not be sufficiently robust to fully homogenize the fluid. This phenomenon is in line with the complexities of turbulent flow, where incomplete mixing can be attributed to the persistence of stagnant regions and challenges in stirring the fluid within these regions, as documented in existing literature. Therefore, slightly increased turbulence may not be able to achieve complete mixing, leading to a reduction in the mixing index. This phenomenon has been previously reported in the literature, where it has been shown that the transition from laminar to turbulent flow can result in incomplete mixing due to the presence of stagnant regions and the difficulty of stirring the fluid in these regions (85).

For flow rates higher than 10 mL/min, the mixing index tends to increase and remains relatively stable at flow rates higher than 90 mL/min. The Navier-Stokes

equation (equation 37) provides context for this behavior, emphasizing the role of the convection term in enhancing mixing performance. At Reynolds numbers higher than 310.21, inertial forces dominate, and the convective transport of momentum becomes a major contributor to mixing. The vortex tube reactor proves highly effective in achieving homogeneity across this wide range of flow rates.

Comparison of vortex tube reactor and tubular reactor with a diameter of 4 mm connected to a Y-mixer. The simulation of the tubular reactor was under the same volume and boundary conditions as the optimized vortex tube reactor. The mixing index of the tubular reactor was found to be 0.392088, as the mass fraction cut plot shown in Figure 28b. The mass fraction evolutions along the midline at the exit of the typical tubular reactor showed an S-curve along the Y-direction of the graph (Figure 29), with a larger standard deviation value of 0.303952, indicating an unmixed state at the exit. The Reynolds number was measured to be 499.07, indicating laminar flow in the tubular reactor (Figure 30b) (83).

When the flow rate in a tubular reactor drops below 10 mL/min or exceeds 400 mL/min (Figure 31), the mixing index tends to increase. However, the variance in mass fraction along the midline at the exit of the reactor decreases (Figure 29). This trend continues until the flow rate drops below 10 mL/min or exceeds 400 mL/min, at which point the mixing index is no longer significantly different (p -value = 0.1733) from that of the vortex tube reactor at any flow rate. However, increasing the diameter or flow rate of the tubular reactor is not recommended as it would reduce the mixing performance and productivity. The reactor length should be sufficient to achieve complete mixing, or the flow rate should be slow enough to ensure good mixing without sacrificing productivity. While high flow rates may increase the mixing index, a high-pressure drop can negatively affect the system's efficiency by increasing energy consumption and reducing flow rates. A high-pressure drop requires more energy to maintain the desired flow rate, limiting the overall efficiency of the system.

Thus, the vortex tube reactor is a promising solution as it offers better mixing performance with a smaller reactor size and increased flow rate, which can enhance productivity. Including a wide range of flow rate adjustments while maintaining homogeneous mixing. This is consistent with previous studies that have

shown the effectiveness of vortex tube reactors in achieving higher mixing performance and productivity compared to traditional tubular reactors.

4. Fabrication of the vortex tube reactor based FDM

In this study, we successfully fabricated a vortex tube reactor using the fused deposition modeling (FDM) 3D printing technique. The reactor was designed with optimized parameters. The material used for printing was PP, which has good thermal and mechanical properties suitable for this application.

The fabrication process involved slicing the 3D model into layers and printing them using a desktop 3D printer. The printing parameters were optimized to obtain a smooth, defect-free surface, and the process occurred layer-by-layer. The 3D printed vortex tube reactor and assembly are shown in Figure 32.

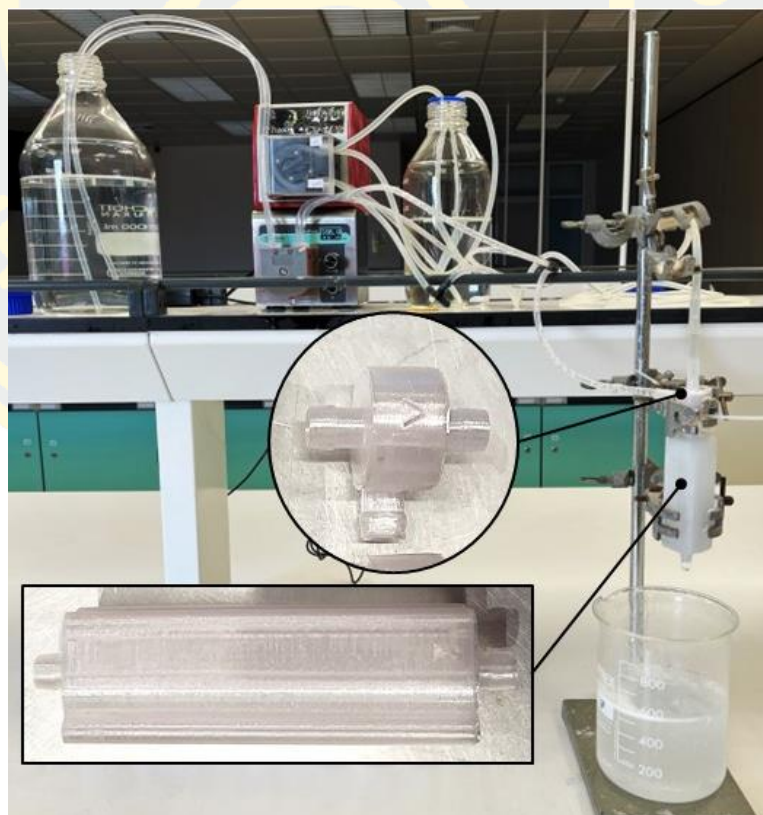


Figure 32 Schematic representation of the 3D printed vortex tube reactor and assembly.

5. Dispersion experiment

The residence time distribution (RTD) is an important characteristic of chemical reactors, providing a quantitative measure of the degree of back mixing within the system. The RTD of a vortex tube reactor was determined using erythrosine as a tracer in a series of experiments conducted at different flow rates. The $E(\theta)$ curves obtained from the experiments revealed significant differences in flow patterns with changing flow rate, as shown in Figure 33. At low flow rates of 10–60 mL/min, a broad $E(\theta)$ curve was observed, indicating a skewed distribution with a shorter mean residence time and some degree of back mixing inside the reactor. The $E(\theta)$ curves also showed a long tail of tracer, suggesting a wide range of residence times in the system. In contrast, at higher flow rates of 90–120 mL/min, the flow pattern was significantly narrower with a bimodal distribution, indicating a more uniform and less dispersed flow through the reactor vessel. An increase in flow rate led to an increase in the symmetry of the RTD curves, indicating the minimization of disturbances. However, all peaks of the $E(\theta)$ curves for different flow rates showed a value of θ lower than 1, indicating that most of the tracer spent less time in the reactor than the mean residence time. These findings suggest that the vortex tube reactor exhibits passive mixing and enhanced mixing efficiency with the increasing flow rate (86).

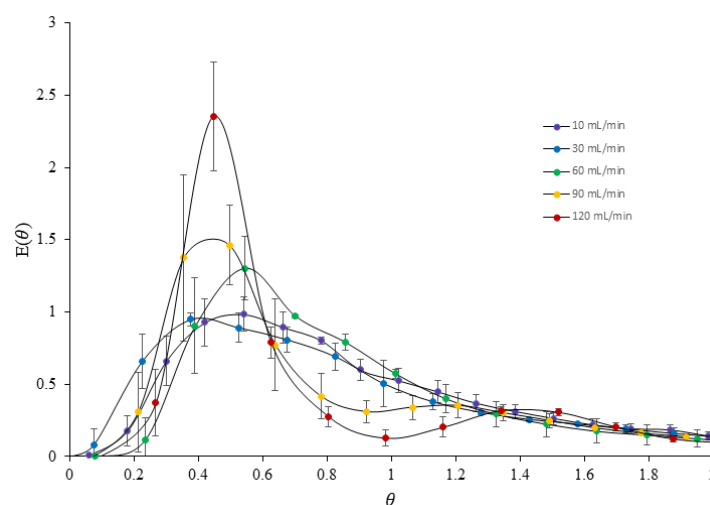


Figure 33 Comparison of $E(\theta)$ curves in different flow rate of the printed vortex tube reactor.

The results of the experiments also indicated that the degree of back mixing decreased with increasing flow rate due to increasing turbulence inside the reactor, which helps to enhance mass transfer and improve mixing efficiency. Table 19 shows that the decreasing value of the distribution variance (σ^2) at higher flow rates indicated that tracer flow through the vortex tube reactor was more homogeneous, making it closer to an ideal plug flow reactor. This result is consistent with computational fluid dynamics (CFD) simulations of the reactor, which have shown that increasing flow rate can enhance mixing efficiency.

Table 19 Mean residence times (t_m) and distribution variance (σ^2) of the 3D-printed optimized vortex tube reactor for the different flow rate.

Flow rate (mL/min)	t_m (sec)	σ^2
10	241.27	15601.41
30	66.48	1787.27
60	26.95	244.34
90	21.12	218.23
120	16.78	146.42

However, the $E(\theta)$ curve was inability to fit with the axial dispersion model (ADM) and the tank in series model (TIS). This model assumes a uniform flow and concentration profile, which may not be the case in a vortex tube reactor. As a result, the model may not be appropriate for our specific experimental setup and unable to obtain a significant fit to our data using standard fitting techniques. This suggests that the flow and mixing patterns in our system may be more complex than can be captured by the axial dispersion model and the tank in series model. While we explored alternative models and fitting techniques, we were unable to find a more appropriate model for our system.

6. Investigation of flow chemistry parameters in vortex tube reactor on formulated PGA nanoparticles

Prior to the preparation of lipid-based nanoparticles using a vortex tube reactor, the initial hurdle of the high cost associated with the lipid components

prompted the adoption of an alternative approach. Polyglycolic acid (PGA) was chosen for preparing PGA nanoparticles to reduce the potential for experimental errors. The utilization of PGA served the purpose of experimental validation, ensuring that the vortex tube reactor could effectively synthesize nanoparticles. This strategy allowed for a preliminary confirmation of the reactor's capability while maintaining flexibility for adjustments to enhance the properties of the nanoparticles.

In this section, the formulation of PGA nanoparticles was examined, focusing on the influence factor of input flow parameters, which consist of the total flow rate and the aqueous-to-organic volumetric ratio, on characteristics and performance. Additionally, a comprehensive comparison was conducted among PGA nanoparticles synthesized using three different methods, evaluating their respective advantages, limitations, and overall effectiveness.

6.1 Effect of input flow rate on formulated PGA nanoparticles

The aim of this test was to investigate the effect of input flow rate on the synthesis of PGA nanoparticles using a 3D-printed vortex tube reactor approach. The organic phase, consisting of 0.5% w/v PGA in acetone, was combined with an aqueous phase containing 0.5% w/v PVA in DI water, with a fixed ratio of 9:1 (aqueous phase: organic phase). The total flow rate was varied to assess its impact on the nanoparticle characteristics. Figure 34a illustrates the impact of varying the total flow rate on the characteristics of the formulated PGA nanoparticles. At a total flow rate of 68.92 mL/min, the highest z-average particle size was 337.03 ± 6.3983 nm and a PDI value of 0.366 ± 0.035 . Conversely, the lowest z-average particle size of 191.83 ± 2.95 nm and a PDI value of 0.365 ± 0.321 were obtained at a flow rate of 104.46 mL/min. Intriguingly, at a higher flow rate of 140.00 mL/min, the z-average particle size increased once again to 232.00 ± 17.05 nm, while the PDI value reached 0.431 ± 0.014 .

This observation suggests that there is an optimal flow rate of 104.46 mL/min for obtaining PGA nanoparticles with the desired particle size with a more uniform size distribution. This flow rate allows for optimal mixing and reaction conditions, leading to better control over particle formation and minimizing size variations. Higher flow rates result in shorter residence time, reducing the time

available for the nucleation and growth of nanoparticles. Lower flow rates, on the other hand, provide longer residence time, allowing for more significant particle growth and larger sizes. Flow rates higher than optimal can lead to incomplete reactions and particle agglomeration, preventing particles from reaching their desired size and causing the formation of larger aggregates. This agglomeration is more likely at higher flow rates due to the increased collision frequency between particles, favoring agglomeration over individual growth (87).

Overall, these results demonstrate the significant influence of input flow parameters, specifically the total flow rate, on the characteristics of the formulated PGA nanoparticles. It is important to carefully optimize the flow rate to achieve the desired particle size and size distribution.

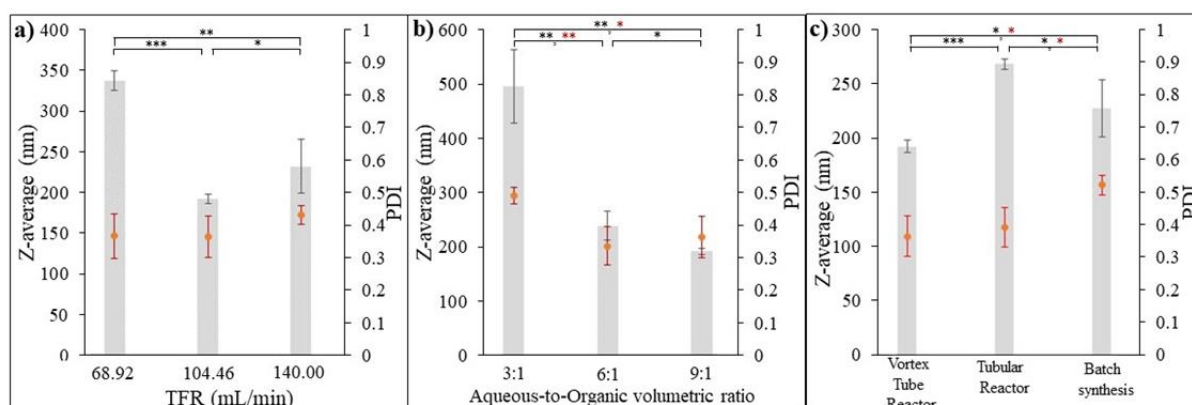


Figure 34 Z-average and PDI analysis of formulated PGA nanoparticles; (a) effect of input flow parameters, (b) effect of aqueous-to-organic volumetric ratio, and (c) comparison of formulated PGA nanoparticles using three different synthesis methods. Error bar represents 95% confidence interval. ($n = 3$, *p-value < 0.05, **p-value < 0.01, and ***p-value < 0.001 where a black star represents for significance of z-average and a red star represents for significance of PDI.)

6.2 Effect of aqueous-to-organic volumetric ratio on formulated PGA nanoparticles

To further investigate the influence of process parameters on the synthesis of PGA nanoparticles using flow chemistry, the volumetric ratio of the aqueous phase to the organic phase was varied while keeping the total flow rate constant at 104.46 mL/min. The organic phase consisted of 0.5% w/v PGA in acetone, while the aqueous phase contained 0.5% w/v PVA in DI water. The z-average particle size (nm) and polydispersity index (PDI) were measured to assess the impact of the ratio on particle characteristics. Figure 34b, presented in this study, illustrates the impact of the aqueous-to-organic volumetric ratio on the characteristics of the PGA nanoparticles that were formulated. By manipulating this ratio, variations in particle sizes were observed. When the ratio was set at 3:1 (aqueous-to-organic volumetric ratio), the z-average particle size measured 496.20 ± 34.13 nm, and the PDI value was 0.491 ± 0.013 . These results indicate a larger particle size and wider size distribution compared to the other ratios tested. However, as the ratio increased to 6:1 and 9:1, the z-average particle sizes decreased to 239.17 ± 13.45 nm and 191.83 ± 2.95 nm, respectively. Furthermore, the corresponding PDI values decreased to 0.337 ± 0.030 and 0.364 ± 0.032 , respectively. These findings suggest that increasing the proportion of the aqueous phase relative to the organic phase leads to smaller PGA nanoparticles and promotes a more uniform distribution of particle sizes. Increasing the aqueous phase ratio (i.e., increasing the proportion of the aqueous phase relative to the organic phase) generally results in improved particle size and size distribution uniformity for formulated PGA nanoparticles. This behavior can be attributed to the role of the aqueous phase, specifically the presence of polyvinyl alcohol (PVA), in the synthesis process. This might be because PVA acts as a stabilizer or surfactant in nanoparticle synthesis. It aids in controlling the growth and agglomeration of particles, leading to smaller and more uniformly dispersed nanoparticles. As the aqueous phase ratio increases, there is a higher concentration of PVA in the reaction mixture. This increased concentration of PVA helps to stabilize the PGA nanoparticles and inhibit particle growth or aggregation, resulting in smaller particle sizes. Conversely, a lower aqueous phase ratio (higher organic phase ratio) may limit the availability of PVA in the reaction mixture, leading to less effective stabilization and allowing for increased

particle growth or aggregation. This can result in larger particle sizes (88, 89). The results highlight the significance of the aqueous phase to organic phase ratio in controlling the particle size and size distribution of formulated PGA nanoparticles. Adjusting this ratio provides a means to tailor the particle characteristics according to the desired application requirements. Further optimization of the ratio, as well as investigating a wider range of ratios, could be explored to achieve precise control over particle size and size distribution.

6.3 Comparison of the formulated PGA nanoparticles using three different synthesis methods

The PGA nanoparticles were synthesized using three different synthesis methods to explore the impact of synthesis techniques on their properties. Firstly, we employed an optimized design 3D printed vortex tube reactor at the optimal conditions. Secondly, a tubular reactor, often referred to as the traditional reactor used in flow chemistry, has a 4 mm diameter and 80 cm length. This reactor operated under the same flow system conditions as 3D printed vortex tube reactor with a total flow rate of 104.46 mL/min and an optimal aqueous-to-organic volumetric ratio (9:1). Lastly, batch synthesis approach, often referred to as the traditional synthesis method, using the emulsification-solvent evaporation method for 12 hours with the same aqueous phase-to-organic phase ratio. These diverse synthesis methods were chosen to provide a comprehensive understanding of how variations in fabrication techniques influence the characteristics of PGA nanoparticles.

The size and size distribution comparison depicted in Figure 34c demonstrates that the 3D printed vortex tube reactor yields the smallest z-average values when compared to the tubular reactor (p -value < 0.001) and batch synthesis methods (p -value < 0.01). Specifically, the 3D printed vortex tube reactor exhibits z-average particle sizes of 191.83 ± 2.95 nm. In contrast, the tubular reactor and batch synthesis methods result in larger particle sizes of 267.33 ± 2.50 nm and 226.7 ± 13.20 nm, respectively. For PDI values, the 3D printed vortex tube reactor and tubular reactor exhibit lower PDI values compared to the batch synthesis approach. The 3D printed vortex tube reactor demonstrates a PDI value of 0.3643 ± 0.0321 , while the tubular reactor shows a PDI value of 0.3913 ± 0.0531 . On the other hand, the batch

synthesis method has a higher PDI value of 0.521 ± 0.016 . These results suggest that the utilization of the 3D printed vortex tube reactor and tubular reactor demonstrated a significant advantage over the batch synthesis method, as they yielded a notably more uniform particle size distribution. Moreover, both flow chemistry systems exhibited a remarkable ability to achieve fast and homogeneous mixing of reactants, which is particularly advantageous for sensitive and rapid nano-precipitation reactions (90).

Figure 35 displays the morphology of PGA nanoparticles prepared using both the 3D printed vortex tube reactor (Figure 35a) and the tubular reactor (Figure 35b). The SEM images revealed that the nanoparticles prepared from both methods exhibited a spherical shape, smooth surface, and agglomeration, forming clusters with nanoparticles sticking together. Interestingly, the nanoparticles produced by the 3D printed vortex tube reactor exhibited a smaller and more uniform size compared to those prepared by the tubular reactor. The PGA particle size from the 3D printed vortex tube reactor measured from SEM images was from 292.2 to 324.0 nm, while some particles in the samples from the tubular reactor reached dimensions up to 725.8 nm. This observation is consistent with the dynamic light scattering data (Figure 34c), despite the fact that the SEM particle size measurements indicated a larger particle size than the dynamic light scattering method, possibly as a result of sample preparation. This might be due to the drying and fixation processes on the solid substrate during SEM sample preparation. Some dispersed PVA might coat and aggregate the PGA nanoparticles, leading to particle aggregation or changes in particle size and shape (91).

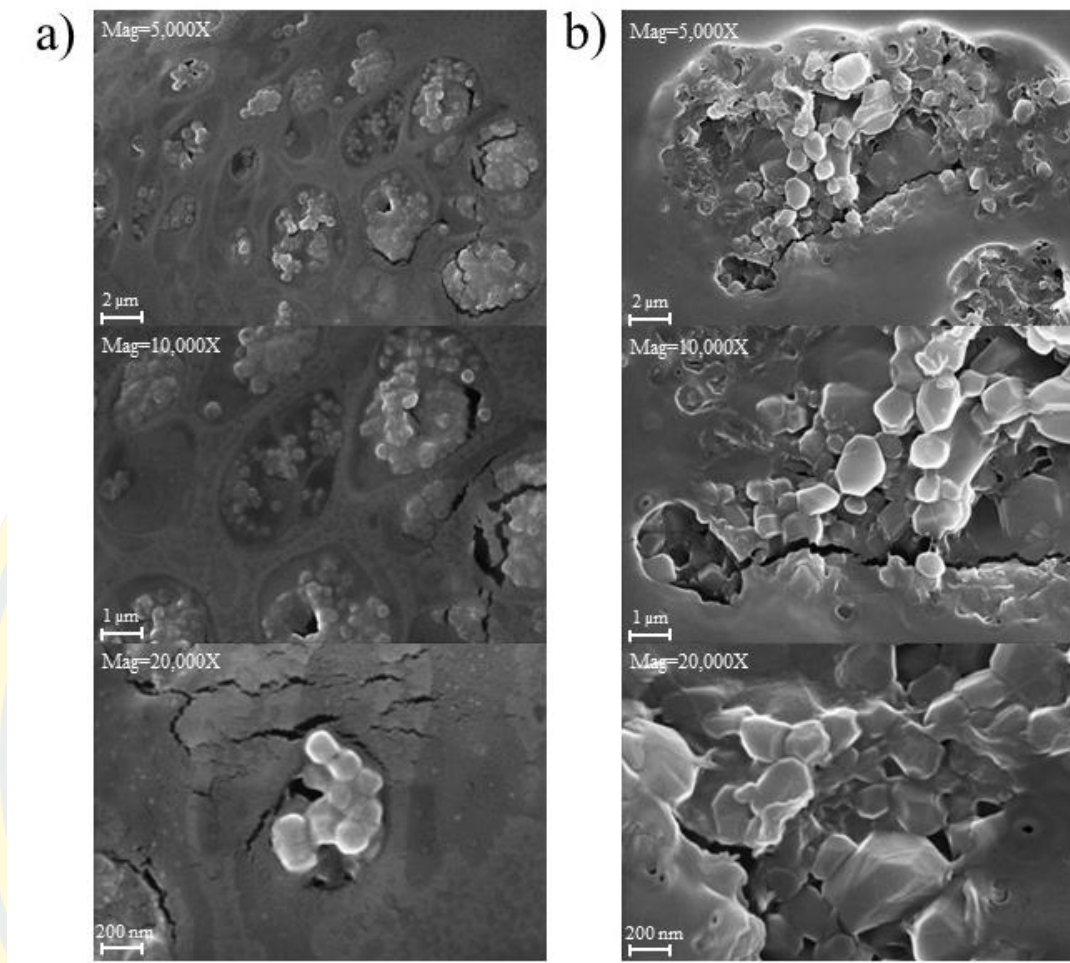


Figure 35 SEM image of PGA nanoparticles prepared using (a) a 3D printed vortex tube reactor and (b) a tubular reactor.

7. Experimental design of lipid-based nanoparticles formulation using a vortex tube reactor

After conducting a series of experiments focused on the synthesis of PGA nanoparticles utilizing a vortex tube reactor, noteworthy outcomes were achieved. The results indicated the successful formation of nanoparticles with the prospect of further enhancing their properties. Subsequently, lipid-based nanoparticles were formulated using the vortex tube reactor. The primary objective behind this endeavor was to optimize these lipid-based nanoparticles as effective carriers for the delivery of

bioproducts, thereby exploring their potential applications in the field of targeted drug delivery or other relevant biomedical applications.

The investigation of the relationship between flow system parameters and the formulation of lipid-based nanoparticles (LNPs), utilizing bovine serum albumin (BSA) as the biological model drug, in combination with DPPC, and cholesterol as lipids, was conducted using 3-factor, 3-level Box–Behnken design. The results of these experiments are summarized in Table 20. These experiments were analyzed using partial least square (PLS) regression to examine the correlations between the independent and dependent variables. Table 21 presents the findings regarding the relationships between the independent factors (X) and the responses (Y).

Table 20 Experimental runs and response results in the Block-Behnken design.

Run	X ₁ : Total flow rate (mL/min)	X ₂ : Aqueous-to-organic volumetric ratio	X ₃ : Number of reactor units (unit)	Y ₁ : Z-average (nm)	Y ₂ : PDI	Y ₃ : Zeta-potential (mV)	Y ₄ : %EE (%)	Y ₅ : %LC (%)	Y ₆ : Productivity (mg/min)
1	10	5.5	5	217.4	0.283	-8.25	31.11	24.75	21.27
2	55	1	1	211.7	0.164	-15.57	88.78	31.08	157.08
3	55	5.5	3	165.4	0.154	-16.07	56.38	34.23	153.29
4	10	1	3	212	0.235	-12.70	118.66	41.07	28.89
5	55	10	1	162.9	0.164	-15.97	42.68	20.48	208.40
6	100	5.5	1	153.1	0.135	-15.40	71.61	50.69	239.10
7	100	1	3	323.1	0.504	-13.53	88.94	22.72	391.50
8	55	5.5	3	166.6	0.15	-16.70	68.96	41.69	153.95
9	100	5.5	5	311.8	0.515	-10.47	61.29	37.87	273.90
10	100	10	3	258.4	0.147	-16.20	46.32	32.91	255.90
11	10	10	3	172.7	0.15	-13.90	60.04	40.12	27.21
12	55	10	5	256.4	0.344	-14.83	57.08	45.70	124.91
13	55	5.5	3	174.5	0.129	-16.03	59.00	32.72	167.81
14	10	5.5	1	158.2	0.125	-16.50	52.66	25.19	35.37
15	55	1	5	205.8	0.366	-13.10	95.35	32.87	159.56

Table 21 Partial least square regression model in terms of coded factors.

PLS models	<i>p</i> -value	F-value	R ²	Adjusted R ²
$Y_1 = -26.45X_1^2X_2 + 32.58X_1^2X_3 + 26.87X_1X_2^2 + 36.82X_1^2 + 35.90X_2^2 + 4.47X_3^2 - 6.35X_1X_2 + 24.88X_1X_3 + 24.85X_2X_3 + 22.33X_1 + 0.45X_2 + 21.90X_3 + 168.83$	0.0069*	144.36	0.9988	0.9919
Lack of fit	N/A	N/A		
$Y_2 = 0.0598X_1^2 + 0.0548X_2^2 + 0.0603X_3^2 - 0.0680X_1X_2 + 0.0555X_1X_3 - 0.0055X_2X_3 + 0.0635X_1 - 0.0580X_2 + 0.1150X_3 + 0.1443$	0.0460*	4.98	0.8996	0.7188
Lack of fit	0.0211*	46.51		
$Y_3 = -0.5308X_1 - 0.75X_2 + 2.10X_3 - 14.35$	0.0424*	3.82	0.5105	0.3769
Lack of fit	0.0312*	31.46		
$Y_4 = 0.7117X_1 - 23.20X_2 - 1.36X_3 + 66.59$	0.0167*	5.30	0.5909	0.4793
Lack of fit	0.1258	7.33		
$Y_5 = \text{Mean}$	<i>p</i> -value > 0.05 in all PLS models			
Lack of fit	0.2339	3.67		
$Y_6 = 130.96X_1 - 15.08X_2 - 7.54X_3 + 159.87$	<0.0001*	32.22	0.8978	0.8700
Lack of fit	0.0376*	26.01		

*indicating statistical significance (p-value < 0.05)

The PLS model, which was built using coded factors for Y_1 : z-average, Y_2 : polydispersity index, Y_3 : zeta-potential, Y_4 : % entrapment efficiency, and Y_6 : productivity, yielded significant results with *p*-values of 0.0069, 0.0460, 0.0424, 0.0167, and less than 0.0001, respectively. These *p*-values suggest that the model effectively explains the relationships between the independent variables and the dependent variables for these parameters. However, it's important to note that the model found Y_5 : %loading capacity to be non-significant (*p*-value > 0.05) in each PLS analysis, indicating that it may not play a significant role in explaining the variation in the dependent variables.

R² and adjusted R² values in the provided table assess the goodness of fit for various PLS models. Notably, the Y_1 and Y_6 models exhibit high R² and adjusted R-squared values, indicating a strong fit to the data. Conversely, the Y_2 , Y_3 , and Y_4

models have lower R^2 values, suggesting a lesser degree of explained variability. The adjusted R^2 values account for the number of predictors, penalizing irrelevant variables.

Lack of fit refers to the inadequacy of a model to capture the true underlying relationship between the independent and dependent variables. A cubic model in terms of Y_1 , which represents a type of polynomial regression model of degree 3, may not explicitly report a lack of fit for several reasons. Cubic models are more flexible than linear models, as they can capture complex, nonlinear relationships. Due to their higher degree, these models can fit the data closely, which might make it seem like they are performing well even when there is a lack of fit. The p-values of lack of fit in terms of Y_2 , Y_3 , and Y_6 suggest that the lack of fit is significant, indicating that the model might not be fully explaining the underlying relationships. Therefore, it may be necessary to find additional important variables or consider non-linear relationship patterns. In terms of Y_4 and Y_5 , the p-values of lack of fit are not significant, indicating that the model fits the data well.

7.1 Z-average (Y_1)

Z-average serves as a critical parameter with significant implications for the performance of LNPs in drug delivery applications. This study aims to assess the impact of three intriguing factors on BSA-loaded LNPs using a vortex tube reactor. The experimental results, summarized in Table 20, indicate substantial variations in z-average, ranging from 153.1 to 323.1 nm for LNPs under different combinations of X_1 , X_2 , and X_3 . The cubic model from PLS regression analysis, as presented in Table 21, reveals a highly significant relationship between the independent variables and Y_1 (p -value = 0.0069), with an impressively high R^2 (0.9988). This implies that the model effectively explains the variation in z-average, highlighting the robustness of the findings. Additionally, the response surface plots of key factors are depicted in Figure 36.

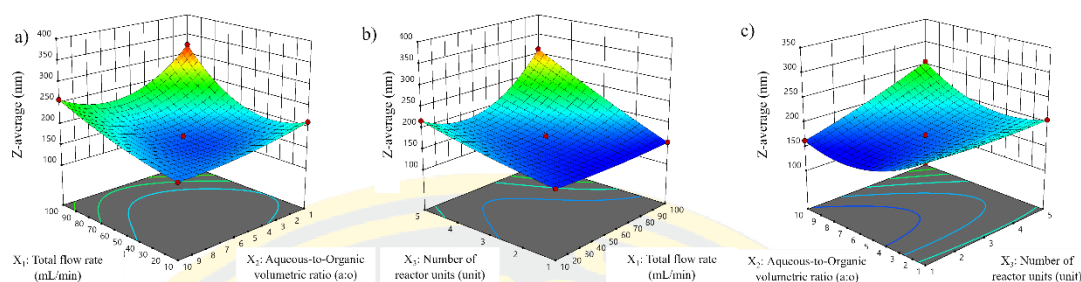


Figure 36 Response surface plot for z-average: (a) X_1 vs X_2 , (b) X_1 vs X_3 , and (c) X_2 vs X_3 .

The coefficients of the PLS equation unveil the relative importance of each variable in predicting the z-average. Positive coefficients are found for $X_1^2 X_3$ ($p = 0.0113$), $X_1 X_2^2$ ($p = 0.0165$), X_1^2 ($p = 0.0048$), X_2^2 ($p = 0.0051$), $X_1 X_3$ ($p = 0.0097$), $X_2 X_3$ ($p = 0.0098$), X_1 ($p = 0.0120$), and X_3 ($p = 0.0125$), indicating that these variables have the most significant positive influence on increasing the z-average. Conversely, a negative coefficient is found for $X_1^2 X_2$ ($p = 0.0170$), suggesting that these variables negatively impact the z-average. Other coefficients, such as X_3^2 ($p = 0.2244$), $X_1 X_2$ ($p = 0.1240$), and X_1 ($p = 0.8723$), have smaller effects on the z-average. These factors may be less critical for predicting z-average, and their influence may be overshadowed by the larger effects of other factors. In the PLS model for Y_1 , the factors X_1 and X_2 have both positive and negative coefficients in the difference term, indicating that increasing these factors can lead to a decrease in the Z-average, but extreme values of these factors can increase it.

This study also examines how each factor, X_1 , X_2 , and X_3 , influences particle size individually while keeping the other factors constant. When solely increasing the total flow rate (X_1), while holding X_2 and X_3 constant, intriguing insights emerge. The PLS model suggests that X_1 has a quadratic effect on particle size, as indicated by the term X_1^2 in the model equation. As X_1 increases, particle size tends to grow non-linearly. Initially, there is a gradual increase in particle size, but beyond a certain point, the rate of particle size growth accelerates more rapidly, and may lead to increased collision frequency between the reactants, resulting in larger

LNPs. Hence, meticulous control and optimization of the total flow rate are essential for achieving the desired particle size in LNP synthesis (87).

Exploring the impact of varying the aqueous-to-organic volumetric ratio (X_2) while keeping X_1 and X_3 constant reveals a complex relationship. The PLS model indicates that X_2 has both linear and quadratic effects on particle size. The term $X_1X_2^2$ implies that increasing X_2 leads to a quadratic increase in particle size, suggesting that larger LNPs tend to form when the aqueous phase dominates the solvent ratio. LNPs are often formed through the self-assembly of lipids, and the size of the resulting particles can be influenced by the solubility of the components. A higher aqueous-to-organic volumetric ratio might change the solubility of lipids, affecting their self-assembly rate and leading to larger particle sizes. However, the presence of the negative term suggests that the interaction between X_1 and X_2 has a negative linear and quadratic effect on particle size. This interaction implies that while increasing X_2 alone may promote larger particles, the presence of a higher X_1 can partially counteract this effect. Achieving the desired particle size by adjusting X_2 alone may require careful consideration of the X_1 value, emphasizing the need to balance solvent ratios with other factors for precise control over particle size (92).

Examining the impact of increasing the number of reactor units (X_3) while keeping X_1 and X_2 constant provides further insights. The interaction term $X_1^2X_3$ in the PLS model indicates that X_3 interacts with the squared total flow rate (X_1^2) to influence particle size. Increasing X_3 alongside X_1^2 tends to have a quadratic effect on particle size, suggesting that more reactor units can lead to larger particle sizes, especially when combined with higher flow rates. Adding more reactor units provides additional residence time for particles to grow, resulting in larger LNPs. However, this effect is influenced by the flow rate (X_1), so the choice of the number of reactor units should be considered in conjunction with the desired particle size and specific flow rate conditions (93).

Overall, these findings are valuable for designing and optimizing similar systems, as they offer insights into the factors with the greatest impact on z-average. The high significance and accuracy of the PLS model also suggest its utility as a valuable tool for predicting z-average in this system.

7.2 Polydispersity index (Y_2)

The Polydispersity Index (PDI) is a crucial metric for assessing the uniformity of particle size distribution within synthesized BSA-loaded LNPs. A lower PDI value indicates a more even distribution of particle sizes, while a higher PDI value suggests a broader range of particle sizes, which could potentially affect the stability and performance of LNPs. The experimental results, summarized in Table 20, reveal significant variations in the PDI, ranging from 0.135 to 0.366 for LNPs under different combinations of independent variables, denoted as X_1 , X_2 , and X_3 . Utilizing a quadratic model derived from PLS regression analysis, as presented in Table 21, demonstrates a substantial relationship between these independent variables and Y_2 (p -value = 0.0460) along with an impressive R^2 of 0.8996. This indicates that the model effectively explains the variation in PDI, underscoring the reliability of the findings. Moreover, the response surface plot of the key factors is illustrated in Figure 37.

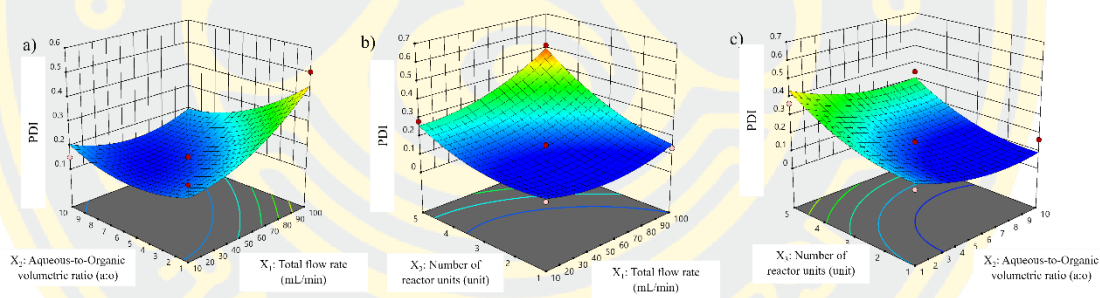


Figure 37 Response surface plot for PDI: (a) X_1 vs X_2 , (b) X_1 vs X_3 , and (c) X_2 vs X_3 .

The coefficients of the PLS equation unveil the relative importance of each variable in predicting PDI. The variable X_3 ($p = 0.0061$) stands out with the highest positive coefficient, suggesting that it has the most significant positive influence on increasing PDI. On the other hand, coefficients of non-significant variables exhibit smaller effects on PDI prediction, with positive terms like X_1^2 ($p = 0.1685$), X_2^2 ($p = 0.2003$), X_3^2 ($p = 0.1656$), X_1X_3 ($p = 0.1810$), X_1 ($p = 0.0536$), as well as negative terms like X_1X_2 ($p = 0.1153$), X_2X_3 ($p = 0.8837$), and X_2 ($p = 0.0701$). These factors are likely less critical in predicting PDI, with their impact overshadowed by other variables. To further investigate the influence of the number of reactor units (X_3) on

PDI, experiments were conducted while maintaining X_1 and X_2 at constant levels. The PLS model for PDI (Y_2) indicates that the linear effect of X_3 significantly impacts PDI, as suggested by the coefficient of X_3 in the model equation. This implies that increasing the number of reactor units (X_3) has a direct, positive linear effect on PDI, resulting in a broader particle size distribution. These results underscore the importance of the number of reactor units (X_3) in governing particle size uniformity within LNPs. Increasing the number of reactor units allows for additional residence time for particles to grow, potentially leading to a broader particle size distribution (93, 94).

These findings hold value for the design and optimization of similar systems, providing insights into factors influencing PDI. The significance and accuracy of the PLS model also suggest its utility as a valuable tool for predicting PDI in this system.

7.3 Zeta-potential (Y_3)

The zeta-potential serves as a critical parameter for characterizing the surface charge of synthesized LNPs. The experimental results, summarized in Table 20, reveal substantial variations in the zeta-potential, ranging from -16.70 to -8.25 mV for LNPs under different combinations of X_1 , X_2 , and X_3 . The linear model obtained from the PLS regression analysis, as presented in Table 21, demonstrates a highly significant relationship between the independent variables and Y_3 (p-value = 0.0424), with an R^2 of 0.5105. This finding effectively explains the variation in zeta-potential, highlighting the robustness of the results. Additionally, Figure 38 depicts the response surface plot of the key factors.

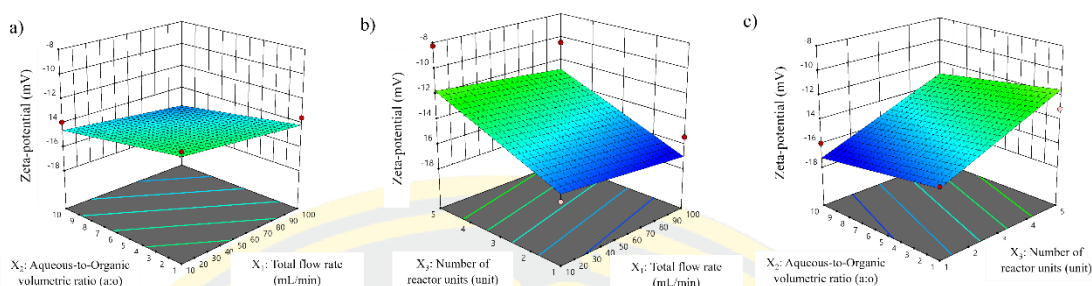


Figure 38 Response surface plot for zeta-potential: (a) X_1 vs X_2 , (b) X_1 vs X_3 , and (c) X_2 vs X_3 .

The coefficients in the PLS equation unveil the relative importance of each variable in predicting zeta-potential. Notably, the variable X_3 ($p = 0.0101$) stands out with the highest positive coefficient, indicating its significant positive influence on increasing zeta-potential. Conversely, non-significant variables exhibit smaller effects on zeta-potential prediction, with negative coefficients for X_1 ($p = 0.4490$) and X_2 ($p = 0.2910$). These factors are less critical in predicting zeta-potential, with their impact overshadowed by other variables.

The PLS model for Y_3 underscores the significant linear effect of X_3 on zeta-potential, as suggested by the coefficient of X_3 in the model equation. This implies that an increase in X_3 is expected to lead to a more positive zeta-potential. In this context, a higher zeta-potential indicates reduced electrostatic repulsion among particles and potentially decreased stability within the negatively charged system. It is essential to consider any surface modification or charge introduced due to prolonged residence time, which may involve DPPC molecules or interactions between DPPC and other components in the LNPs. Therefore, while an increase in X_3 may still result in a more positive zeta-potential, as discussed earlier. The specific behavior of DPPC in this context should be taken into account when analyzing the results and implications for LNPs. Consequently, the extended residence time associated with higher X_3 values may promote weaker electrostatic repulsion, leading to a more positive zeta-potential and potentially impacting the stability of LNPs (95, 96). This underscores the significance of X_3 in controlling zeta-potential and particle stability

within negatively charged LNPs, emphasizing the need for careful consideration when optimizing X_3 to achieve the desired electrostatic properties.

These findings are valuable for the design and optimization of similar systems, providing insights into factors influencing zeta-potential. The significance and accuracy of the PLS model also suggest its utility as a valuable tool for predicting zeta-potential in this system.

7.4 Entrapment efficiency percentage (Y_4)

The entrapment efficiency percent (%EE) serves as a critical metric in the synthesis of LNPs since it quantifies the proportion of encapsulated materials, such as drugs or bioactive compounds, within the LNPs. A higher %EE is desirable as it indicates the successful encapsulation of a greater quantity of the active ingredient within the LNPs. The experimental results, which are summarized in Table 20, demonstrate substantial variations in %EE, ranging from 31.11 to 118.66% for LNPs under different combinations of X_1 , X_2 , and X_3 . Through a PLS regression analysis, as presented in Table 21, a significant relationship between the independent variables and y_4 (p-value = 0.0167) has been established, with an R^2 of 0.5909. This outcome effectively explains the variance in %EE and underscores the robustness of the results. Additionally, Figure 39 illustrates a response surface plot of the key factors.

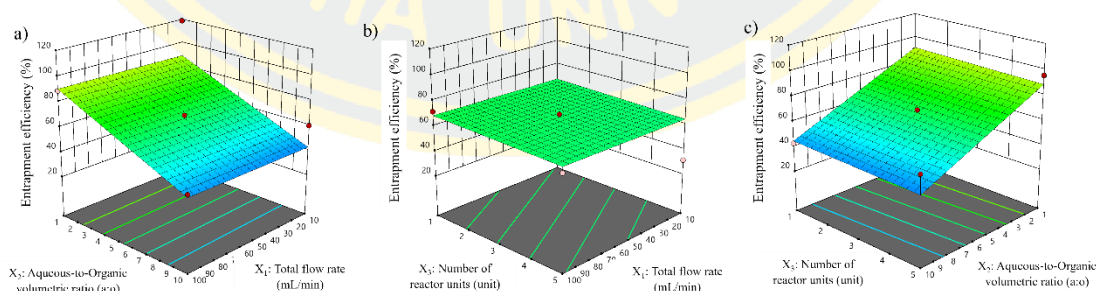


Figure 39 Response surface plot for percentage entrapment efficiency: (a) X_1 vs X_2 , (b) X_1 vs X_3 , and (c) X_2 vs X_3 .

The coefficients in the PLS equation reveal the relative importance of each variable in predicting %EE. Notably, X_2 ($p = 0.0022$) stands out with the highest negative coefficient, signifying its substantial negative influence on reducing %EE. Conversely, non-significant variables exhibit smaller effects on %EE prediction, with positive coefficients for X_1 ($p = 0.9051$) and negative coefficients for X_3 ($p = 0.8197$). These factors play a less critical role in predicting %EE, with their impact overshadowed by other variables. The PLS model for Y_4 underscores the significant linear effect of X_2 on %EE, as indicated by the coefficient of X_2 in the model equation. This suggests that the choice of this ratio plays a critical role in determining the encapsulation efficiency of BSA in the lipid nanoparticles.

The significance of X_2 lies in its capacity to influence the emulsification process. Our findings suggest that maintaining a lower aqueous-to-organic volumetric ratio enhances encapsulation efficiency, aligning with the principle of emulsion stability. At lower ratios, the organic phase predominates in the mixture. This results in reduced interfacial tension between the aqueous and organic phases, which, in turn, promotes the formation of smaller and more stable organic droplets within the aqueous phase. Smaller droplets provide a larger surface area for interaction between BSA molecules and the lipid components, facilitating efficient encapsulation. Furthermore, lower values of X_2 may lead to a higher concentration gradient between the aqueous and organic phases, effectively driving BSA molecules into the lipid bilayer and further enhancing encapsulation efficiency (97, 98).

7.5 Loading capacity percentage (Y_5)

Investigating the crucial parameter of the percentage of loading capacity (%LC) and its relationship with various independent variables using PLS models, the study uncovered a surprising result of %LC did not exhibit statistical significance within these models. This lack of significance can be attributed to various factors within the experimental setup. Firstly, inherent experimental variability or noise in the data on weighting method for %LC may obscure any potential relationships with the independent variables. The dataset for %LC displayed notable variability, with a minimum value of 20.48%, a maximum value of 50.69%, and a mean value of 34.27%. Secondly, the encapsulation process in LNPs is a multifaceted and intricate

process influenced by numerous factors, and the variables considered in the PLS models may not fully capture the complexity of this system. There could be other unexplored variables that play a more substantial role in determining %LC. Additionally, the weighting method for low volume of lyophilized products in terms of %LC may have limitations, potentially diminishing the statistical power to identify significant relationships. Furthermore, the nature of the encapsulation process itself might not strongly depend on the factors under investigation. To gain deeper insights into the determinants of %LC in LNPs.

7.6 Productivity (Y_6)

Productivity in a research context is a measure of the rate or efficiency at which a desired product or outcome is produced per unit of input, such as time, materials, or resources. It reflects the effectiveness of a given process or system. The experimental results presented in Table 20 reveal significant variations in productivity, ranging from 21.27 to 273.90 mg/min for lipid nanoparticles, depending on the combinations of variables X_1 , X_2 , and X_3 . A comprehensive analysis, utilizing PLS regression as detailed in Table 21, has established a strong relationship between the independent variables and the dependent variable Y_6 (p -value < 0.0001), yielding an impressive R^2 of 0.8978. This outcome effectively explains the variance in productivity and underscores the robustness of the results. Moreover, Figure 40 visually represents the response surface plots of the key factors, providing a more intuitive understanding of their impact.

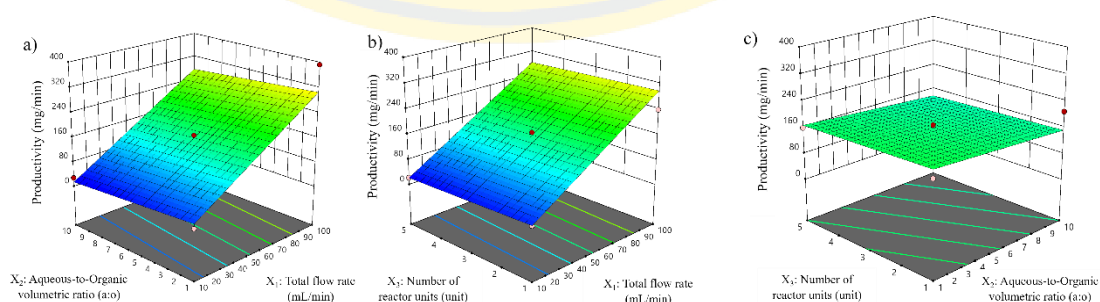


Figure 40 Response surface plot for productivity: (a) X_1 vs X_2 , (b) X_1 vs X_3 , and (c) X_2 vs X_3 .

Examining the coefficients within the PLS equation allows us to gauge the relative importance of each variable in predicting productivity. Remarkably, X_1 ($p < 0.0001$) emerges as the most influential variable with a significant positive coefficient, signifying its substantial positive effect on increasing productivity. Conversely, non-significant variables exhibit smaller effects on productivity prediction, with positive coefficients for X_2 ($p = 0.2855$) and negative coefficients for X_3 ($p = 0.5858$). These factors play a less critical role in predicting productivity, with their impact being overshadowed by other variables.

The PLS model has shed light on the critical role played by the total flow rate (X_1) in shaping the productivity (Y_6) of the BSA-loaded lipid-based nanoparticles synthesis process. The highest positive coefficient for X_1 indicates that an increase in the total flow rate has a positive impact on productivity. One key factor contributing to this positive impact is the enhancement of mass transport and mixing within the reactor. As the flow rate increases, more reactants are introduced into the reaction zone, facilitating efficient diffusion and distribution of reactants, thus expediting reactions. Improved mixing ensures that reactants are consistently exposed to each other, minimizing concentration gradients and reducing the likelihood of localized areas with reduced reaction rates.

These findings are invaluable for the design and optimization of similar systems, providing valuable insights into the factors influencing productivity. The significance and accuracy of the PLS model also highlights its utility as a valuable tool for predicting productivity within this system, offering researchers a reliable means to optimize processes and achieve higher productivity.

8. Optimization condition for lipid-based nanoparticles formulation using a vortex tube reactor

After completing the experimental design, PLS models and response surfaces were generated and the constraints for all factors determined the desirability of all responses, as presented in Table 14. The optimization of lipid-based nanoparticles formulation using a vortex tube reactor followed, yielding prediction values for factors X_1 , X_2 , and X_3 , which were determined as 100 mL/min for the total

flow rate, 5.278 for the aqueous-to-organic volumetric ratio, and 1 unit for the reactor, respectively. Subsequently, lipid-based nanoparticles were prepared under these optimized conditions (optimized solution 1). Table 22 provides insight into the prediction accuracy, with percentages comparing predicted responses from the partial least squares regression models to actual test values. Remarkably, the actual values closely matched the predicted values, despite a low R^2 and the presence of a significant lack of fit in some relationships. For the response variables, the prediction ability for Y_1 , Y_2 , Y_3 , Y_4 , Y_5 , and Y_6 occurred at 93.50%, 96.48%, 94.78%, 97.05%, 96.49%, and 95.22%, respectively, resulting in the highest desirability value of 0.742. These high prediction percentages for both factors and response variables affirm the successful optimization process, indicating that the chosen conditions for lipid-based nanoparticle formulation using a vortex tube reactor can significantly improve z-average, polydispersity index, zeta potential, percentage entrapment efficiency, percentage loading capacity, and productivity.

Table 22 Comparison between the predicted values form PLS models and the actual values of three difference optimized condition for lipid-based nanoparticle using the vortex tube reactor.

Optimized solution	Desirability value	Factor (X) and response (Y)	Unit	Calculated independent factor (X) and prediction values (Y)	Standard deviation of prediction values	Standard error of predicted mean	95%CI low for predicted mean	95%CI high for predicted mean	Actual values	Percentage of prediction ability (%)
1	0.742	X_1 : Total flow rate	mL/min	100.00						
		X_2 : Aqueous-to-organic volumetric ratio	-	5.28						
		X_3 : Number of reactor unit	Unit	1.00						
		Y_1 : Z-average	nm	156.08	4.94	4.94	134.80	177.34	166.23	93.50%
		Y_2 : PDI	-	0.16	0.07	0.06	0.00	0.32	0.17	96.48%
		Y_3 : Zeta-potential	mV	-16.94	1.91	1.08	-19.31	-14.57	-16.06	94.78%
		Y_4 : %EE	%	69.81	16.50	9.29	49.36	90.25	67.75	97.05%
Y_5 : %LC	%	37.71	12.41	10.75	10.07	65.34	36.39	96.49%		
		Y_6 : Productivity	mg/min	299.12	37.99	21.39	252.04	346.19	313.40	95.22%

		X ₁ : Total flow rate	mL/min	100.00						
		X ₂ : Aqueous-to-organic volumetric ratio	-	5.50						
		X ₃ : Number of reactor unit	Unit	1.00						
2	0.742	Y ₁ : Z-average	nm	153.10	4.94	4.94	131.82	174.37	165.63	91.81%
		Y ₂ : PDI	-	0.16	0.07	0.06	-0.00	0.32	0.15	91.77%
		Y ₃ : Zeta-potential	mV	-16.98	1.91	1.08	-19.34	-14.60	-16.03	94.45%
		Y ₄ : %EE	%	68.66	16.50	9.29	48.23	89.10	69.69	98.51%
		Y ₅ : %LC	%	37.63	12.41	10.74	10.01	65.25	38.73	97.09%
		Y ₆ : Productivity	mg/min	298.37	37.99	21.38	251.32	345.42	301.90	98.82
		X ₁ : Total flow rate	mL/min	72.06						
		X ₂ : Aqueous-to-organic volumetric ratio	-	4.24						
		X ₃ : Number of reactor unit	Unit	1.00						
3	0.703	Y ₁ : Z-average	nm	163.19	4.94	3.52	148.10	178.37	154.47	94.65%
		Y ₂ : PDI	-	0.13	0.07	0.05	0.01	0.25	0.12	96.32%
		Y ₃ : Zeta-potential	mV	-16.437	1.91	0.90	-18.41	-14.47	-16.63	98.81%
		Y ₄ : %EE	%	74.70	16.50	7.73	57.71	91.73	67.00	89.69%
		Y ₅ : %LC	%	35.44	12.41	8.09	14.66	56.23	35.58	99.63%
		Y ₆ : Productivity	mg/min	221.27	37.99	17.79	182.12	260.45	227.61	97.13%

Figure 41 presents the morphology of lipid-based nanoparticles that have been prepared under optimized conditions using a vortex tube reactor. Our examination of these nanoparticles through both transmission electron microscopy (TEM) and scanning electron microscopy (SEM) has revealed that they exhibit a spherical shape with a smooth surface texture of well-formed lipid nanoparticles. TEM images allowed us to observe the internal structure of the nanoparticles. The lipid layer of DPPC and cholesterol was clearly visible, surrounding the BSA core. This core-shell structure is consistent with the expected composition of the nanoparticles, where the hydrophobic lipid bilayer encapsulates the hydrophilic BSA cargo. The measurements of particle size obtained from TEM and SEM images were found to be 117.46 ± 23.74 nm and 152.74 ± 31.00 nm, respectively. Interestingly, these observations align with the data acquired from dynamic light scattering. However, it is worth noting that the particle sizes determined through TEM and SEM

appeared to be smaller than those obtained using the dynamic light scattering method. This discrepancy may be attributed to the inherent differences in sample preparation techniques. Specifically, during the sample preparation process, the nanoparticles underwent drying and fixation procedures on a solid substrate. These steps could have introduced alterations in both the size and shape of the particles. As a result, the particle size data obtained from TEM and SEM should be interpreted in the context of the sample preparation steps, acknowledging the potential impact of these processes on the observed particle characteristics (91).

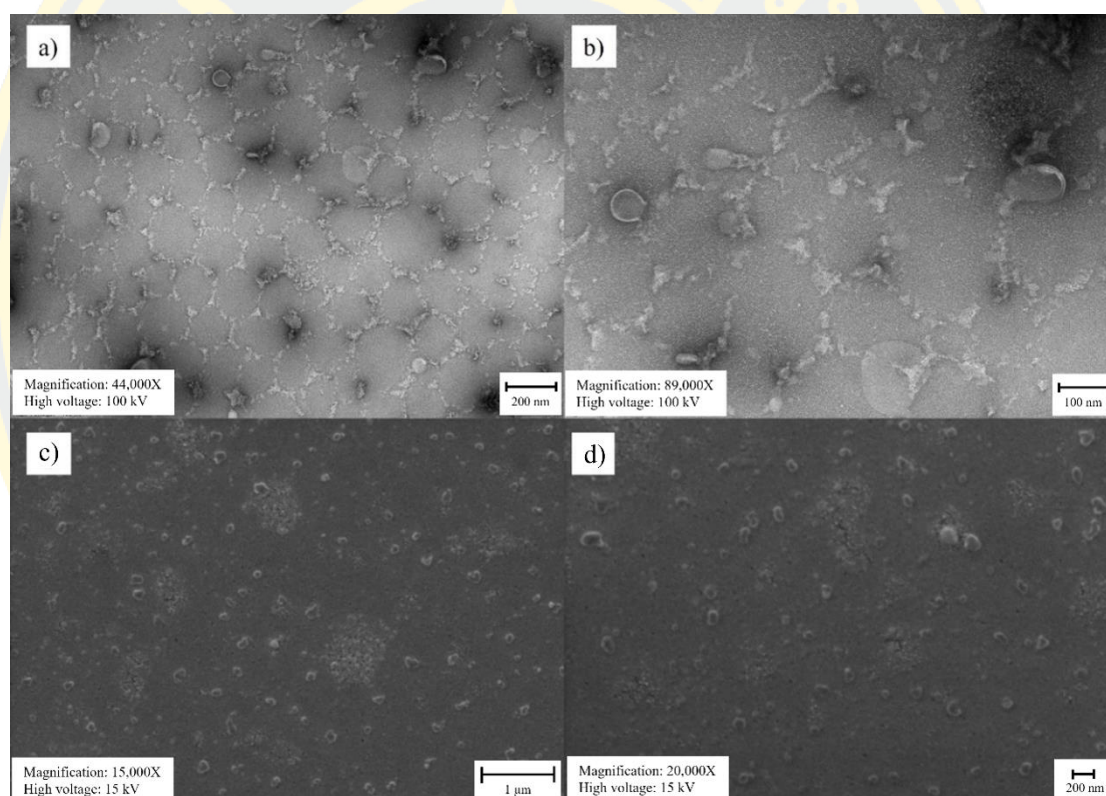


Figure 41 TEM and SEM images of lipid-based nanoparticles using the vortex tube reactor: (a) TEM image at 44,000X, (b) TEM image at 89,000X, (c) SEM image at 15,000X, and (d) SEM image at 20,000X.

9. Prediction performance

To assess the accuracy of the PLS equation derived from the DoE, the prediction performance was evaluated by comparing the predicted values with the actual values. Three optimized solution points were selected within the design space and subjected to triplicate sample evaluations. This comparison involved verifying that the percentage of prediction ability and the actual values fell within the 95% confidence interval of the predicted values, ensuring both the reliability of the PLS model and the effectiveness of the DoE approach in optimizing parameters for synthesizing the desired product.

Table 22 also provides a comparison between the predicted and actual values for various parameters in three different optimized solutions. In the results, the predicted values of all optimized solutions closely matched the actual values, demonstrating a high percentage of prediction ability. The results also indicated that the actual values fell within the 95% confidence interval of the predicted values (p -value > 0.05), as illustrated in Figure 42. These findings suggest that the PLS model developed through the DoE approach is effective in predicting the key parameters related to the synthesis of the desired product. The high percentage of prediction ability values across various parameters further demonstrates the model's reliability. These findings underscore the value of employing a data-driven approach such as DoE in optimizing processes and ensuring product quality.

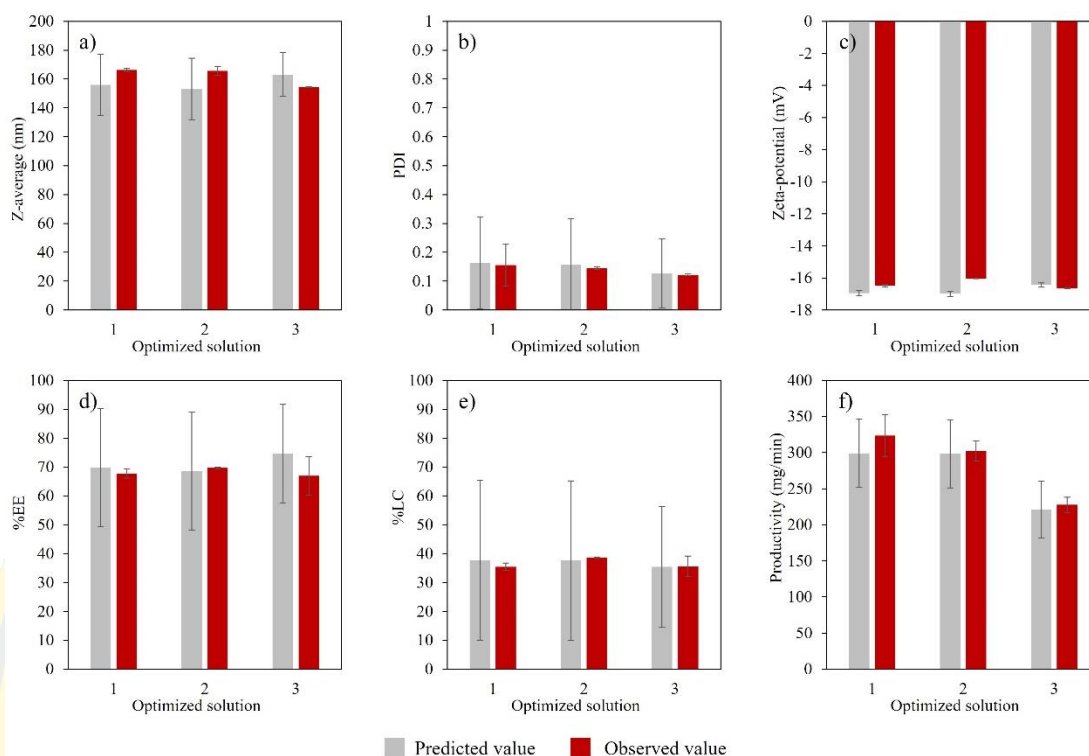


Figure 42 Comparison between the predicted values and the actual values of three difference optimized solutions for lipid-based nanoparticle using the vortex tube reactor based on (a) z-average, (b) PDI, (c) zeta-potential, (d) %EE, (e) %LC, and (f) productivity. Error bar represents 95% confidence interval.

10. Formulation uniformity over formulated time

Ensuring the uniformity of a formulation across multiple lots stands as a pivotal stage in the successful scale-up of any manufacturing process, particularly in industries as critical as pharmaceuticals and biopharmaceuticals. Control charts have emerged as indispensable tools for evaluating process performance, offering a means to measure, monitor, and control production processes effectively. Their widespread adoption within pharmaceutical and biopharmaceutical manufacturing underscores their significance.

The control chart of the moving range (MR) method played a central role in this study, where the objective was to validate the consistency of the optimized formulations. Over separate production runs, six lots of optimized lipid-nanoparticle

formulation (referred to as optimized solution 1) were generated. A rigorous analysis was conducted, meticulously calculating control limits (CL), encompassing the mean, upper control limit (UCL), and lower control limit (LCL), a comprehensive process documented in the Appendix. This rigorous approach ensured the process's reliability and consistency.

The results depicted in Figure 43, which illustrates the z-average, PDI, zeta-potential, %EE, %LC, and productivity across various lots of lipid-based nanoparticles, offer compelling evidence. Both the X-chart and MR-chart demonstrate a remarkable absence of variability across the sampled lots. Each measurement consistently falls within the confines delineated by the upper and lower control limits. Notably, no data points stray beyond the boundaries of system stability. These control charts provide strong indications that the parameters governing the operation of the vortex tube reactor remain steadfast for lipid-based nanoparticle formulation (99, 100).

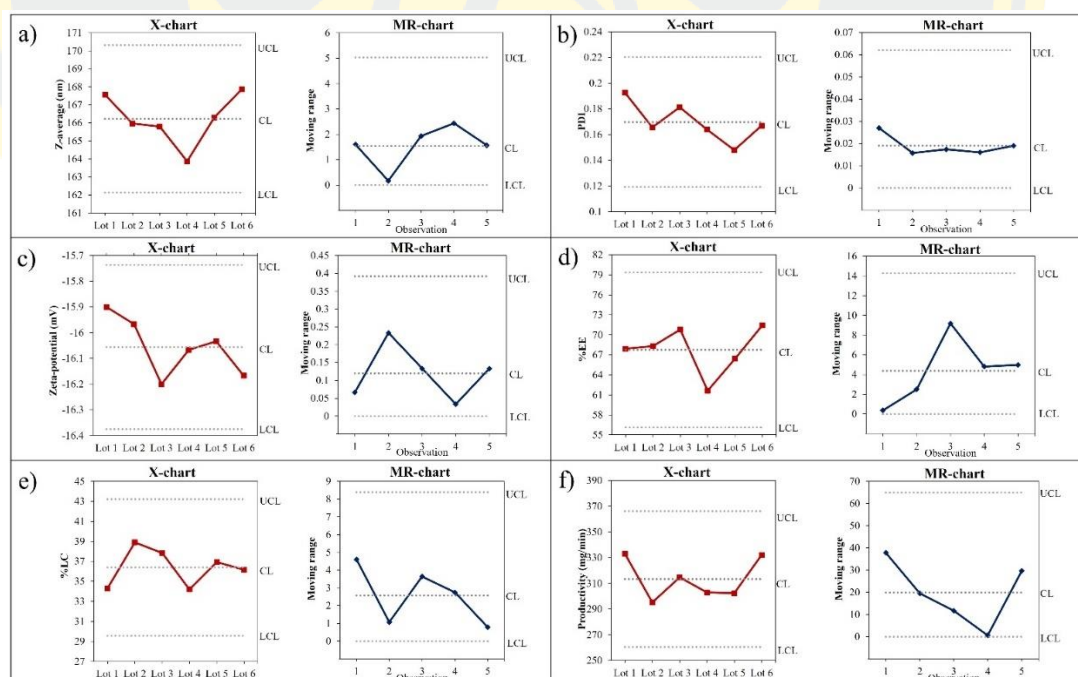


Figure 43 X-chart and MR-chart of (a) z-average, (b) PDI, (c) zeta-potential, (d) %EE, (e) %LC, and (f) productivity across 6 lots of lipid-based nanoparticles formulation.

Upon scrutinizing these experimental outcomes, the affirmation of the formulation process's consistency becomes unequivocal. Further, the reproducibility of the optimized formulations stands clearly demonstrated. The insights gained from this study will serve as a cornerstone for future optimization efforts. They will be instrumental in maintaining consistent product quality throughout large-scale production, ensuring that the formulations continue to meet stringent standards of excellence in pharmaceutical and biopharmaceutical manufacturing.

11. Comparison of lipid-based nanoparticle formulation between vortex tube reactor and batch synthesis

To compare lipid-based nanoparticles formulation synthesized through a vortex tube reactor with the optimized condition (optimized solution 1) and a batch synthesis approach employing the conventional emulsification-solvent evaporation method. Both methods utilized the same aqueous phase-to-organic phase ratio and produced the same final product volume. In the batch synthesis, samples were collected at intervals ranging from 5 to 30 minutes for particle dispersion analysis using a Zetasizer until the desired product quality was achieved. Interestingly, after 15 minutes of synthesis, there was no observable change in particle dispersion. Therefore, it was assumed that the process had reached its optimal state at this point, and calculations of productivity were based on this 15-minute time frame.

The comparison between the two synthesis methods, as illustrated in Figure 44, reveals that the vortex tube reactor yielded nanoparticles with a lower z-average size (p-value = 0.0156) and a lower PDI (p-value < 0.01). Additionally, it exhibited higher percentages of entrapment efficiency (p-value < 0.01), loading capacity (p-value < 0.01), and productivity (p-value < 0.01). However, there was no significant difference in zeta-potential (p-value = 0.4953) between the two methods. To provide more specific data, the vortex tube reactor resulted in nanoparticles with a z-average size of 166.23 ± 0.98 nm and a PDI value of 0.17 ± 0.01 , whereas the batch synthesis method produced larger particles with a size of 192.67 ± 9.40 nm and a PDI value of 0.25 ± 0.01 . The zeta-potential measurements showed no significant difference, with values of -16.06 ± 0.27 mV for the vortex tube reactor and -16.07 ± 1.64 mV for the

batch synthesis. Regarding % entrapment efficiency, % loading capacity, and productivity, the vortex tube reactor outperformed the batch synthesis method. Specifically, the vortex tube reactor achieved % entrapment efficiency, % loading capacity, and productivity values of $67.75 \pm 1.55\%$, $36.39 \pm 0.83\%$, and 313.4 ± 12.88 mg/min, respectively. In contrast, the batch synthesis method exhibited lower values for % entrapment efficiency ($49.09 \pm 0.65\%$), % loading capacity ($28.99 \pm 0.38\%$), and productivity (1.05 ± 0.13 mg/min).

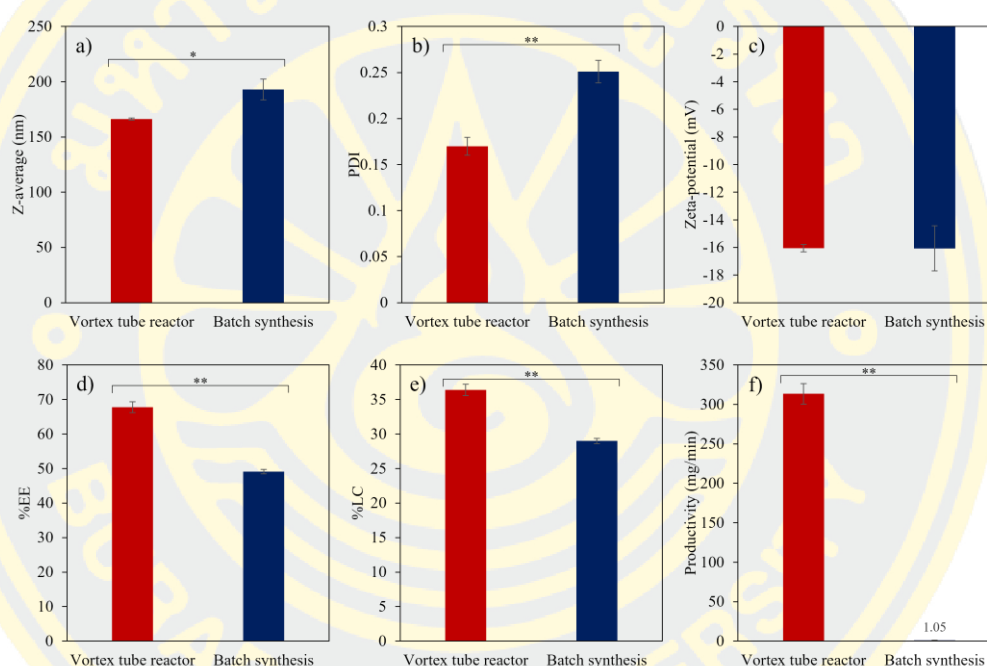


Figure 44 Comparison of lipid-based nanoparticle formulation: Vortex tube reactor vs. Batch synthesis; (a) z-average, (b) PDI, (c) zeta-potential, (d) %EE, (e) %LC, and (f) productivity. Error bar represents 95% confidence interval. (*p-value < 0.05, and **p-value < 0.01).

The 3D printed vortex tube reactor demonstrates clear advantages over the batch synthesis method in terms of smaller particle size, more uniform nanoparticles, higher entrapment and loading capacity suggests higher productivity compared to batch synthesis method. Consequently, the enhanced productivity of the vortex tube reactor in generating nanoparticles with favorable properties reinforces its potential as an efficient and reliable method for nanoparticle synthesis.

CHAPTER 5

CONCLUSION

In conclusion, this comprehensive study has delved deep into the mixing performance and flow characteristics of the vortex tube reactor, employing a combination of computational fluid dynamics simulations, a meticulously planned design of experiments, and meticulous optimization techniques. Throughout this research endeavor, we have gained profound insights into the critical factors influencing both the mixing index and the Reynolds number within the intricate vortex tube reactor system.

The knowledge garnered from this investigation forms a solid cornerstone for the development and enhancement of similar systems in various scientific and industrial applications. The predictive power of the partial least squares models, developed through design of experiments, promises to be a valuable resource for engineers and researchers seeking to anticipate mixing performance and Reynolds numbers within their own setups, thereby streamlining their design and optimization processes. Our optimized vortex tube reactor, as elucidated by the empirical findings, has showcased remarkable mixing capabilities, marked by a notably high mixing index and the presence of a transitional flow regime. This versatility in adjusting the flow rate widens the range of possible applications, and the passive mixing phenomenon, as harnessed through the residence time distribution function within our 3D printed vortex tube reactor, further augments its mixing efficiency. The implications of these discoveries cannot be overstated, as they point toward a promising new direction in the field of lipid-based nanoparticle synthesis.

Indeed, the novel 3D printed vortex tube reactor design, in tandem with the design of experiments methodology, holds immense potential for transformative advancements in particle size control, polydispersity index reduction, entrapment efficiency optimization, loading capacity augmentation, and overall productivity enhancement in the realm of lipid-based nanoparticle synthesis. In comparison to conventional methods, it has demonstrated clear superiority, opening doors to

improved processes and ultimately, more efficient and effective drug delivery systems.

Looking ahead, the potential for groundbreaking advancements in vortex tube reactor research becomes increasingly evident. The proposed future experiments should additionally observe other factors of the vortex tube reactor, including the wall roughness, the radius of curvature of vortex chamber, or other dimensions of the mixer and the reactor that might be affect mixing process. Leveraging computational fluid dynamics to intricately probe the heterogeneous phase of solvents, represent a pivotal step towards unraveling the complexities of mixing efficiency and mass transfer under the dynamic influence of non-laminar flow. This avenue of exploration holds the promise of not only enhancing our theoretical understanding but also fostering practical applications with wide-ranging implications. Delving deeper into the realm of residence time distribution, it becomes apparent that further investigations may necessitate specialized setups and alternative models. The alignment of these models with observed outcomes is crucial for providing a comprehensive and nuanced explanation of the reactor's behavior. As we move forward, the importance of refining our understanding of these fundamental aspects cannot be overstated, serving as the cornerstone for subsequent advancements. In the pursuit of heightened productivity, future studies could navigate the terrain of altering pump types, strategically aiming for the absolute zenith of efficiency. This entails a meticulous examination of the vortex tube reactor's durability, especially under challenging conditions characterized by high flow rates and pressure. The inclusion of materials like stainless steel grades 314 or 316, commonly employed in the pharmaceutical industry, adds a layer of practicality to the investigation, aligning theoretical advancements with real-world applicability. However, it is crucial to consider biological molecular conformation when high flow rate is used. Beyond the confines of material properties, the installation of in-line analysis emerges as a valuable consideration. This analytical tool, when integrated into the experimental framework, has the potential to unveil intricate details about the reactor's performance under varying conditions. Additionally, the introduction of controlled conditions, thoughtfully implemented, can further enrich our understanding by providing a controlled environment for studying the effects of changing conditions.

In closing, the horizon of possibilities extends beyond lipid-based nanoparticles. Our findings, shaped by a systematic approach to experimental design, can be leveraged and expanded upon in future studies involving other nanoparticle drug delivery systems, whether polymeric nanoparticles, inorganic nanoparticles, or solid-lipid nanoparticles. This underscores the potential for producing nanoparticles for vaccine or biopharmaceutical delivery. Our journey has not only deepened our understanding of vortex tube reactors but has also illuminated a path toward enhanced efficiency and efficacy in nanoparticle synthesis. The implications of these findings, combined with the power of experimental design, extend far beyond this research, fostering anticipation for innovations and breakthroughs. Notably, the reactor design forged through this study holds the potential for seamless adaptation into various nanoparticle synthesis. Our aspiration is that this labor, under the guiding influence of experimental design, may ignite further forays into the uncharted territories of these captivating fields of science and technology, fueling the relentless pursuit of new discoveries and revelations.

REFERENCES

1. Weissig V, Pettinger TK, Murdock N. Nanopharmaceuticals (part 1): products on the market. *International journal of nanomedicine*. 2014;4357-73.
2. Schoenmaker L, Witzigmann D, Kulkarni JA, Verbeke R, Kersten G, Jiskoot W, et al. mRNA-lipid nanoparticle COVID-19 vaccines: Structure and stability. *International journal of pharmaceutics*. 2021;601:120586.
3. Grossel SS. *Guidelines for Process Safety in Batch Reaction Systems*, (1999)-By Center for Chemical Process Safety, Center for Chemical Process Safety of the American Institute of Chemical Engineers, New York, NY, 171 pages, \$139.00. *Journal of Loss Prevention in the Process Industries*. 2001;4(14):330.
4. Aguillón AR, Bezerra MAdM, Gomez MR, de Souza RO. Continuous-flow chemistry toward sustainable chemical synthesis. *Green Sustainable Process for Chemical and Environmental Engineering and Science*: Elsevier; 2020. p. 49-69.
5. Missen RW, Missen RW, Mims CA, Saville BA. *Introduction to chemical reaction engineering and kinetics*: John Wiley & Sons Incorporated; 1999.
6. Neyt NC, Riley DL. Application of reactor engineering concepts in continuous flow chemistry: a review. *Reaction Chemistry & Engineering*. 2021;6(8):1295-326.
7. Rudyak V, Minakov A. Modeling and optimization of Y-type micromixers. *Micromachines*. 2014;5(4):886-912.
8. Le The H, Ta BQ, Le-Thanh H, Karlsen F, Nguyen-Thoi T, editors. A novel design of passive split and recombination micromixer with trapezoidal zigzag channels. *10th IEEE International Conference on Nano/Micro Engineered and Molecular Systems*; 2015: IEEE.
9. Mitchell MJ, Billingsley MM, Haley RM, Wechsler ME, Peppas NA, Langer R. Engineering precision nanoparticles for drug delivery. *Nature Reviews Drug Discovery*. 2021;20(2):101-24.
10. Kumari B. A Review on Nanoparticles: Their Preparation method and applications. *Ind Res J Pharm Sci*. 2018;5(2):1420.
11. Rivas CJM, Tarhini M, Badri W, Miladi K, Greige-Gerges H, Nazari QA, et al. Nanoprecipitation process: From encapsulation to drug delivery. *International journal of pharmaceutics*. 2017;532(1):66-81.

12. Desai KG. Chitosan nanoparticles prepared by ionotropic gelation: An overview of recent advances. *Critical Reviews™ in Therapeutic Drug Carrier Systems*. 2016;33(2).
13. Khan IU, Serra CA, Anton N, Vandamme TF. Production of nanoparticle drug delivery systems with microfluidics tools. *Expert opinion on drug delivery*. 2015;12(4):547-62.
14. Danhier F, Ansorena E, Silva JM, Coco R, Le Breton A, Pr at V. PLGA-based nanoparticles: an overview of biomedical applications. *Journal of controlled release*. 2012;161(2):505-22.
15. Semyari S, Azizi S, Kundu D, Boroumandmoghaddam A, Moniri M, Ebrahimifar M, et al. A Review of Poly Butyl Cyanoacrylate Nanoparticles as a Cancer Drug Delivery and Targeting. *Journal of Nanostructures*. 2021;11(4):754-71.
16. Akay C, Avukat E. Effect of nanoparticle addition on polymethylmethacrylate resins. *Acta Scientific Dental Sciences*. 2019;3(7):91-7.
17. Sangnim T, Dheer D, Jangra N, Huanbutta K, Puri V, Sharma A. Chitosan in Oral Drug Delivery Formulations: A Review. *Pharmaceutics*. 2023;15(9):2361.
18. Sinha V, Bansal K, Kaushik R, Kumria R, Trehan A. Poly- ϵ -caprolactone microspheres and nanospheres: an overview. *International journal of pharmaceutics*. 2004;278(1):1-23.
19. Moulay S. Poly (vinyl alcohol) functionalizations and applications. *Polymer-Plastics Technology and Engineering*. 2015;54(12):1289-319.
20. Das M, Shim KH, An SSA, Yi DK. Review on gold nanoparticles and their applications. *Toxicology and Environmental Health Sciences*. 2011;3:193-205.
21. Huber DL. Synthesis, properties, and applications of iron nanoparticles. *Small*. 2005;1(5):482-501.
22. Jeelani PG, Mulay P, Venkat R, Ramalingam C. Multifaceted application of silica nanoparticles. A review. *Silicon*. 2020;12:1337-54.
23. Probst CE, Zrazhevskiy P, Bagalkot V, Gao X. Quantum dots as a platform for nanoparticle drug delivery vehicle design. *Advanced drug delivery reviews*. 2013;65(5):703-18.
24. Paliwal R, Paliwal SR, Kenwat R, Kurmi BD, Sahu MK. Solid lipid

nanoparticles: A review on recent perspectives and patents. *Expert opinion on therapeutic patents*. 2020;30(3):179-94.

25. Sharma A, Baldi A. Nanostructured lipid carriers: A review. *Journal of Developing Drugs*. 2018;7(2):1-15.
26. Liu Y, Yang G, Jin S, Xu L, Zhao CX. Development of high-drug-loading nanoparticles. *ChemPlusChem*. 2020;85(9):2143-57.
27. Wang S, McGuirk CM, d'Aquino A, Mason JA, Mirkin CA. Metal–organic framework nanoparticles. *Advanced Materials*. 2018;30(37):1800202.
28. Hamidi M, Azadi A, Rafiei P. Hydrogel nanoparticles in drug delivery. *Advanced drug delivery reviews*. 2008;60(15):1638-49.
29. John E, Matschei T, Stephan D. Nucleation seeding with calcium silicate hydrate—A review. *Cement and Concrete Research*. 2018;113:74-85.
30. Bharti C, Nagaich U, Pal AK, Gulati N. Mesoporous silica nanoparticles in target drug delivery system: A review. *International journal of pharmaceutical investigation*. 2015;5(3):124.
31. Lara-Ochoa S, Ortega-Lara W, Guerrero-Beltrán CE. Hydroxyapatite nanoparticles in drug delivery: physicochemistry and applications. *Pharmaceutics*. 2021;13(10):1642.
32. Elzoghby AO, Samy WM, Elgindy NA. Protein-based nanocarriers as promising drug and gene delivery systems. *Journal of controlled release*. 2012;161(1):38-49.
33. Marasini N, Haque S, Kaminskas LM. Polymer-drug conjugates as inhalable drug delivery systems: A review. *Current Opinion in Colloid & Interface Science*. 2017;31:18-29.
34. Luo Y, Prestwich G. Cancer-targeted polymeric drugs. *Current Cancer Drug Targets*. 2002;2(3):209-26.
35. Hasan M, Leak RK, Stratford RE, Zlotos DP, Witt-Enderby PA. Drug conjugates—an emerging approach to treat breast cancer. *Pharmacology Research & Perspectives*. 2018;6(4):e00417.
36. Truong-Dinh Tran T, Ha-Lien Tran P, Tu Nguyen K, Tran V-T. Nano-precipitation: preparation and application in the field of pharmacy. *Current*

pharmaceutical design. 2016;22(20):2997-3006.

37. Britton J, Jamison TF. The assembly and use of continuous flow systems for chemical synthesis. *nature protocols*. 2017;12(11):2423-46.
38. Porta R, Benaglia M, Puglisi A. Flow chemistry: recent developments in the synthesis of pharmaceutical products. *Organic Process Research & Development*. 2016;20(1):2-25.
39. Britton J, Raston CL. Multi-step continuous-flow synthesis. *Chemical Society Reviews*. 2017;46(5):1250-71.
40. Movsisyan M, Delbeke E, Berton J, Battilocchio C, Ley S, Stevens C. Taming hazardous chemistry by continuous flow technology. *Chemical Society Reviews*. 2016;45(18):4892-928.
41. Trojanowicz M. Flow chemistry vs. flow analysis. *Talanta*. 2016;146:621-40.
42. Noël T, Su Y, Hessel V. Beyond organometallic flow chemistry: the principles behind the use of continuous-flow reactors for synthesis. *Organometallic Flow Chemistry*. 2016:1-41.
43. Garciadiego-Ortega E, Tsaoulidis D, Pineda M, Fraga ES, Angeli P. Hydrodynamics and mass transfer in segmented flow small channel contactors for uranium extraction. *Chemical Engineering and Processing-Process Intensification*. 2020;153:107921.
44. Durst F, Arnold I. *Fluid mechanics: an introduction to the theory of fluid flows*: Springer; 2008.
45. Saliba J, Daou A, Damiati S, Saliba J, El-Sabban M, Mhanna R. Development of microplatforms to mimic the in vivo architecture of CNS and PNS physiology and their diseases. *Genes*. 2018;9(6):285.
46. Plutschack MB, Pieber Bu, Gilmore K, Seeberger PH. The hitchhiker's guide to flow chemistry||. *Chemical reviews*. 2017;117(18):11796-893.
47. Mallia CJ, Baxendale IR. The use of gases in flow synthesis. *Organic Process Research & Development*. 2016;20(2):327-60.
48. Suter SP, Skalak R. The history of Poiseuille's law. *Annual review of fluid mechanics*. 1993;25(1):1-20.
49. Malet-Sanz L, Susanne F. Continuous flow synthesis. A pharma perspective.

Journal of medicinal chemistry. 2012;55(9):4062-98.

50. Roffo F, Ponsiglione AM, Netti PA, Torino E. coupled Hydrodynamic Flow Focusing (cHFF) to Engineer Lipid–Polymer Nanoparticles (LiPoNs) for Multimodal Imaging and Theranostic Applications. *Biomedicines*. 2022;10(2):438.
51. Pal S, Besenhard MO, Storozhuk L, Lees MR, Thanh NTK, Gavriilidis A. Self-seeded coprecipitation flow synthesis of iron oxide nanoparticles via triphasic reactor platform: Optimising heating performance under alternating magnetic fields. *Chemical Engineering Journal*. 2023;462:142007.
52. Kim S, Wang H, Yan L, Zhang X, Cheng Y. Continuous preparation of itraconazole nanoparticles using droplet-based microreactor. *Chemical Engineering Journal*. 2020;393:124721.
53. Galant O, Donmez HB, Barner-Kowollik C, Diesendruck CE. Flow photochemistry for single-chain polymer nanoparticle synthesis. *Angewandte Chemie*. 2021;133(4):2070-4.
54. Gu T, Zheng C, He F, Zhang Y, Khan SA, Hatton TA. Electrically controlled mass transport into microfluidic droplets from nanodroplet carriers with application in controlled nanoparticle flow synthesis. *Lab on a Chip*. 2018;18(9):1330-40.
55. Karan D, Khan SA. Mesoscale triphasic flow reactors for metal catalyzed gas–liquid reactions. *Reaction Chemistry & Engineering*. 2019;4(7):1331-40.
56. Operti MC, Bernhardt A, Sincari V, Jager E, Grimm S, Engel A, et al. Industrial scale manufacturing and downstream processing of PLGA-based nanomedicines suitable for fully continuous operation. *Pharmaceutics*. 2022;14(2):276.
57. Tai S, Zhang W, Zhang J, Luo G, Jia Y, Deng M, et al. Facile preparation of UiO-66 nanoparticles with tunable sizes in a continuous flow microreactor and its application in drug delivery. *Microporous and Mesoporous Materials*. 2016;220:148-54.
58. Bayazit MK, Yue J, Cao E, Gavriilidis A, Tang J. Controllable synthesis of gold nanoparticles in aqueous solution by microwave assisted flow chemistry. *ACS Sustainable Chemistry & Engineering*. 2016;4(12):6435-42.
59. Hu HH. Computational fluid dynamics. *Fluid mechanics: Elsevier*; 2012. p. 421-72.
60. Zawawi MH, Saleha A, Salwa A, Hassan N, Zahari NM, Ramli MZ, et al.,

editors. A review: Fundamentals of computational fluid dynamics (CFD). AIP conference proceedings; 2018: AIP Publishing.

61. Peymani FY, Liu Y, Hayatdavoudi A. CFD simulation and validation of phase particle entrapment. *International Journal for Computational Methods in Engineering Science and Mechanics*. 2014;15(5):438-47.
62. Alfonsi G. Reynolds-averaged Navier–Stokes equations for turbulence modeling. *Applied Mechanics Reviews*. 2009;62(4).
63. Launder BE, Spalding DB. The numerical computation of turbulent flows. *Numerical prediction of flow, heat transfer, turbulence and combustion*: Elsevier; 1983. p. 96-116.
64. Gullberg R. *Computational Fluid Dynamics in OpenFOAM: Mesh Generation and Quality*. Dostopno na: [http://folk.ntnu.no/preisig/HAP_Specials ...](http://folk.ntnu.no/preisig/HAP_Specials...); 2017.
65. Matsson JE. *An Introduction to SolidWorks Flow Simulation 2013*: SDC publications; 2013.
66. Zhang J, Amini N, Morton DA, Hapgood KP. 3D printing with particles as feedstock materials. *Advanced Powder Technology*. 2021;32(9):3324-45.
67. Piedra-Cascón W, Krishnamurthy VR, Att W, Revilla-León M. 3D printing parameters, supporting structures, slicing, and post-processing procedures of vat-polymerization additive manufacturing technologies: A narrative review. *Journal of Dentistry*. 2021;109:103630.
68. Goh GD, Yap YL, Tan H, Sing SL, Goh GL, Yeong WY. Process–structure–properties in polymer additive manufacturing via material extrusion: A review. *Critical Reviews in Solid State and Materials Sciences*. 2020;45(2):113-33.
69. Tyagi S, Yadav A, Deshmukh S. Review on mechanical characterization of 3D printed parts created using material jetting process. *Materials Today: Proceedings*. 2022;51:1012-6.
70. Ziaee M, Crane NB. Binder jetting: A review of process, materials, and methods. *Additive Manufacturing*. 2019;28:781-801.
71. Singh DD, Mahender T, Reddy AR. Powder bed fusion process: A brief review. *Materials Today: Proceedings*. 2021;46:350-5.
72. Ahn D-G. Directed energy deposition (DED) process: State of the art.

International Journal of Precision Engineering and Manufacturing-Green Technology. 2021;8:703-42.

73. Reddy BY, Siddhartha M, Reddy PSR, Lakshmi AA, editors. Influence of Process Parameters on Sheet Lamination Method-based 3D printing: A Review. E3S Web of Conferences; 2023: EDP Sciences.
74. Kouadri A, Douroum E, Lasbet Y, Naas TT, Khelladi S, Makhlof M. Comparative study of mixing behaviors using non-Newtonian fluid flows in passive micromixers. International Journal of Mechanical Sciences. 2021;201:106472.
75. Plouffe P, Roberge DM, Macchi A. Liquid–liquid flow regimes and mass transfer in various micro-reactors. Chemical Engineering Journal. 2016;300:9-19.
76. El-Batsh HM. Improving cyclone performance by proper selection of the exit pipe. Applied mathematical modelling. 2013;37(7):5286-303.
77. Overcamp TJ, Scarlett SE. Effect of Reynolds number on the Stokes number of cyclones. Aerosol science and technology. 1993;19(3):362-70.
78. Goswami R, O’Hagan DT, Adamo R, Baudner BC. Conjugation of mannans to enhance the potency of liposome nanoparticles for the delivery of RNA vaccines. Pharmaceutics. 2021;13(2):240.
79. Becker JM, Caldwell GA, Zachgo EA. Biotechnology: a laboratory course: Academic Press; 1996.
80. Khalde CM, Ramanan V, Sangwai JS, Ranade VV. Passive mixer cum reactor using threaded inserts: investigations of flow, mixing, and heat transfer characteristics. Industrial & Engineering Chemistry Research. 2019;59(9):3943-61.
81. Hossain S, Kim K-Y. Mixing performance of a serpentine micromixer with non-aligned inputs. Micromachines. 2015;6(7):842-54.
82. Kim K, Shah I, Ali M, Aziz S, Khalid MAU, Kim YS, et al. Experimental and numerical analysis of three Y-shaped split and recombination micromixers based on cantor fractal structures. Microsystem Technologies. 2020;26:1783-96.
83. White FM. Fluid mechanics 1966.
84. Ferziger JH, Perić M, Street RL. Computational methods for fluid dynamics: Springer; 2002.
85. Madana VST, Ashraf Ali B. Numerical investigation of engulfment flow at

low Reynolds numbers in a T-shaped microchannel. *Physics of Fluids*.

2020;32(7):072005.

86. Missen RW. *Introduction to chemical reaction engineering and kinetics*: John Wiley & Sons; 1928.

87. Zhang H-X, Wang J-X, Shao L, Chen J-F. Microfluidic fabrication of monodispersed pharmaceutical colloidal spheres of atorvastatin calcium with tunable sizes. *Industrial & engineering chemistry research*. 2010;49(9):4156-61.

88. Roces CB, Christensen D, Perrie Y. Translating the fabrication of protein-loaded poly (lactic-co-glycolic acid) nanoparticles from bench to scale-independent production using microfluidics. *Drug delivery and translational research*. 2020;10:582-93.

89. Mesquita PC, dos Santos-Silva E, Streck L, Damasceno IZ, Maia AMS, Fernandes-Pedrosa MF, et al. Cationic functionalized biocompatible polylactide nanoparticles for slow release of proteins. *Colloids and Surfaces A: Physicochemical and Engineering Aspects*. 2017;513:442-51.

90. Kašpar O, Koyuncu A, Hubatová-Vacková A, Balouch M, Tokárová V. Influence of channel height on mixing efficiency and synthesis of iron oxide nanoparticles using droplet-based microfluidics. *RSC advances*. 2020;10(26):15179-89.

91. Hernández-Giottonini KY, Rodríguez-Córdova RJ, Gutiérrez-Valenzuela CA, Peñuñuri-Miranda O, Zavala-Rivera P, Guerrero-Germán P, et al. PLGA nanoparticle preparations by emulsification and nanoprecipitation techniques: Effects of formulation parameters. *Rsc Advances*. 2020;10(8):4218-31.

92. Tucci S, Seo J, Kakwere H, Kheiolomoom A, Ingham E, Mahakian L, et al. A scalable method for squalenoylation and assembly of multifunctional ⁶⁴Cu-Labeled squalenoylated gemcitabine nanoparticles. *Nanotheranostics*, 2018, 2 (4), 387-402.

93. Bal V, Bandyopadhyaya R. Mechanistic aspects in the formation of nano-and submicron particles in a batch and a continuous microfluidic reactor: Experiment, modeling and simulation. *Chemical Engineering Journal*. 2019;371:43-54.

94. Yanar F, Mosayyebi A, Nastruzzi C, Carugo D, Zhang X. Continuous-flow production of liposomes with a millireactor under varying fluidic conditions. *Pharmaceutics*. 2020;12(11):1001.

95. Makino K, Yamada T, Kimura M, Oka T, Ohshima H, Kondo T. Temperature- and ionic strength-induced conformational changes in the lipid head group region of liposomes as suggested by zeta potential data. *Biophysical chemistry*. 1991;41(2):175-83.
96. Wiącek AE. Influence of dipalmitoylphosphatidylcholine (or dioleoylphosphatidylcholine) and phospholipase A2 enzyme on the properties of emulsions. *Journal of colloid and interface science*. 2012;373(1):75-83.
97. Desai D, Guerrero YA, Balachandran V, Morton A, Lyon L, Larkin B, et al. Towards a microfluidics platform for the continuous manufacture of organic and inorganic nanoparticles. *Nanomedicine: Nanotechnology, Biology and Medicine*. 2021;35:102402.
98. Fan H, Striolo A. Nanoparticle effects on the water-oil interfacial tension. *Physical Review E*. 2012;86(5):051610.
99. Albisa A, Piacentini E, Sebastian V, Arruebo M, Santamaria J, Giorno L. Preparation of drug-loaded PLGA-PEG nanoparticles by membrane-assisted nanoprecipitation. *Pharmaceutical Research*. 2017;34:1296-308.
100. Długosz O, Banach M. Continuous production of silver nanoparticles and process control. *Journal of Cluster Science*. 2019;30:541-52.

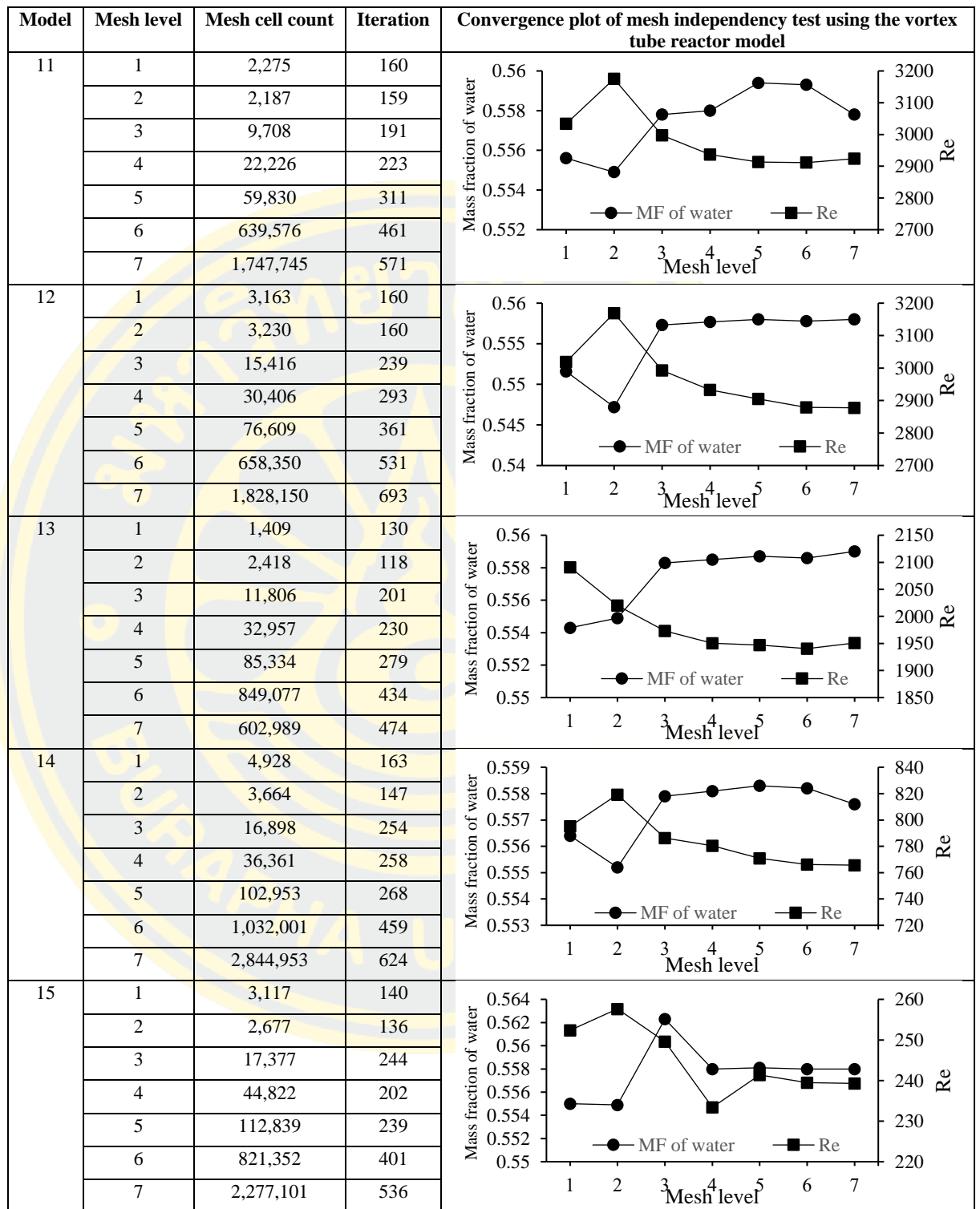


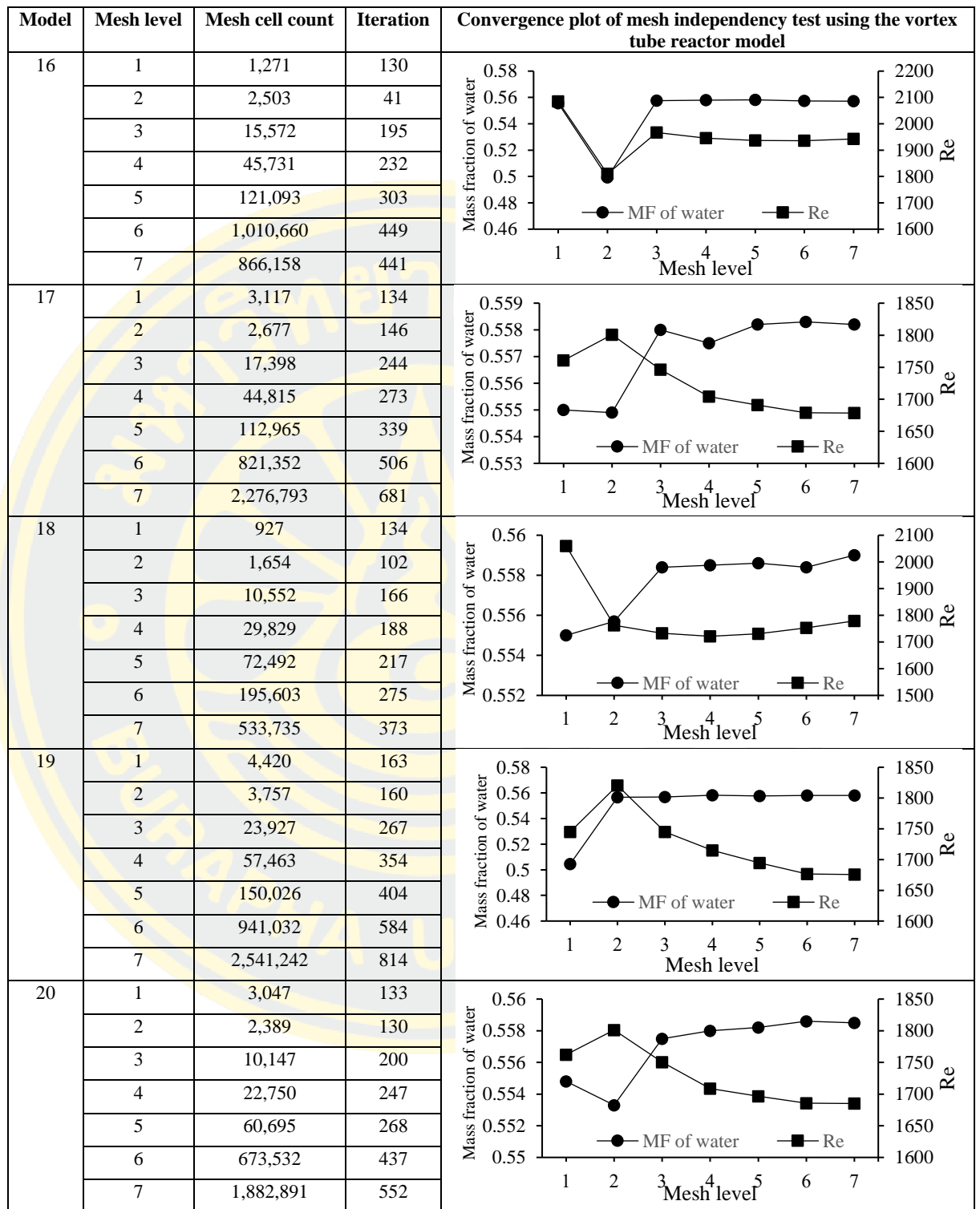
APPENDIX

Appendix Table 1. Mesh independence test using the vortex tube reactor model.

Model	Mesh level	Mesh cell count	Iteration	Convergence plot of mesh independency test using the vortex tube reactor model
1	1	3,268	160	
	2	3,558	160	
	3	24,010	268	
	4	48,429	300	
	5	122,228	351	
	6	817,569	521	
	7	2,236,753	695	
2	1	3,117	127	
	2	2,677	141	
	3	17,398	216	
	4	44,850	261	
	5	112,741	320	
	6	821,352	508	
	7	2,276,391	676	
3	1	3,163	160	
	2	3,320	160	
	3	15,409	239	
	4	30,693	246	
	5	76,805	283	
	6	658,343	447	
	7	1,828,178	620	
4	1	3,117	126	
	2	2,677	146	
	3	17,377	217	
	4	44,878	262	
	5	112,391	319	
	6	821,325	508	
	7	2,276,856	676	
5	1	2,335	160	
	2	2,435	148	
	3	14,856	195	
	4	34,843	222	
	5	90,903	261	
	6	133,316	437	
	7	1,997,191	598	

Model	Mesh level	Mesh cell count	Iteration	Convergence plot of mesh independency test using the vortex tube reactor model
6	1	1,409	58	
	2	2,418	116	
	3	11,806	184	
	4	32,957	201	
	5	85,334	226	
	6	849,119	383	
	7	603,021	363	
7	1	5,039	145	
	2	3,664	144	
	3	16,898	228	
	4	36,375	260	
	5	102,972	310	
	6	1,031,558	488	
	7	2,843,638	651	
8	1	5,498	167	
	2	3,687	160	
	3	23,934	276	
	4	53,093	292	
	5	156,980	301	
	6	1,428,243	526	
	7	3,882,523	696	
9	1	1,425	134	
	2	2,591	123	
	3	15,666	200	
	4	45,878	220	
	5	120,732	248	
	6	1,010,688	419	
	7	884,499	414	
10	1	3,117	136	
	2	2,677	160	
	3	17,377	244	
	4	44,822	328	
	5	113,014	389	
	6	821,352	534	
	7	2,276,551	823	





Model	Mesh level	Mesh cell count	Iteration	Convergence plot of mesh independency test using the vortex tube reactor model
21	1	3,117	131	
	2	2,677	143	
	3	17,398	244	
	4	44,822	280	
	5	112,741	342	
	6	821,366	506	
	7	2,277,094	680	
22	1	3,258	160	
	2	3,558	160	
	3	23,821	267	
	4	48,992	335	
	5	122,312	452	
	6	817,667	636	
	7	2,236,669	867	
23	1	2,335	160	
	2	2,435	160	
	3	14,835	230	
	4	34,836	270	
	5	90,896	331	
	6	733,085	518	
	7	1,997,415	670	
24	1	1,446	135	
	2	3,138	114	
	3	15,544	210	
	4	35,977	236	
	5	101,130	262	
	6	276,519	307	
	7	750,381	395	
25	1	2,275	158	
	2	2,187	147	
	3	9,729	201	
	4	22,184	209	
	5	59,858	237	
	6	639,597	381	
	7	1,747,738	520	

Model	Mesh level	Mesh cell count	Iteration	Convergence plot of mesh independency test using the vortex tube reactor model
26	1	5,387	164	
	2	3,687	160	
	3	23,934	276	
	4	53,100	326	
	5	156,961	366	
	6	1,427,656	580	
	7	3,879,258	786	
27	1	3,187	137	
	2	2,890	147	
	3	24,677	268	
	4	66,594	312	
	5	170,598	378	
	6	1,013,285	557	
	7	2,784,134	765	
28	1	2,603	160	
	2	2,263	160	
	3	12,410	225	
	4	27,077	297	
	5	70,760	393	
	6	630,716	624	
	7	1,673,348	817	
29	1	3,117	129	
	2	2,677	153	
	3	17,377	244	
	4	44,850	274	
	5	112,363	340	
	6	821,352	506	
	7	2,277,087	681	
30	1	3,117	132	
	2	2,677	152	
	3	17,377	240	
	4	44,850	274	
	5	112,650	343	
	6	821,086	506	
	7	2,276,912	681	

Appendix Table 2 CFD result of mass fraction at the outlet of a vortex tube reactor.

Run	Cross section length at the end point	Mass fraction of water	MF-Bar	SD	Max SD	Mixing index	Plot of mass fraction evolutions along the midline at the exit
1	0.00000	0.55956	0.55851	0.00219	0.49656	0.99559	
	0.11489	0.55957					
	0.25986	0.55961					
	0.45315	0.55977					
	0.64645	0.56012					
	0.83974	0.56067					
	1.03304	0.56110					
	1.22633	0.56148					
	1.61292	0.56114					
	2.00000	0.55907					
	2.38610	0.55679					
	2.77270	0.55581					
	3.15929	0.55579					
	3.35258	0.55596					
	3.54588	0.55608					
3.73917	0.55611						
4.00000	0.55605						
2	0.00000	0.55547	0.55773	0.00107	0.49666	0.99785	
	0.11639	0.55552					
	0.28759	0.55601					
	0.45879	0.55691					
	0.62998	0.55774					
	0.91531	0.55831					
	0.97238	0.55842					
	1.31478	0.55864					
	1.65717	0.55862					
	2.00000	0.55854					
	2.34197	0.55839					
	2.68436	0.55811					
	3.02676	0.55790					
	3.36916	0.55794					
	3.71155	0.55828					
3.88275	0.55830						
4.00000	0.55829						
3	0.00000	0.55494	0.55771	0.00208	0.49666	0.99582	
	0.06656	0.55497					
	0.25986	0.55527					
	0.45315	0.55600					
	0.64645	0.55725					
	0.83974	0.55864					
	1.03304	0.55935					
	1.22633	0.56002					
	1.61292	0.55939					
	2.00000	0.55725					
	2.38610	0.55546					
	2.77270	0.55538					
	2.96599	0.55612					
	3.15929	0.55691					
	3.35258	0.55834					
3.54588	0.55969						
3.73917	0.56043						
3.93247	0.56055						
4.00000	0.56053						

Run	Cross section length at the end point	Mass fraction of water	MF-Bar	SD	Max SD	Mixing index	Plot of mass fraction evolutions along the midline at the exit
4	0.00000	0.55549	0.55776	0.00103	0.49665	0.99792	
	0.11639	0.55555					
	0.28759	0.55603					
	0.45879	0.55693					
	0.62998	0.55775					
	0.91531	0.55830					
	0.97238	0.55841					
	1.31478	0.55862					
	1.65717	0.55859					
	2.00000	0.55851					
	2.34197	0.55836					
	2.68436	0.55810					
	3.02676	0.55790					
	3.36916	0.55796					
	3.58315	0.55819					
5	0.00000	0.55824	0.55767	0.00358	0.49666	0.99279	
	0.17792	0.55829					
	0.34360	0.55803					
	0.50928	0.55745					
	0.67496	0.55670					
	1.00633	0.55465					
	1.33769	0.55349					
	1.66905	0.55505					
	2.00000	0.55949					
	2.33178	0.56390					
	2.66314	0.56500					
	2.99451	0.56230					
	3.32587	0.55786					
	3.65723	0.55466					
	3.82291	0.55386					
4.00000	0.55368						
6	0.00000	0.55939	0.55725	0.00565	0.49671	0.98863	
	0.06131	0.55939					
	0.21041	0.55935					
	0.50861	0.55888					
	0.80682	0.55809					
	1.10502	0.55773					
	1.40322	0.55846					
	1.70142	0.56044					
	2.00000	0.56301					
	2.29783	0.56491					
	2.59603	0.56493					
	2.89423	0.56245					
	3.19243	0.55744					
	3.49064	0.55171					
	3.63974	0.55010					
3.78884	0.54842						
3.93794	0.54789						
4.00000	0.54787						

Run	Cross section length at the end point	Mass fraction of water	MF-Bar	SD	Max SD	Mixing index	Plot of mass fraction evolutions along the midline at the exit
7	0.00000	0.55798	0.55738	0.00056	0.49670	0.99887	
	0.04854	0.55800					
	0.21120	0.55813					
	0.37385	0.55818					
	0.53651	0.55817					
	0.69916	0.55804					
	0.89435	0.55782					
	1.34979	0.55730					
	1.67510	0.55707					
	2.00000	0.55702					
	2.00041	0.55702					
	2.65103	0.55731					
	2.97634	0.55729					
	3.30165	0.55709					
	3.46431	0.55695					
8	0.00000	0.55174	0.55834	0.00682	0.49658	0.98627	
	0.21120	0.55175					
	0.37385	0.55165					
	0.53651	0.55144					
	0.69916	0.55112					
	1.02447	0.55067					
	1.34979	0.55092					
	1.67510	0.55314					
	2.00000	0.55833					
	2.32572	0.56348					
	2.65103	0.56564					
	2.97634	0.56588					
	3.35587	0.56545					
	3.57275	0.56529					
	3.68119	0.56519					
3.78962	0.56507						
4.00000	0.56498						
9	0.00000	0.55717	0.55861	0.00504	0.49655	0.98986	
	0.06206	0.55719					
	0.21116	0.55747					
	0.50936	0.55913					
	0.80757	0.56225					
	1.10577	0.56458					
	1.40397	0.56405					
	1.70217	0.56309					
	2.00000	0.56488					
	2.29858	0.56564					
	2.59678	0.56093					
	2.89498	0.55448					
	3.19318	0.55172					
	3.49139	0.55168					
	3.78959	0.55176					
4.00000	0.55169						

Run	Cross section length at the end point	Mass fraction of water	MF-Bar	SD	Max SD	Mixing index	Plot of mass fraction evolutions along the midline at the exit
10	0.00000	0.55808	0.55839	0.00015	0.49658	0.99971	
	0.11725	0.55812					
	0.28845	0.55823					
	0.45965	0.55830					
	0.63084	0.55837					
	0.85911	0.55843					
	0.97324	0.55846					
	1.31564	0.55852					
	1.65803	0.55858					
	2.00000	0.55859					
	2.00043	0.55859					
	2.34283	0.55852					
	2.68522	0.55845					
	3.02762	0.55841					
	3.37002	0.55839					
	3.54121	0.55837					
3.71241	0.55835						
3.88361	0.55832						
4.00000	0.55831						
11	0.00000	0.55925	0.55924	0.00022	0.49648	0.99955	
	0.01224	0.55926					
	0.17792	0.55941					
	0.34360	0.55950					
	0.50928	0.55952					
	0.67496	0.55954					
	1.00633	0.55950					
	1.33769	0.55939					
	1.66905	0.55932					
	2.00000	0.55930					
	2.33178	0.55927					
	2.66314	0.55921					
	2.99451	0.55917					
	3.32587	0.55918					
	3.49155	0.55917					
	3.65723	0.55913					
3.82291	0.55898						
3.98860	0.55877						
4.00000	0.55876						
12	0.00000	0.55760	0.55783	0.00015	0.49664	0.99969	
	0.06753	0.55761					
	0.26083	0.55769					
	0.45412	0.55777					
	0.64742	0.55783					
	0.84071	0.55790					
	1.03401	0.55794					
	1.22730	0.55798					
	1.61390	0.55801					
	2.00000	0.55802					
	2.00049	0.55802					
	2.38708	0.55800					
	2.77367	0.55795					
	3.16026	0.55786					
	3.35355	0.55781					
	3.54685	0.55776					
3.74014	0.55771						
3.93344	0.55763						
4.00000	0.55762						

Run	Cross section length at the end point	Mass fraction of water	MF-Bar	SD	Max SD	Mixing index	Plot of mass fraction evolutions along the midline at the exit
13	0.00000	0.55834	0.55851	0.00010	0.49657	0.99980	
	0.06206	0.55838					
	0.21116	0.55856					
	0.36026	0.55862					
	0.50936	0.55867					
	0.80757	0.55867					
	1.10577	0.55862					
	1.40397	0.55854					
	1.70217	0.55848					
	2.00000	0.55847					
	2.00037	0.55847					
	2.44768	0.55852					
	2.59678	0.55854					
	2.89498	0.55856					
	3.19318	0.55856					
	3.49139	0.55852					
	3.64049	0.55848					
3.78959	0.55844						
3.93869	0.55837						
4.00000	0.55836						
14	0.00000	0.55921	0.55862	0.00283	0.49655	0.99430	
	0.04854	0.55922					
	0.21120	0.55941					
	0.37385	0.56002					
	0.53651	0.56108					
	0.69916	0.56228					
	1.02447	0.56361					
	1.34979	0.56315					
	1.75632	0.56052					
	2.00000	0.55891					
	2.40705	0.55594					
	2.65103	0.55418					
	2.97634	0.55361					
	3.30165	0.55515					
	3.46431	0.55633					
	3.62697	0.55735					
	3.78962	0.55792					
3.95228	0.55799						
4.00000	0.55799						
15	0.00000	0.58678	0.55629	0.02615	0.49682	0.94736	
	0.45879	0.58693					
	0.62998	0.58681					
	0.85825	0.58571					
	0.97238	0.58523					
	1.31478	0.58120					
	1.65717	0.57249					
	2.00000	0.55842					
	2.34197	0.54432					
	2.68436	0.53540					
	3.02676	0.53110					
	3.31209	0.52965					
	3.36916	0.52933					
	3.58315	0.52909					
	3.71155	0.52908					
4.00000	0.52913						

Run	Cross section length at the end point	Mass fraction of water	MF-Bar	SD	Max SD	Mixing index	Plot of mass fraction evolutions along the midline at the exit
16	0.00000	0.55502	0.55739	0.00133	0.49670	0.99732	
	0.06131	0.55506					
	0.21041	0.55547					
	0.35951	0.55602					
	0.50861	0.55651					
	0.80682	0.55768					
	1.10502	0.55855					
	1.40322	0.55893					
	1.70142	0.55892					
	2.00000	0.55857					
	2.29783	0.55804					
	2.59603	0.55771					
	2.89423	0.55777					
	3.19243	0.55797					
	3.49064	0.55803					
17	0.00000	0.55938	0.55857	0.00059	0.49656	0.99881	
	0.11725	0.55938					
	0.28845	0.55929					
	0.45965	0.55903					
	0.63084	0.55874					
	0.80204	0.55855					
	0.97324	0.55838					
	1.31564	0.55825					
	1.65803	0.55835					
	2.00000	0.55851					
	2.34283	0.55869					
	2.68522	0.55878					
	3.02762	0.55858					
	3.31295	0.55814					
	3.37002	0.55804					
3.71241	0.55700						
3.88361	0.55671						
4.00000	0.55667						
18	0.00000	0.55623	0.55860	0.00127	0.49655	0.99744	
	0.23947	0.55624					
	0.53296	0.55677					
	0.82644	0.55785					
	1.11992	0.55871					
	1.41340	0.55917					
	1.70689	0.55940					
	2.00000	0.55935					
	2.29385	0.55896					
	2.58733	0.55861					
	2.88082	0.55871					
	3.17430	0.55912					
	3.46778	0.55967					
	3.76126	0.56005					
	4.00000	0.56011					

Run	Cross section length at the end point	Mass fraction of water	MF-Bar	SD	Max SD	Mixing index	Plot of mass fraction evolutions along the midline at the exit
19	0.00000	0.55498	0.55806	0.00183	0.49662	0.99631	
	0.13191	0.55501					
	0.31868	0.55525					
	0.50544	0.55581					
	0.69220	0.55663					
	0.87896	0.55740					
	1.10307	0.55792					
	1.25248	0.55825					
	1.62601	0.55848					
	2.00000	0.55810					
	2.37305	0.55788					
	2.74658	0.55831					
	2.97069	0.55881					
	3.12010	0.55915					
	3.30686	0.55975					
20	0.00000	0.55945	0.55854	0.00054	0.49656	0.99892	
	0.11639	0.55947					
	0.28759	0.55943					
	0.45879	0.55923					
	0.62998	0.55900					
	0.80118	0.55884					
	0.97238	0.55869					
	1.31478	0.55835					
	1.65717	0.55805					
	1.99957	0.55793					
	2.00000	0.55793					
	2.34197	0.55799					
	2.68436	0.55816					
	3.02676	0.55829					
	3.36916	0.55833					
3.54035	0.55833						
21	0.00000	0.55666	0.55839	0.00083	0.49658	0.99833	
	0.11639	0.55670					
	0.28759	0.55699					
	0.62998	0.55805					
	0.91531	0.55850					
	0.97238	0.55859					
	1.31478	0.55879					
	1.65717	0.55870					
	2.00000	0.55852					
	2.34197	0.55836					
	2.68436	0.55826					
	3.02676	0.55839					
	3.19796	0.55856					
	3.36916	0.55875					
	3.54035	0.55904					
3.71155	0.55930						
3.88275	0.55939						
4.00000	0.55939						

Run	Cross section length at the end point	Mass fraction of water	MF-Bar	SD	Max SD	Mixing index	Plot of mass fraction evolutions along the midline at the exit
22	0.00000	0.55804	0.55803	0.00015	0.49662	0.99969	
	0.06753	0.55806					
	0.26083	0.55814					
	0.45412	0.55812					
	0.64742	0.55805					
	0.84071	0.55803					
	1.22730	0.55805					
	1.61390	0.55807					
	2.00000	0.55810					
	2.77367	0.55819					
	3.16026	0.55818					
	3.35355	0.55813					
	3.54685	0.55801					
	3.74014	0.55786					
3.93344	0.55770						
4.00000	0.55768						
23	0.00000	0.55857	0.55871	0.00008	0.49654	0.99984	
	0.01224	0.55858					
	0.17792	0.55866					
	0.34360	0.55871					
	0.50928	0.55873					
	0.67496	0.55875					
	1.00633	0.55877					
	1.33769	0.55877					
	1.66905	0.55877					
	2.00000	0.55876					
	2.33178	0.55876					
	2.74598	0.55877					
	2.99451	0.55877					
	3.32587	0.55876					
3.49155	0.55875						
3.65723	0.55873						
3.82291	0.55868						
3.98860	0.55857						
4.00000	0.55856						
24	0.00000	0.58345	0.55692	0.01650	0.49675	0.96679	
	0.27408	0.58260					
	0.55695	0.57839					
	0.83982	0.57086					
	1.12269	0.56240					
	1.40556	0.55525					
	1.68843	0.55339					
	1.97129	0.55776					
	2.00000	0.55829					
	2.25416	0.56302					
	2.53703	0.56297					
	2.81990	0.55597					
	3.10277	0.54673					
	3.38563	0.53902					
3.66850	0.53389						
3.95137	0.53187						
4.00000	0.53179						

Run	Cross section length at the end point	Mass fraction of water	MF-Bar	SD	Max SD	Mixing index	Plot of mass fraction evolutions along the midline at the exit
25	0.00000	0.55595	0.55869	0.00240	0.49654	0.99516	
	0.17792	0.55597					
	0.34360	0.55595					
	0.56451	0.55605					
	0.67496	0.55611					
	1.00633	0.55650					
	1.33769	0.55715					
	1.75179	0.55783					
	2.00000	0.55822					
	2.33178	0.55905					
	2.66314	0.56019					
	2.99451	0.56114					
	3.32587	0.56154					
	3.54678	0.56158					
26	0.00000	0.55927	0.55840	0.00088	0.49658	0.99823	
	0.04854	0.55928					
	0.21120	0.55944					
	0.37385	0.55962					
	0.53651	0.55970					
	0.69916	0.55955					
	0.89435	0.55919					
	1.10580	0.55881					
	1.34979	0.55836					
	1.67510	0.55800					
	2.00000	0.55800					
	2.00041	0.55800					
	2.32572	0.55816					
	2.65103	0.55812					
2.97634	0.55781						
27	0.00000	0.55555	0.55851	0.00215	0.49656	0.99567	
	0.11639	0.55557					
	0.28759	0.55565					
	0.45879	0.55581					
	0.62998	0.55612					
	0.80118	0.55652					
	0.97238	0.55687					
	1.31478	0.55774					
	1.65717	0.55855					
	2.00000	0.55901					
	2.34197	0.55932					
	2.68436	0.55984					
	3.02676	0.56045					
	3.19796	0.56064					
3.36916	0.56086						
3.54035	0.56090						
3.79715	0.56079						
3.88275	0.56075						
4.00000	0.56072						

Run	Cross section length at the end point	Mass fraction of water	MF-Bar	SD	Max SD	Mixing index	Plot of mass fraction evolutions along the midline at the exit
28	0.00000	0.55938	0.55811	0.00096	0.49661	0.99807	
	0.19947	0.55942					
	0.33794	0.55946					
	0.52256	0.55941					
	0.70718	0.55923					
	0.89180	0.55899					
	1.07643	0.55871					
	1.26105	0.55845					
	1.63029	0.55780					
	2.00000	0.55746					
	2.36878	0.55733					
	2.79957	0.55712					
	2.92265	0.55706					
	3.10727	0.55692					
	3.29189	0.55697					
29	0.00000	0.55939	0.55837	0.00082	0.49658	0.99834	
	0.11725	0.55940					
	0.28845	0.55931					
	0.45965	0.55904					
	0.63084	0.55875					
	0.80204	0.55856					
	0.97324	0.55839					
	1.31564	0.55826					
	1.65803	0.55835					
	2.00000	0.55851					
	2.34283	0.55869					
	2.68522	0.55879					
	3.02762	0.55859					
	3.31295	0.55814					
	3.37002	0.55805					
3.71241	0.55701						
30	0.00000	0.55936	0.55836	0.00082	0.49658	0.99834	
	0.11725	0.55937					
	0.28845	0.55928					
	0.45965	0.55903					
	0.63084	0.55874					
	0.80204	0.55855					
	0.97324	0.55839					
	1.31564	0.55826					
	1.65803	0.55836					
	2.00000	0.55852					
	2.34283	0.55870					
	2.68522	0.55879					
	3.02762	0.55859					
	3.31295	0.55814					
	3.37002	0.55805					
3.71241	0.55699						
3.88361	0.55671						
4.00000	0.55666						

Appendix: Control chart calculation for X-chart and MR-chart (MR method)

In this appendix, we will outline the calculations and steps involved in creating X-charts and MR-charts using the Moving Range (MR) method for control purposes. These control charts are commonly employed in quality control and process improvement to monitor the stability and variability of processes.

Calculate the subgroup average (\bar{X})

To compute the Subgroup Average (X-bar), follow this formula for each subgroup:

$$\bar{X} = \frac{1}{n} \sum_{i=1}^n X_i$$

where; \bar{X} is the sample mean,

n is the number of data points in the sample,

X_i is the value of the element at the i -th position.

Calculation of moving range (MR)

For each subgroup, determine the Moving Range (MR) using this formula:

$$MR = |X_i - X_{i-1}|$$

Calculate the average of moving range (\overline{MR})

Calculate the average of the moving ranges (MR-bar) across all subgroups using the formula:

$$\overline{MR} = \frac{1}{n-1} \sum_{i=1}^n |X_i - X_{i-1}|$$

Determining control limits for the X-chart

To establish the control limits for the X-chart, follow these steps:

Upper control limit (UCL)

$$UCL = \bar{X} + \frac{3\overline{MR}}{d_2}$$

Control limit (CL)

$$CL = \bar{X}$$

Lower control limit (LCL)

$$LCL = \bar{X} - \frac{3\overline{MR}}{d_2}$$

Where d_2 is a constant obtained from statistical tables for $n=2$.

Determining control limits for the MR-chart:

For the MR-chart, the control limits can be defined as:

Upper control limit (UCL)

$$UCL = D_4\overline{MR}$$

Control limit (CL)

$$CL = \overline{MR}$$

Lower control limit (LCL)

$$LCL = D_3\overline{MR}$$

Where The constants D_4 and D_3 are derived from control chart constants in Appendix table 3 at $n=2$.

In the end, \bar{X} -bar and Moving Ranges (MR) should be plotted against time on a control chart using the calculated control limits.

Appendix Table 3 Control chart constants

Sample Size = m	A_2	A_3	d_2	D_3	D_4	B_3	B_4
2	1.880	2.659	1.128	0	3.267	0	3.267
3	1.023	1.954	1.693	0	2.574	0	2.568
4	0.729	1.628	2.059	0	2.282	0	2.266
5	0.577	1.427	2.326	0	2.114	0	2.089
6	0.483	1.287	2.534	0	2.004	0.030	1.970
7	0.419	1.182	2.704	0.076	1.924	0.118	1.882
8	0.373	1.099	2.847	0.136	1.864	0.185	1.815
9	0.337	1.032	2.970	0.184	1.816	0.239	1.761
10	0.308	0.975	3.078	0.223	1.777	0.284	1.716
11	0.285	0.927	3.173	0.256	1.744	0.321	1.679
12	0.266	0.886	3.258	0.283	1.717	0.354	1.646
13	0.249	0.850	3.336	0.307	1.693	0.382	1.618
14	0.235	0.817	3.407	0.328	1.672	0.406	1.594
15	0.223	0.789	3.472	0.347	1.653	0.428	1.572
16	0.212	0.763	3.532	0.363	1.637	0.448	1.552
17	0.203	0.739	3.588	0.378	1.622	0.466	1.534
18	0.194	0.718	3.640	0.391	1.608	0.482	1.518
19	0.187	0.698	3.689	0.403	1.597	0.497	1.503
20	0.180	0.680	3.735	0.415	1.585	0.510	1.490
21	0.173	0.663	3.778	0.425	1.575	0.523	1.477
22	0.167	0.647	3.819	0.434	1.566	0.534	1.466
23	0.162	0.633	3.858	0.443	1.557	0.545	1.455
24	0.157	0.619	3.895	0.451	1.548	0.555	1.445
25	0.153	0.606	3.931	0.459	1.541	0.565	1.435

BIOGRAPHY

NAME Kittipat Suwanpitak

DATE OF BIRTH November 29, 1996.

PLACE OF BIRTH Mueang Rayong District, Rayong, Thailand

PRESENT ADDRESS 135/1 M.5 Kram, Klaeng, Rayong 21190

EDUCATION 2015-2020 Doctor of Pharmacy at Faculty of Pharmaceutical Sciences, Burapha University, Chonburi, Thailand.

AWARDS OR GRANTS 2019 Third Best Poster Presentation Award, The international Conference of Pharmaceutical Sciences and Medicine (ICPAM), Faculty of Pharmaceutical Sciences, Burapha University, Chonburi, Thailand.

